Applied Computational Electromagnetics Society

Journal

January 2013 Vol. 28 No. 1

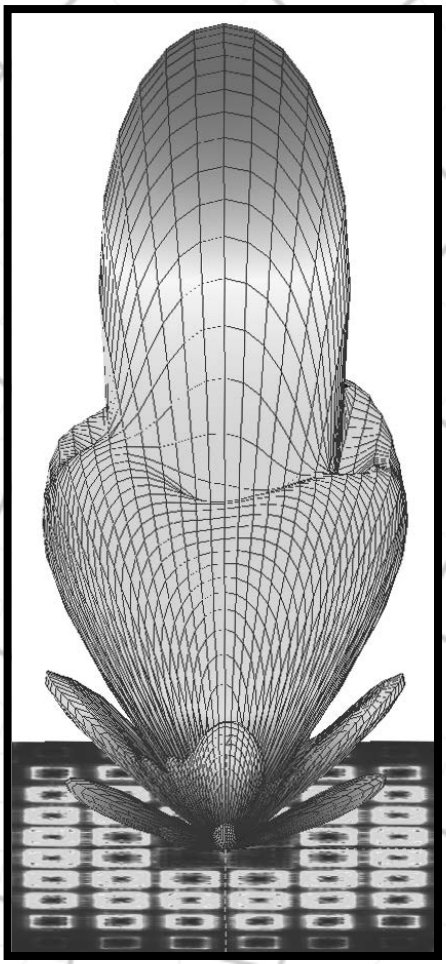

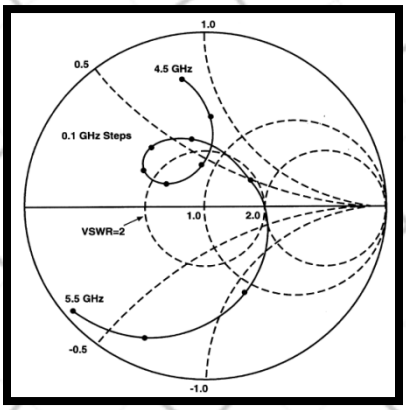

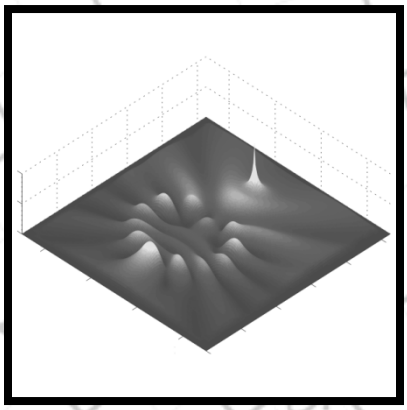

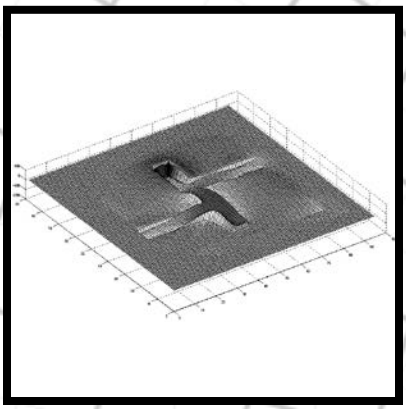

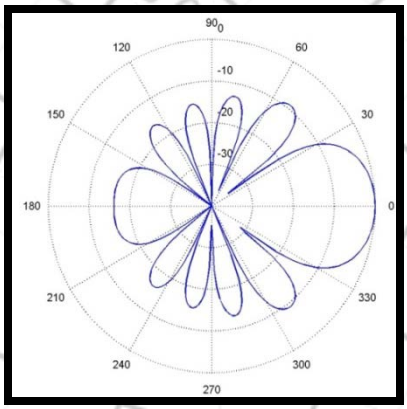

ISSN 1054-4887

GENERAL PURPOSE AND SCOPE: The Applied Computational Electromagnetics Society ***(ACES)*** Journal hereinafter known as the ***ACES Journal*** is devoted to the exchange of information in computational electromagnetics, to the advancement of the state-of-the art, and the promotion of related technical activities. The primary objective of the information exchange is to inform the scientific community on the developments of new computational electromagnetics tools and their use in electrical engineering, physics, or related areas. The technical activities promoted by this publication include code validation, performance analysis, and input/output standardization; code or technique optimization and error minimization; innovations in solution technique or in data input/output; identification of new applications for electromagnetics modeling codes and techniques; integration of computational electromagnetics techniques with new computer architectures; and correlation of computational parameters with physical mechanisms.

SUBMISSIONS: The ***ACES Journal*** welcomes original, previously unpublished papers, relating to applied computational electromagnetics. Typical papers will represent the computational electromagnetics aspects of research in electrical engineering, physics, or related disciplines. However, papers which represent research in applied computational electromagnetics itself are equally acceptable.

Manuscripts are to be submitted through the upload system of ***ACES*** web site http://www.aces-society.org See "Information for Authors" on inside of back cover and at ***ACES*** web site. For additional information contact the Editor-in-Chief:

Dr. Atef Elsherbeni
Department of Electrical Engineering
The University of Mississippi
University, MS 386377 USA
Phone: 662-915-5382
Email: atef@olemiss.edu

SUBSCRIPTIONS: All members of the Applied Computational Electromagnetics Society are entitled to access and download the ***ACES Journal*** any published journal article available at http://aces.ee.olemiss.edu. Printed issues of the ***ACES Journal*** are delivered to institutional members. Each author of published papers receives a printed issue of the ***ACES Journal*** in which the paper is published.

Back issues, when available, are $50 each. Subscription to ***ACES*** is through the web site. Orders for back issues of the ***ACES Journal*** and change of address requests should be sent directly to ***ACES*** office at:

Department of Electrical Engineering
The University of Mississippi
University, MS 386377 USA
Phone: 662-915-7231
Email: aglisson@olemiss.edu

Allow four weeks advance notice for change of address. Claims for missing issues will not be honored because of insufficient notice, or address change, or loss in the mail unless the ***ACES*** office is notified within 60 days for USA and Canadian subscribers, or 90 days for subscribers in other countries, from the last day of the month of publication. For information regarding reprints of individual papers or other materials, see "Information for Authors".

LIABILITY. Neither ***ACES***, nor the ***ACES Journal*** editors, are responsible for any consequence of misinformation or claims, express or implied, in any published material in an ***ACES Journal*** issue. This also applies to advertising, for which only camera-ready copies are accepted. Authors are responsible for information contained in their papers. If any material submitted for publication includes material which has already been published elsewhere, it is the author's responsibility to obtain written permission to reproduce such material.

APPLIED COMPUTATIONAL ELECTROMAGNETICS SOCIETY JOURNAL

January 2013
Vol. 28 No. 1
ISSN 1054-4887

The ACES Journal is abstracted in INSPEC, in Engineering Index, DTIC, Science Citation Index Expanded, the Research Alert, and to Current Contents/Engineering, Computing & Technology.

The illustrations on the front cover have been obtained from the research groups at the Department of Electrical Engineering, The University of Mississippi.

JANUARY 2013 REVIEWERS

Ahmed Abdelrahman
Iftikhar Ahmed
Seyed Armaki
Adem Aydin
Abdul Ali Babar
Mohamed Bakr
Toni Björninen
William Coburn
Veysel Demir
Khaled ElMahgoub
Mark Ingalls
Arkom Kaewrawang
Yasushi Kanai
B. David Moore
Payam Nayeri
Ozlem Ozgun
Ali Ozmetin
Stergios Papantonis
Seyyed Sedighy
Lotfollah Shafai
Sellakkutti Suganthi
Yasuhiro Tsunemitsu
Yuhao Wang
Su Yan
Xiaohua Yi

THE APPLIED COMPUTATIONAL ELECTROMAGNETICS SOCIETY

JOURNAL

Vol. 28 No. 1 January 2013

TABLE OF CONTENTS

Broadband High Efficiency Single-Layer Reflectarray Antenna Based on Spiral Crosses

Abdelhamid Tayebi, Josefa Gómez, José R. Almagro, and Felipe Cátedra

Department of Computer Science
University of Alcalá, Alcalá de Henares, Madrid, 28805, Spain
hamid.tayebi@uah.es, josefa.gomezp@uah.es, joseramon.almagro@uah.es, and felipe.catedra@uah.es

Abstract ─ This paper presents the design and analysis of a broadband high gain reflectarray antenna based on a novel radiating element, named spiral cross, that has been investigated showing high performance capabilities. The unit cell and the reflectarray antenna have been analyzed by using a full-wave Moment Method code. The proposed antenna exhibits excellent polarization purity, an aperture efficiency of 43.5 %, and a 25.3% bandwidth for 3-dB gain reduction operating at 20 GHz.

Index Terms - Broadband antenna, cross polarization, and reflectarrays.

I. INTRODUCTION

During the last few years, microstrip reflectarray antennas have received the interest of the research community because of its well-known multiple advantages. They have several attractive applications such as remote sensing, radar, satellite communications, and direct broadcast satellite services. Reflectarray antennas combine the benefits of parabolic reflectors and phased arrays antennas, which are low weight, low profile, low cost, compatibility with active devices, beam scanning capabilities, and short manufacturing time. On the other hand, their main disadvantage is the narrow-band behavior, which is due to the inherent narrow-band nature of the microstrip radiating elements and to the different spatial phase delays between the feed and each element. The second factor is more dominant in the case of large size reflectarrays, and depends on system parameters like aperture diameter, *f/D* ratio, and power factor of the feed pattern [1]. To overcome this limitation, some proposals based on multilayer configurations [2-4], single-layer multi-resonant structures [5], aperture coupled lines [6], sub-wavelength unit cells [7], and rectangular dielectric resonators [8] have been reported.

In this case, the adopted solution to increase the bandwidth is based on a single substrate layer of spiral crosses that provides a wide phase range with varying the size of the crosses. The analyzed single-layer spiral cross is cost effective and easy to fabricate, and shows good response in term of bandwidth. A reflectarray antenna has been designed and analyzed to evaluate the benefits of the proposed unit cell. Results show a notable improvement in terms of bandwidth, cross-polarization levels, and aperture efficiency when comparing with conventional single-layer reflectarrays.

II. UNIT CELL DESIGN

The design of the unit cell is a tedious task, since it must provide an appropriate reflection phase curve with a phase range wider than 360º and a linear curve slope. If both requirements are fulfilled, a wide bandwidth can be achieved and manufacturing errors can be reduced. Since the behavior of the reflectarray antenna strongly depends on the unit cell response, the optimization of its geometrical parameters is a mandatory pre-process that must be carried out before generating the whole reflectarray antenna layout.

The proposed elementary cell is a spiral cross composed of a conventional metallic cross and two little stubs perpendicularly located at the end of its four arms. We have found that the effects of adding these two little stubs are: 1) an important

Submitted On: Oct. 20, 2012
Accepted On: Jan. 3, 2013

increase in the aperture efficiency and 2) a notable bandwidth enhancement.

A single-layer configuration has been used to design the unit cell to simplify the manufacturing process and reduce the cost of the antenna. Figure 1 shows the top view of the spiral cross. The dielectric substrate located between the spiral cross and the ground plane is a 3 mm thick interface of relative permittivity $\varepsilon_r = 1.05$ and low loss tangent. It is commonly named as foam.

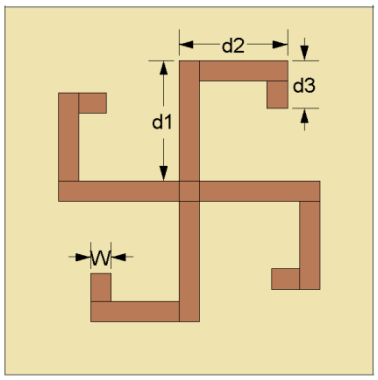

Fig. 1. Top view of the unit cell.

A parallelized Moment Method code [9-10] has been used to analyze the behavior of the unit cell. The phase curve is computed by analyzing a periodic array of identical unit cells that scatter a normal incidence plane wave. Figure 2 depicts the reflection coefficient phase versus the length of the spiral cross in the band from 18 GHz to 22 GHz. It can be seen that the phase range is slightly wider than 360º and the phase variation is quite smooth. The first condition ensures high directivity levels and the second avoids manufacturing errors due to minimum manufacturing tolerances. Note that the frequency curves remain quite linear, with no changes in the slope at extreme frequencies.

It is important to highlight that the size variation is affected to the parameters d1, d2 = 0.9d1, and d3 = 0.4d1. The variation range of parameter d1 is set from 1.763 mm to 4.249 mm, and the cross width is set to 0.5 mm in every cell.

The phase curve of a conventional cross has been also analyzed in order to evaluate the benefits of the spiral cross. The same parameter variation has been carried out at the same frequencies. In Fig. 3 it can be observed that the phase range is less than 360º for every frequency.

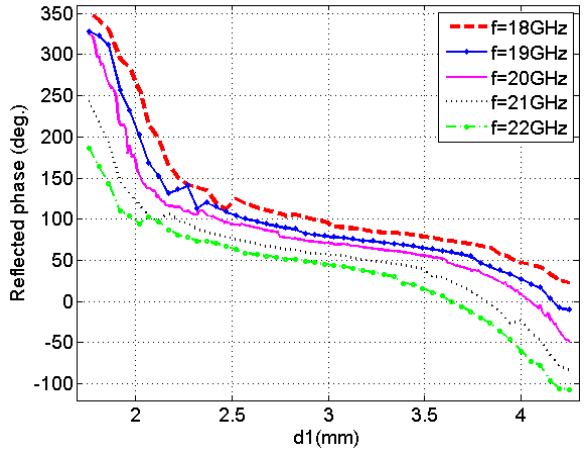

Fig. 2. Phase curve of the spiral cross in the band from 18 GHz to 22 GHz.

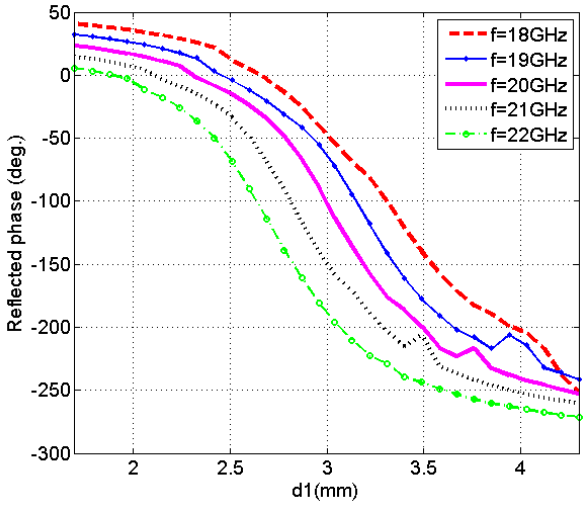

Fig. 3. Phase curve of the conventional cross in the band from 18 GHz to 22 GHz.

The reflected phase of both crosses has been also studied versus the thickness of the substrate. The results are shown in Figs. 4 and 5. It can be seen that the curve slope is too abrupt for thinner substrates in both cases. Again, the phase range is less than 360º in the case of the conventional cross for every thickness.

III. REFLECTARRAY ANTENNA DESIGN

Two center-fed reflectarray antennas have been designed and analyzed to validate the performance of the proposed unit cell. Once the phase curves are obtained, the layouts of the

reflectarray antennas are generated taking into account the phase shift introduced by each radiating element, which can be computed as follows,

$$\phi_i = k_0(d_i - \vec{r_i}\cdot\hat{r_0}) + 2\pi N \quad N = 0, 1, 2, \ldots \qquad (1)$$

where k_0 is the propagation constant in vacuum, $\hat{r_0}$ is the unit vector in the desired direction of the main beam, $\vec{r_i}$ is the position vector from the center of the reflectarray plane to the i_{th} radiating element, and d_i is the distance from the feed to the i_{th} element.

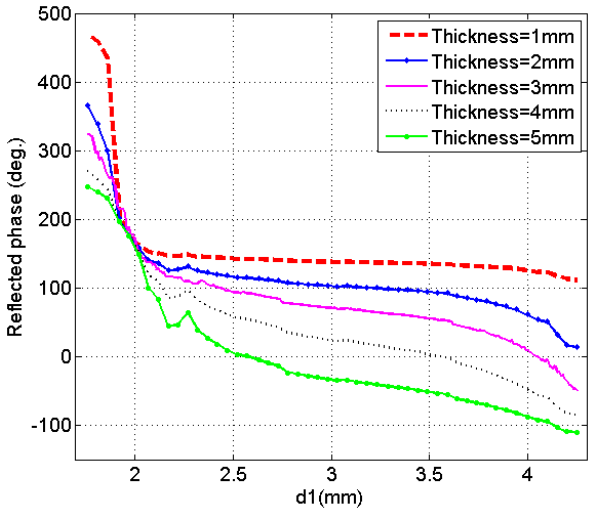

Fig. 4. Phase curve of the spiral cross versus the thickness of the substrate.

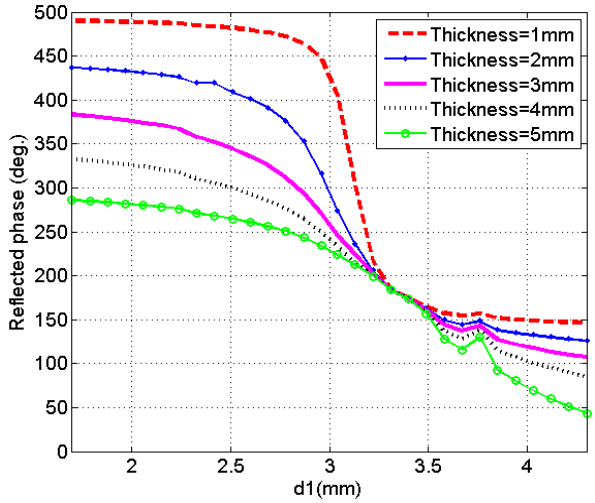

Fig. 5. Phase curve of the conventional cross versus the thickness of the substrate.

Figures 6 and 7 depict the top view of the obtained layouts. The feed location ($x_f = 0$, $y_f = 0$, $z_f = 120$ mm) is the same for both cases and has been calculated to maximize the antenna efficiency. The periodicity has been set to 0.6 λ to avoid grating lobes. The radiating elements are symmetrically located in a 15 × 15 square lattice, so the total size of the reflectarrays is 135 × 135 mm (9λ × 9λ at 20 GHz).

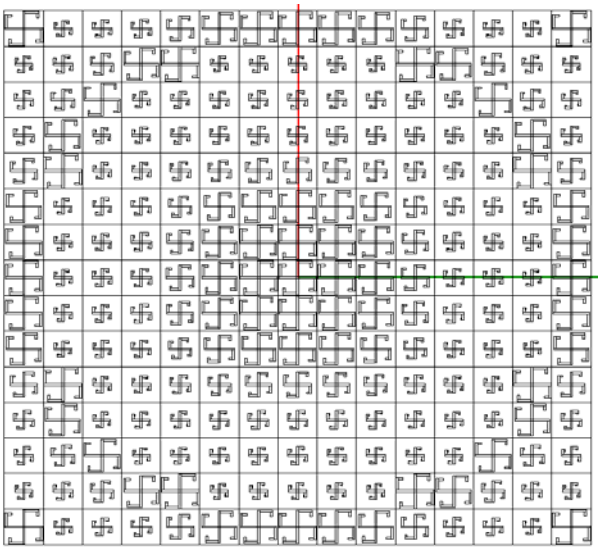

Fig. 6. Layout of the reflectarray antenna composed of spiral crosses.

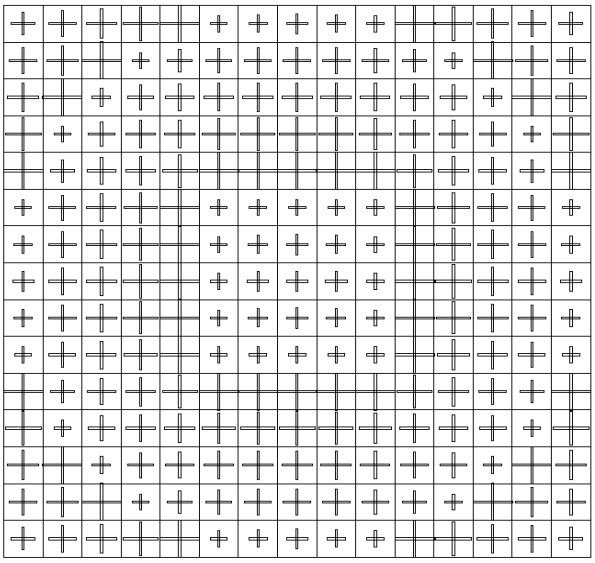

Fig. 7. Layout of the reflectarray antenna composed of conventional crosses.

IV. RESULTS

The designed reflectarray antennas have been analyzed by applying a full-wave Moment Method code [9-10]. Hence, the formulation takes into account the incidence angle of the waves that are reflected by each radiating element. This code has been validated in many benchmark experiments to check its reliability [11-13], showing high accuracy when comparing to measurements. The same linearly polarized antenna has been used to feed the reflectarrays. Figure 8 depicts the normalized radiation pattern of the feed antenna that is used in the numerical simulations.

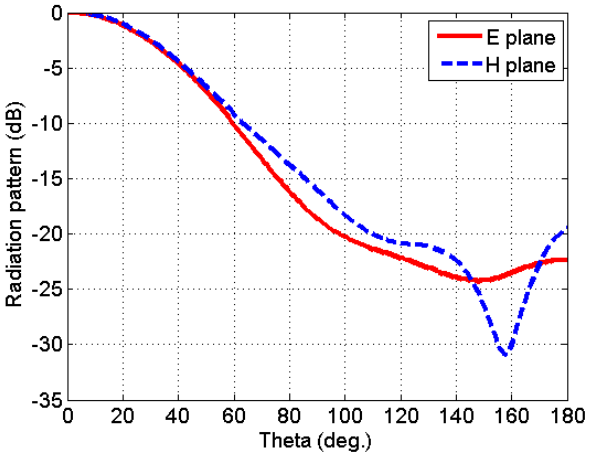

Fig. 8. Radiation pattern of the feed antenna.

The current distribution and the 3D far field radiation pattern of the spiral cross reflectarray at 20 GHz are shown in Fig. 9.

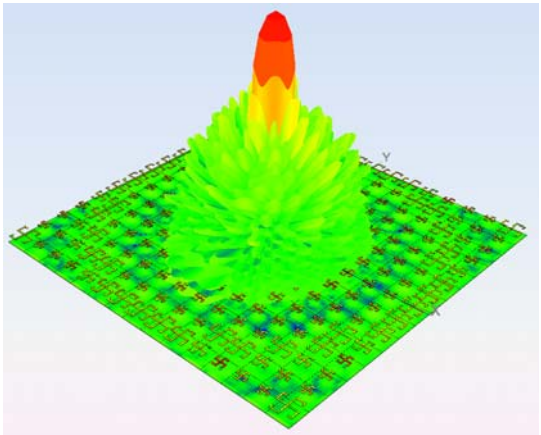

Fig. 9. Current distribution and 3D radiation pattern at 20 GHz.

Figure 10 depicts the E-plane of the normalized radiation pattern at 20 GHz. It can be seen that the simulated cross-polarization is below -30 dB for all directions. The side lobe levels of the co-polarized far field radiation pattern are below 17.6 dB regarding the maximum gain level.

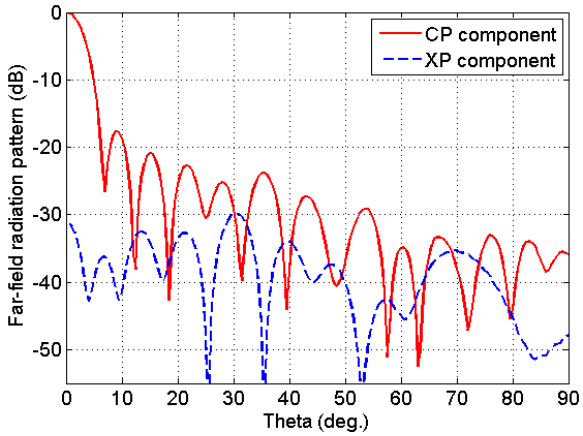

Fig. 10. Far field radiation pattern for the E-plane at 20 GHz.

Figure 11 shows a comparison between the maximum gains provided by each reflectarray. A remarkable difference can be observed. The gain peak of the spiral cross reflectarray is 26.37 dBi, which means an aperture efficiency of 43.35 %, whereas the gain peak of the conventional cross reflectarray is 24.6 dBi, which means an aperture efficiency of 28.25%. Regarding the broadband performance, the proposed reflectarray provides a 1 dB gain bandwidth of 12.41 % and a 3 dB gain bandwidth of 25.3 %. However, the conventional cross reflectarray provides a 1 dB gain bandwidth of 11 % and a 3 dB gain bandwidth of 17.5 %. On the other hand, the maximum cross-polarization level in the diagonal plane ($\theta = 45^{\circ}$) as a function of the frequency has been also studied to ensure the goodness of the polarization purity. Whereas the level of the cross-polar component is very low in the E- and H-planes, and in some cases could be high in the diagonal plane. Hence, the diagonal plane of the radiation pattern has been computed following the Ludwig's third definition [14].

Figure 12 shows the comparison between the maximum cross-polar levels in the diagonal plane, which is -26 dB for both reflectarrays. It can be seen that the polarization purity of the spiral cross reflectarray at 18.6 GHz is excellent. The cross-

polar level at that frequency is -36.6 dB. From Fig. 11 we can see that the computed gain of the spiral cross reflectarray at 18.6 GHz is 25.19 dBi, which means a decrease of 1.18 dBi regarding the maximum gain achieved at 20 GHz. However, this downgrade can be overcome by increasing the size of the reflectarray. With respect to the conventional cross reflectarray, it can be seen that the cross-polarization level is a bit lower than the levels provided by the reflectarray composed of spiral crosses at the center frequencies.

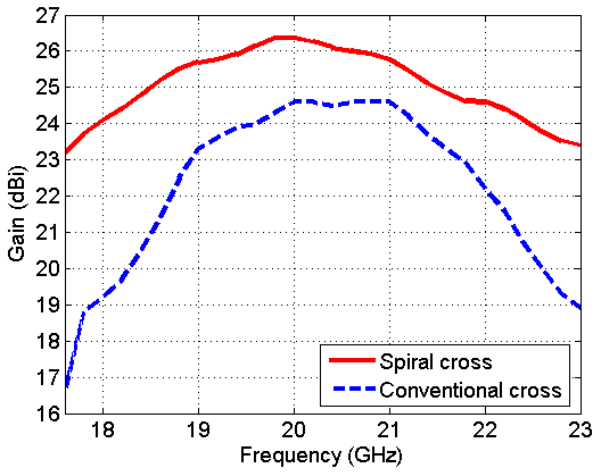

Fig. 11. Gain versus frequency for the spiral and conventional cross.

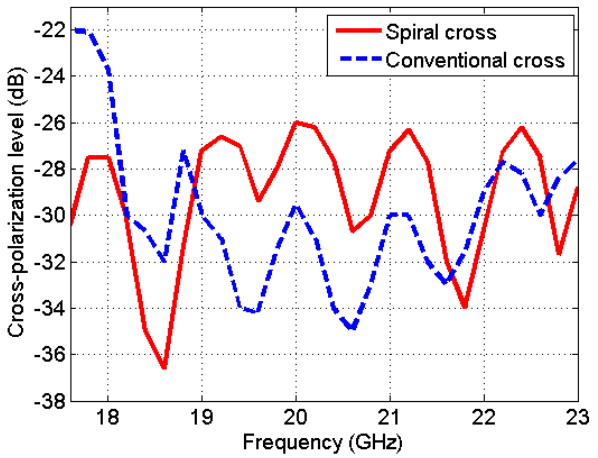

Fig. 12. Comparison of the maximum cross-polarization level in the diagonal plane versus frequency.

The bandwidth limitation due to the effect of non-constant path delay is more significant for large reflectarrays with small *f/D* ratios. Therefore, the prototype presented in this paper, whose electrical size is 9 λ and *f/D* ratio is 0.88, exhibits excellent performance when comparing to other previously published and measured reflectarrays that have similar aperture size and *f/D* ratio. For instance, the 22.8 λ reflectarray with *f/D* = 0.68 presented in [15] provides a 3 dB gain bandwidth of 6 % and cross-polarization levels lower than -16 dB. Three similar reflectarray antennas in term of size (around 9 λ) are proposed and measured in [16-18]. The reflectarray presented in [16] achieves a 3 dB gain bandwidth of 18 %, cross-polarization levels lower than -13 dB and an aperture efficiency of 35 %. Chang in [17] reports a reflectarray with *f/D* = 0.88 that provides a 3 dB gain bandwidth of 7 % and maximum cross-polar level of -25 dB. Finally, the reflectarray analyzed in [18], whose *f/D* ratio is 1.02, shows an aperture efficiency of 39.81 % and a 3 dB gain bandwidth of 17 %.

V. CONCLUSIONS

A novel unit cell named spiral cross has been studied and used to generate the layout of a 9 λ reflectarray antenna operating at 20 GHz. The designed center-fed reflectarray antenna shows good performance in terms of gain, bandwidth, aperture efficiency, and side lobe level. It achieves a 3 dB gain bandwidth of 25.3 %, an aperture efficiency of 43.35 %, maximum cross-polarization level of -26 dB, and secondary lobe level of 17.6 dB. The single-layer reflectarray is cost effective and might be a promising candidate for applications requiring high gain and low profile reflectors.

REFERENCES

[1] B. Devireddy, A. Yu, F. Yang, and A. Z. Elsherbeni, "Gain and bandwidth limitations of reflectarrays," *Appl. Comp. Electro. Society (ACES)*, vol. 26, no. 2, pp. 170-178, Feb. 2011.

[2] J. A. Encinar, "Design of a dual frequency reflectarray using microstrip stacked patches of variable size," *Electronics Letters*, vol. 32, no. 12, pp. 1049-1050, June 1996.

[3] P. Robustillo, J. Zapata, J. A. Encinar, and J. Rubio, "ANN characterization of multi-layer reflectarray elements for contoured-beam space

antennas in the Ku-band," *IEEE Trans. Antennas Propagat.*, vol. 60, no.7, pp. 3205-3214, July 2012.

[4] M. Mohammadirad, N. Komjani, A. R. Sebak, and M. R. Chaharmir, "A broadband reflectarray antenna using the triangular array configuration," *Appl. Comp. Electro. Society (ACES),* vol. 26, no. 8, pp. 640-650, August 2011.

[5] M. R. Chaharmir, J. Shaker, M. Cuhaci, and A. Ittipiboon, "A broadband reflectarray antenna with double square rings as the cell elements," *First European Conference on Antennas and Propagation*, Nice, France, pp. 1-4, Nov. 2006.

[6] E. Carrasco, M. Barba, and J. A. Encinar, "Reflectarray element based on aperture-coupled patches with slots and lines of variable length," *IEEE Trans. Antennas Propagat.*, vol. 55, no. 3, pp. 820-825, March 2007.

[7] P. Nayeri, F. Yang, and A. Z. Elsherbeni, "A broadband microstrip reflectarray using sub-wavelength patch elements," *IEEE Antennas and Propagation Society International Symposium*, Spokane, pp. 1-4, June 2009.

[8] S. H. Zainud-Deen, S. M. Gaber, A. M. Abd-Elhady, K. H. Awadalla, A. A. Kishk, "Perforated dielectric resonator antenna reflectarray," *Applied Computational Electromagnetics Society (ACES)*, vol. 26, no. 10, pp. 848-855, October 2011.

[9] http://www.fasant.com

[10] I. González, E. Garcia, F. Saez de Adana, and M. F. Cátedra, "MONURBS: A parallelized multipole multilevel code for analyzing complex bodies modeled by NURBS surfaces", *Appl. Comp. Electro. Society (ACES)*, vol. 23, no. 2, June 2008.

[11] J. Gómez, A. Tayebi, I. González, and F. Cátedra, "Design of a compact circular waveguide antenna of low polarization level using EBG structures," *Appl. Comp. Electro. Society (ACES)*, vol. 26, no. 5, 2011.

[12] I. Gonzalez, J. Gomez, A. Tayebi, and F. Catedra, "Optimization of a dual-band helical antenna for TTC applications at S band," *IEEE Antennas and Propagat. Magazine*, vol. 54, no. 4, pp. 63-77, August 2012.

[13] J. Gómez, A. Tayebi, J.R. Almagro, I. González, and F. Cátedra, "Design and Optimization of an EBG Antenna with an Efficient Electromagnetic Solver", *International Journal of Antennas and Propagation,* vol. 2012.

[14] A. Ludwig, "The definition of cross polarization," *IEEE Trans. Antennas Propagat.*, vol. 21, no. 1, pp. 116-119, Jan. 1973.

[15] A. Yu, F. Yang, A. Z. Elsherbeni, J. Huang, and Y. Kim, "An offset-fed X-band reflectarray antenna using a modified element rotation eechnique," *IEEE Trans. Antennas Propagat.*, vol. 60, no. 3, pp. 1619-1624, March 2012.

[16] H. Hasani, M. Kamyab, and A. Mirkamali, "Broadband reflectarray antenna incorporating disk elements with attached phase-delay lines," *IEEE Antennas and Wireless Propagation Letters,* vol. 9, pp. 156-158, 2010.

[17] D. C. Chang and M. C. Huang, "Multiple-polarization microstrip reflectarray antenna with high efficiency and low cross-polarization," *IEEE Trans. Antennas Propagat.*, vol. 43, no. 8, pp. 829-834, August 1995.

[18] A. Edalati and K. Sarabandi, "Wideband reflectarray antenna based on miniaturized element frequency selective surfaces," *Sixth European Conference on Antennas and Propagation*, Prague, pp. 362-364, March 2012.

Abdelhamid Tayebi was born in 1983. He received the B.Sc. and M.Sc. degrees in Telecommunications Engineering from the University Polytechnic of Cartagena, Spain, in 2005 and 2007, respectively, and the Ph.D. degree in Telecommunications Engineering from the University of Alcala, Spain in 2011. He has participated in several research projects with Spanish and European companies. His research interests focuses on design and optimization of antennas, electromagnetic radiation and scattering, on-board antennas analysis and design of reflectarray antennas.

Josefa Gómez was born in 1984. She received the B.Sc. and M.Sc. degrees in Telecommunications Engineering from the University Polytechnic of Cartagena, Spain, in 2005 and 2007, respectively, and the Ph.D. degree in Telecommunications Engineering from the University of Alcala, Spain in 2011. She has participated in several research projects with Spanish and European companies. She has been a visiting Ph.D. student at Hong Kong University. Her research interests are design and optimization of antennas, electromagnetic radiation and scattering, on-board antennas analysis and design of graphical user interfaces.

José Ramón Almagro was born in 1984. He received the Telecommunications Engineer degree from the Polytechnic University of Cartagena, Spain, in 2008. He is currently working towards the Ph.D. degree. He has been a visiting Ph.D. student at Technical University of München (TUM), Germany. He has participated in several research projects with Spanish and European companies. His research interest is methods of measurement of antennas in anechoic chambers, design of antennas, electromagnetic radiation and GPU computing.

Felipe Cátedra, IEEE Fellow received his M.Sc. and Ph. D. degrees in Telecommunications Engineering from the Polytechnic University of Madrid (UPM) in 1977 and 1982, respectively. From 1976 to 1989 he was with the Radio Communication and Signal Processing Department of the UPM. He has been Professor at the University of Cantabria from 1989 to 1998. He is currently Professor at the University of Alcalá, in Madrid, Spain. He has worked on about 90 research projects solving problems of Electromagnetic Compatibility in Radio and Telecommunication Equipment, Antennas, Microwave Components and Radar Cross Section and Mobile Communications. He has developed and applied CAD tools for radio-equipment systems such as Navy ships, aircraft, helicopters, satellites, the main contractors being: EADS, ALCATEL, CNES, ALENIA, DASA, SAAB, INTA, BAZAN, INDRA, the Spanish Defence Department, European Spatial Agency. Ericsson, MATRA SPACE, CSELT, KTH, Texas University, Drexel University, Singapour University, Mitsubishi, Kawasaki Heavy Industries, BOSCH, , INDRA, GMV, ACCIONA. Recently he promoted the creation of a technology-based company of the University of Alcalá called NEWFASANT (www.fasant.com) for a better transfer of techniques developed by the research team he leads. He has directed about 18 Ph. D. dissertations, has published about 70 papers (IEEE, Electronic Letters, etc.), three books, about 10 chapters in different books, has given short courses and has given around a hundred and thirty presentations in International Symposia.

A Multi-Band/UWB MIMO/Diversity Antenna with an Enhanced Isolation Using Radial Stub Loaded Resonator

Yingsong Li[1], Wenxing Li[1, 2], and Wenhua Yu[1, 2, 3]

[1]College of Information and Communication Engineering,
[2]Institute of Electromagnetic and Wireless Engineering,
Harbin Engineering University, Harbin, Heilongjiang 150001, China
liyingsong82@gmail.com and liwenxing@hrbeu.edu.cn

[3]2COMU, Inc.
State College, PA 16803
wenyu@2comu.com

Abstract ─ In this paper a multi-band/Ultra-Wideband (UWB) Multiple Input Multiple Output (MIMO) antenna, which is composed of two identical microstrip fed triple notch band UWB antennas and a Radial Stub Loaded Resonator (RSLR), is proposed and verified numerically and experimentally. The antenna is designed to meet the requirement of multi-band/UWB communication applications. A Defected Microstrip Structure (DMS) Band-Stop Filter (BSF) and an invert π-shaped slot are employed to design the triple notch band UWB antenna. The resonance characteristics of the DMS-BSF and the band notch functions are presented to realize the proposed triple notch band UWB antenna. The isolation of the multi-band/UWB-MIMO antenna has been enhanced by inserting an RSLR loaded T-shaped stub between two identical triple notch band antennas. Both simulation and measurement results are presented to illustrate the performances of the proposed multi-band/UWB-MIMO antenna.

Index Terms – Band notch antenna, diversity antenna, MIMO antenna, multi-band antenna, and UWB antenna.

I. INTRODUCTION

With the rapid development of wireless communication, the high performance modern communication systems with low cost and high data rate have been becoming an urgent requirement. The UWB technology is one of the potential candidates in the race of wireless communication since the Federal Communications Commission (FCC) approved the commercial use of the bandwidth from 3.1 GHz to 10.6 GHz [1]. It is a well-known fact that UWB antenna is one of the key parts in the UWB systems, and many types of UWB antennas have been proposed to meet this application [2-9], such as microstrip fed UWB antenna [2, 4-8] and coplanar waveguide (CPW) fed UWB antenna [3]. However, in contrast to the wide bandwidth of the UWB systems, there exist some Narrow Band (NB) wireless systems that have been licensed and used for a long time. It is necessary to design UWB antenna with notch band characteristic to mitigate the potential interference between NB and UWB systems. Therefore, a practical UWB antenna can not only be satisfying the wide bandwidth, covering the whole UWB band, but also has the low interference with the NB systems. Recently, numbers of UWB antennas including the notch bands have been proposed to reduce the potential interference level [10-16]. However, most of proposed notch band characteristics are obtained by etching various slots on either the radiation patch or the ground plane, which will leak electromagnetic wave, in turn; they will deteriorate the system radiation patterns. In addition, the transmitted power of the UWB systems is limited to a relatively low level (-41.3 dBm/MHz). In order to overcome this limitation, the MIMO technology using multipath

Submitted On: Nov. 9, 2012
Accepted On: Jan. 3, 2013

has been combined with the UWB technology to find an alternative solution for solving the issues above [17-18]. Another challenge in the implementation of the MIMO technique for compact devices arises from the strong mutual coupling between the closely packed antenna elements. Mutual coupling can be usually improved by increasing the distance between the antenna elements but the compact size of the wireless devices makes it impossible in most practical cases [19-27]. A possible approach appears to enhance the isolation or to reduce the mutual coupling by using some other techniques, such as slots and stubs in the antenna structure [19-22]. Furthermore, the DMS structure has been recently widely studied and used for coupling reduction, filter design, and compact antenna design [28-37].

In this paper, a multi-band/UWB-MIMO antenna with anenhanced isolation is proposed and verified numerically and experimentally. The proposed UWB antenna with three notch bands can cover the entire UWB band and also reduce the potential interference from the NB systems. The proposed antenna exploits the approach by using a stub on the ground plane to enhance the isolation. A modified DMS-BSF [31] and an invert π-shaped slot are employed to provide three notch bands for reducing the interference from the NB systems. The mutual coupling between the two multi-band/UWB antennas is reduced by using the RSLR loaded T-shaped stub. The proposed multi-band/UWB-MIMO antenna shows that the isolation level is better than 15 dB over the entire operation band.

Section 2 in this paper presents a triple band notched UWB antenna integrated with the DMS-BSF and the invert π-shaped slot. The resonance characteristic of the DMS-BSF and the notch band functions are analyzed. Moreover, the multi-band/UWB-MIMO antenna with a radial stub loaded resonator loaded T-shaped stub on the ground plane is also proposed. Section 3 illustrates the parametric investigation of the proposed multi-band/UWB-MIMO antenna. The experimental results including the reflection and transmission coefficients, radiation patterns, and the correlation coefficient are presented in section 4. A brief conclusion is presented in section 5.

II. ANTENNA DESIGN

A. Design of the notch band UWB antenna

Figure 1 illustrates the configuration of the proposed triple notch band UWB antenna, which is printed on the substrate surface whose relative dielectric constant, loss tangent, and thickness are 2.65, 0.002, and 1.6 mm, respectively. The UWB antenna consists of a rectangular radiation patch, two square tapped corners at the bottom of rectangular radiation patch, an inverted π-shaped slot embedded in the rectangular radiation patch, a DMS-BSF etched in a microstrip feed line, a partial ground plane, and a 50 Ω microstrip feed line. The radiation patch and the microstrip feed line are printed on the top surface of the substrate while the partial ground plane is printed on the bottom surface. The DMS-BSF embedded in the microstrip feed line is a dual mode resonator, as shown in Fig. 2.

The resonance and phase characteristics of the 50 Ω microstrip line with a meander slot DMS-BSF are shown in Figs. 3 and 4, respectively, in which the parameters L1, g and g1 of proposed DMS-BSF are selected to be 6.6 mm, 0.5 mm, and 0.4 mm, respectively. Figure 3 shows the effects of L1 on the S-parameters of the microstrip feed line with DMS-BSF. It can be observed from Fig. 3 that the DMS-BSF shows dual stop band characteristic in the operation band. As L1 increases, the first resonant frequency shifts down slowly to a lower band while the second resonant frequency moves fast toward a lower band, which means that the length of the meander slot DMS-BSF changes its capacitance characteristic. The first resonant frequency has a tuning stop band from 3.5 GHz to 6 GHz while the second resonant frequency can be adjusted from 7.4 GHz to 12.9 GHz. Therefore, the stop band of the DMS-BSF can be tuned easily. Figure 4 shows the phase characteristic of the microstrip feed line with and without the DMS. A 90º phase jumping for the case with the DMS-BSF is shown in Fig. 4. At frequencies 4.2 GHz and 10.9 GHz, the inductance characteristic changes to be a capacitance in the S21 phase diagram. The discontinuous phase characteristic makes the microstrip line a group delay and two notch bands in the two discontinuous phase points.

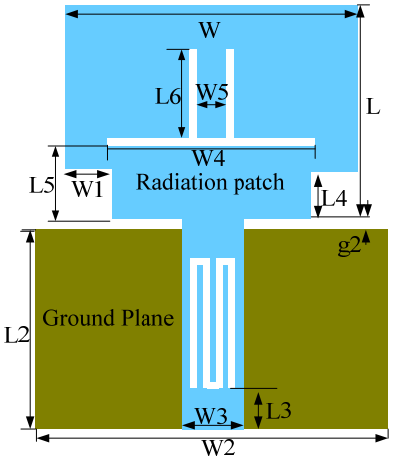

Fig. 1. Geometry of the proposed band notched UWB antenna.

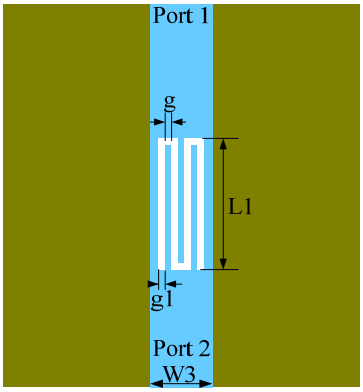

Fig. 2. Structure of the DMS-BSF in the microstrip feed line.

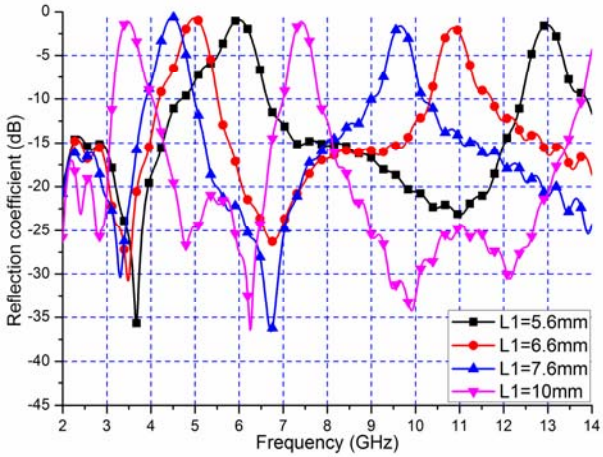

(a)

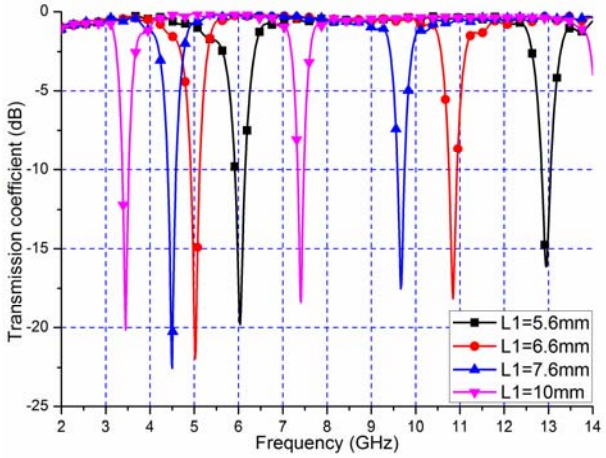

(b)

Fig. 3. Simulated (a) reflection and (b) transmission coefficients of the microstrip feed with DMS-BSF.

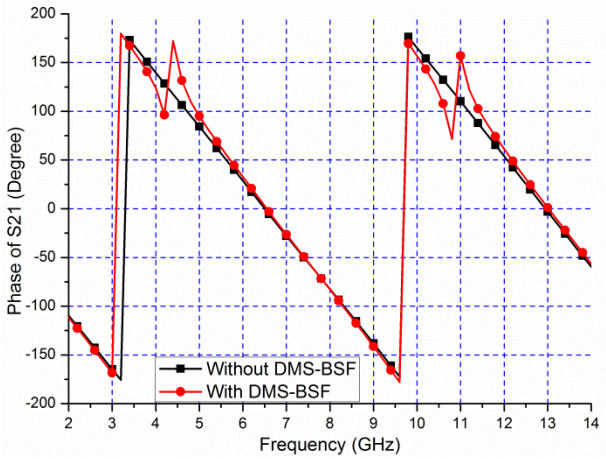

Fig. 4. Phase characteristics of the microstrip feed with DMS-BSF.

Based on the investigation of the microstrip feed line with or without DMS-BSF, another notch band is introduced by using an inverted π-shaped slot etched in the radiation patch. The inverted π-shaped slot is a quarter-wavelength resonant filter. The resonant frequency of the inverted π-shaped slot, for the given dimensions of the notch band function at 6.8 GHz, can also be postulated as,

$$\lambda_{notch} = \frac{c}{f_{notch}\sqrt{\varepsilon_{eff}}} = \frac{c}{f_{notch}\sqrt{\frac{\varepsilon_r + 1}{2}}} \qquad (1)$$

where λ_{notch} is the wave length of the notch band, f_{notch} is the center resonant frequency of the notch band, ε_{eff} is the effective dielectric constant, ε_r is the relative dielectric constant, and c is the speed of light in free space. We take equation (1) in to consideration to achieve the original dimensions of the inverted π-shaped slot in the design. The inverted π-shaped slot is also integrated in the proposed antenna shown in Fig. 1. In order to achieve the ideal simulation results, the proposed tri-notch band UWB antenna is printed on the same substrate with a dielectric constant of 2.65, a loss tangent of 0.002, and a thickness h = 1.6 mm. The simulation results of the tri-notch band functions are shown in Fig. 5.

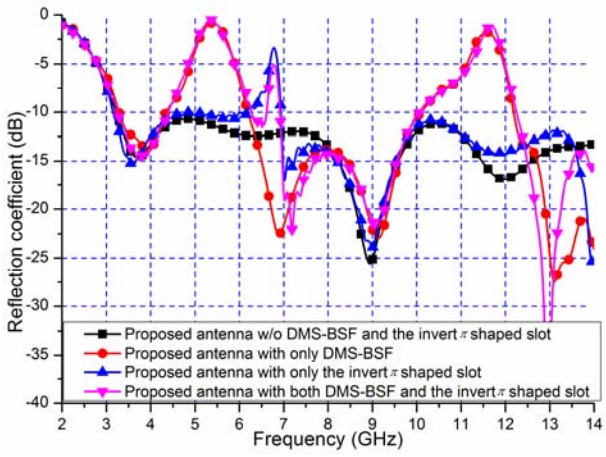

Fig. 5. Reflection characteristics of the proposed tri-notch band UWB antenna.

It can be seen from Fig. 5 that the proposed tri-notch band UWB antenna without the DMS-BSF and the inverted π-shaped slot is an UWB antenna covering the entire band from 3.1 GHz to 14 GHz. When the proposed antenna has only an inverted π-shaped slot, the antenna is an UWB antenna with a notch band near 6.8 GHz, which can reduce the potential interference from RFID systems. As for the proposed UWB antenna with DMS-BSF only, the antenna has two notch bands near 5.5 GHz and 11.5 GHz, respectively. The two notch bands can reduce the potential interference from WLAN, WiMAX, and X-band. The proposed antenna with both DMS-BSF and inverted π-shaped slot has three notch bands. This is also a four band antenna in the frequency bands 3.1 GHz - 4.2 GHz, 6.2 GHz - 6.6 GHz, 7.0 GHz – 10 GHz and 12.2 GHz – 14 GHz. It is observed that the notch band around 6.8 GHz is generated by the inverted π-shaped slot while the other notch bands near the 5.5 GHz and the 11.5 GHz are caused by the DMS-BSF. It is worthwhile to mention that the three notch bands can be designed independently.

The tri-notch band UWB antenna is optimized and fabricated to further verify the proposed design. The optimized dimensions of the proposed tri-notch band antenna are as follow (all units are in mm): L = 15, W = 16, W1 = 2, W2 = 30, W3 = 4.7, W4 = 9, W5 = 3.2, L2 = 16.2, L3 = 3.7, L4 = 2.2, L5 = 4.1, L6 = 6.2, and g2 = 0.8. The parameters L1, g, and g1 of the DMS-BSF are selected to be 6 mm, 0.5 mm and 0.4 mm, respectively. The fabricated tri-notch band UWB antenna is shown in Fig. 6. The measured reflection coefficient, using Anritsu 37347D vector network analyzer, is shown in Fig. 7. It can be observed from Fig. 7 that the measurement results in the low frequency band agree well with the simulated one. The slight discrepancy between the simulated and measured curves in the high frequency band may be caused by the coarse mesh in the numerical simulation using the FDTD method and the fabrication errors.

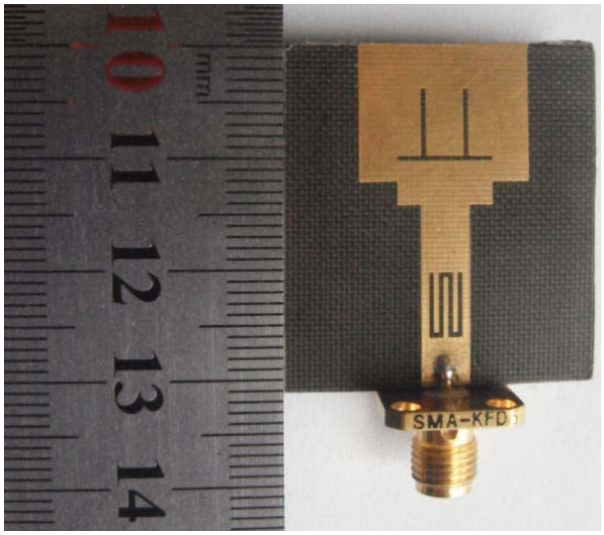

Fig. 6. Photograph of the fabricated tri-notch band antenna.

B. Multi-band/UWB MIMO antenna

In this section, a multi-band/UWB-MIMO antenna is proposed using two identical tri-notch band antennas, as shown in Fig. 8 (a). Based on the

investigation of the proposed tri-notch band UWB antenna, the multi-band/UWB-MIMO antenna integrated with an RSLR loaded T-shaped stub is shown in Fig. 8 (c). The RSLR loaded T-shaped stub is illustrated in Fig. 8 (b). The RSLR loaded T-shaped stub is inserted between the two identical tri-notch band UWB antennas in Fig. 8 (a) to form the multi-band/UWB diversity/MIMO antenna shown in Fig. 8 (c).

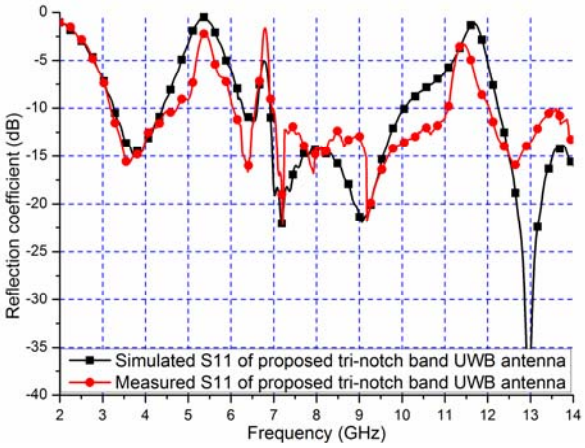

Fig. 7. Measured results of the fabricated tri-notch band antenna.

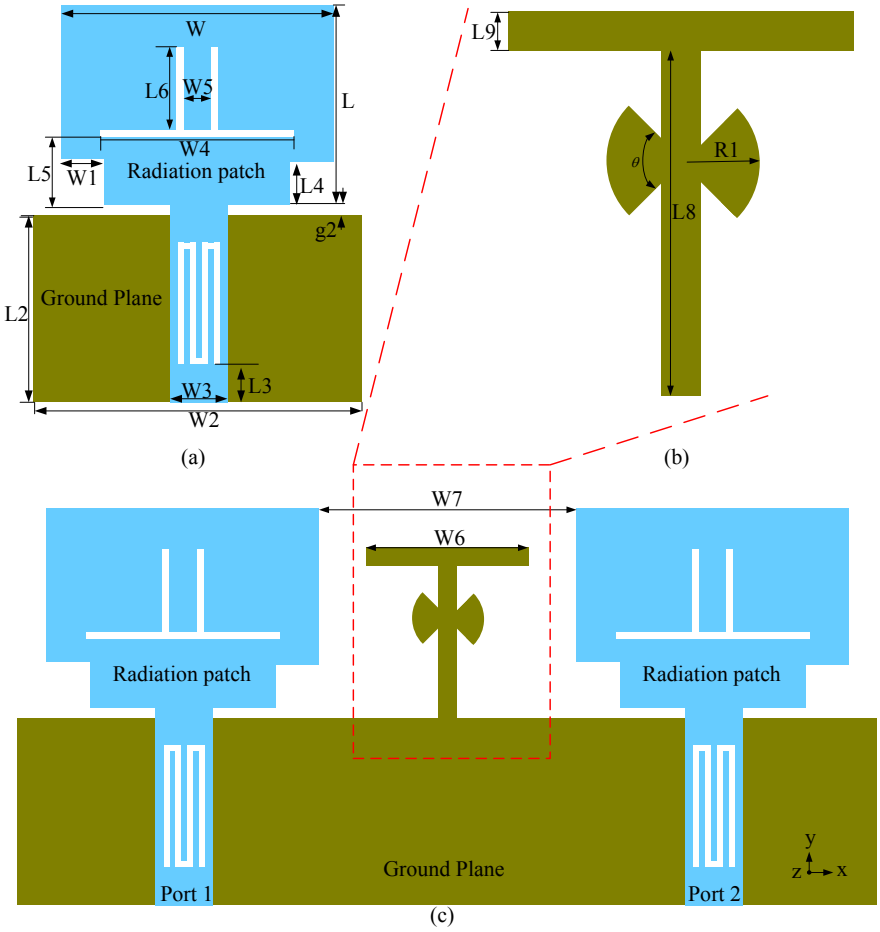

Fig. 8. Geometry of the proposed multi-band/UWB-MIMO antenna.

For the sake of comparison, the multi-band/UWB-MIMO antenna without RSLR loaded T-shaped stub is also investigated to evaluate the performance of multi-band/UWB-MIMO antenna. The multi-band/UWB-MIMO antenna is adjusted to be a smaller size compared with other UWB-MIMO antennas [17-18]. The substrate parameters in the proposed MIMO antennas are selected to be

ε_r = 2.65, δ = 0.002, and h = 1.6 mm. The antenna dimensions are optimized to be (all units are in mm): L = 15, W = 16, W1 = 2, W2 = 30, W3 = 4.7, W4 = 9, W5 = 3.2, L2 = 16.2, L3 = 3.7, L4 = 2.2, L5 = 4.1, L6 = 6.2, g2 = 0.8, W6 = 8, W7 = 14, R1 = 3, L9 = 1, L8 = 9.8, and θ = 60º. The dimensions of the DMS-BSF are selected to be L1 = 6mm, g = 0.5 mm, and g1 = 0.4 mm, respectively.

It is worthwhile to mention that the RLSR loaded T-shaped stub plays a key role in the isolation enhancement. The effects of the RLSR loaded T-shaped parameters on the antenna performance are investigated in the next section. Compared with the stub used in [22], the proposed RSLR loaded T-shaped stub has simple structure and is easy to design.

III. PARAMETRIC STUDY

The proposed RLSR loaded T-shaped stub will be investigated in this section. The reflection and transmission coefficients S_{11} and S_{21}, of the proposed multi-band/UWBMIMO antenna with various parameters are investigated. For the sake of comparison, the multi-band/UWBMIMO antenna without RLSR loaded T-shaped stub is also presented. In the simulation of the multi-band/UWBMIMO antenna, when one parameter changes, the rest of the parameters are kept the same as the optimization parameters listed in section 2. Since the structure is symmetric, it is sufficient to show the S_{11} and S_{21} only. It is observed from the parametric study that the variations of the dimensions of RSLR loaded T-shaped stub are not a linear relationship to S_{11} and S_{21}. The aim of the parametric study is to obtain the variation trend of the S_{11} and S_{21} with the dimension of the RSLR loaded T-shaped stub. The effects of R1, W6, and θ on the antenna performance are presented to investigate S_{11} and S_{21}. The effects of R1 on the antenna performance are demonstrated in Fig. 9. It is found that the impedance bandwidth of the multi-band/UWB MIMO antenna has been improved in the lower frequency band with the increase in the radius R1 of RLSR. The impedance bandwidth between 7 GHz and 9 GHz is deteriorated at a larger radius of RLSR because of the effects on the notch band UWB antennas. The isolation in the lower frequency band has been enhanced significantly with the increase of the radius R1 of RLSR. The isolation between 7 GHz and 9 GHz is a little deteriorated with the increase of R1. This is caused by the increase of R1 near the notch band UWB antenna. Moreover, it also effects the radiation of the proposed multi-band/UWB MIMO antenna elements.

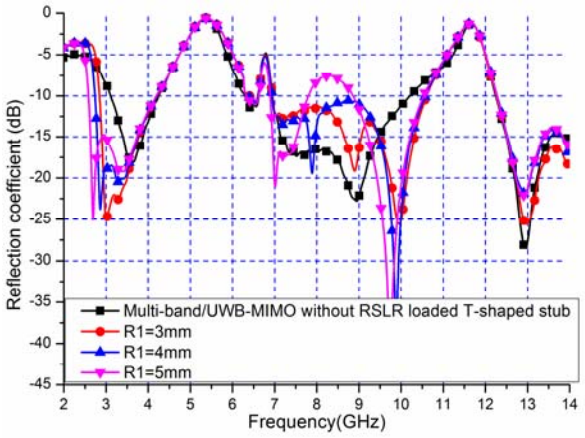

(a)

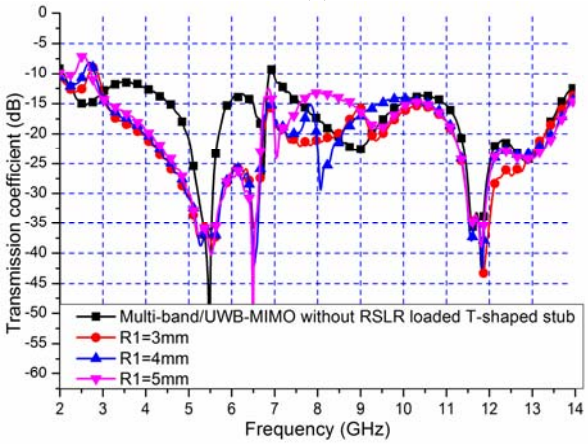

(b)

Fig. 9. Variation of the (a) reflection and (b) transmission coefficients with the parameter R1.

The variation of the S-parameter with θ is presented in Fig. 10. It can be seen from Fig. 10 (a) that the impedance bandwidth at the lower frequency band has been widened with the increase in θ of RLSR. The impedance bandwidth between 8 GHz and 9.3 GHz is getting worse compared with the multi-band/UWB MIMO antenna without RSLR loaded T-shaped stub. It is noticed from Fig. 10 that the bandwidth of the higher notch band near the 11.5 GHz becomes narrower. The isolation shown in Fig. 10 (b) is

improved in the lower frequency band. Inside the lower notch band, the isolation at WLAN and WiMAX bands is higher than 25 dB. However, the isolation at the X-band is deteriorated with the increase of parameter θ in RLSR. This is caused by the increase in θ of RLSR near the notch band UWB antenna and the T-shaped stub.

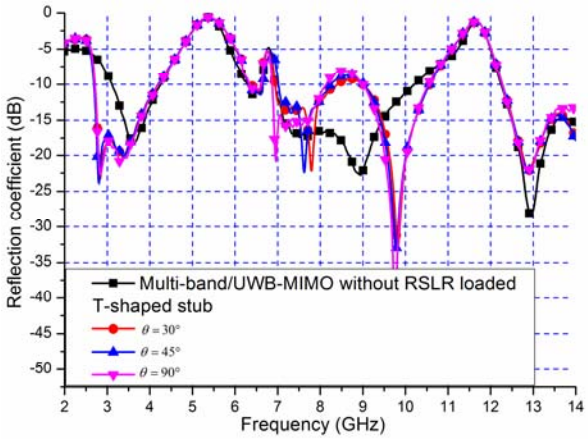

(a)

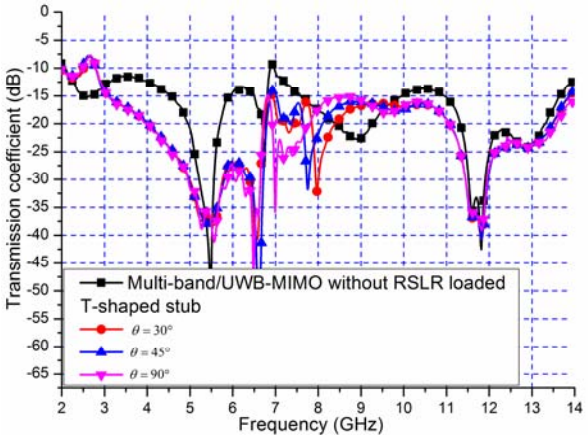

(b)

Fig. 10. Variation of the (a) reflection and (b) transmission coefficients with parameter θ.

The results with W6 variations are summarized in Fig. 11. We can observe from Fig. 11 (a) that the impedance bandwidth of the proposed multi-band/MIMO antenna is increased with W6 while the impedance bandwidth between 7.6 GHz and 8.3 GHz is exacerbated with W6. The bandwidth of the higher notch band is narrower than the proposed MIMO antenna without RSLR loaded T-shaped stub. It is evident that the isolation of the proposed multi-band/MIMO antenna has been improved. The isolation over the entire operation band is better than the MIMO antenna without RSLR loaded T-shaped stub. Especially, in the lower frequency band, the isolation is improved from 5 dB to 10 dB. At 7 GHz, the mutual coupling is reduced about 7 dB for W6 = 6mm. In the high frequency band, the isolation is deteriorated with increasing W6. However, the isolation is improved compared to the MIMO antenna without the RSLR loaded T-shaped stub.

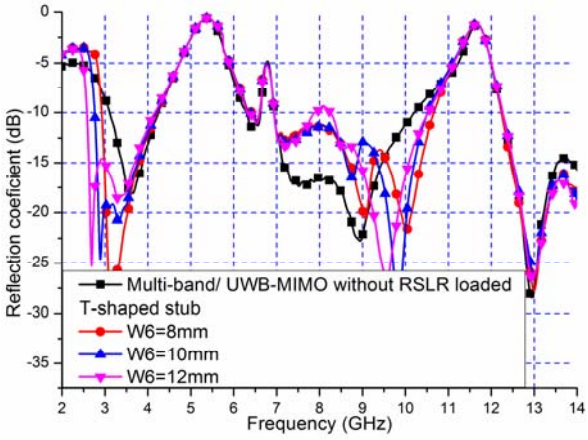

(a)

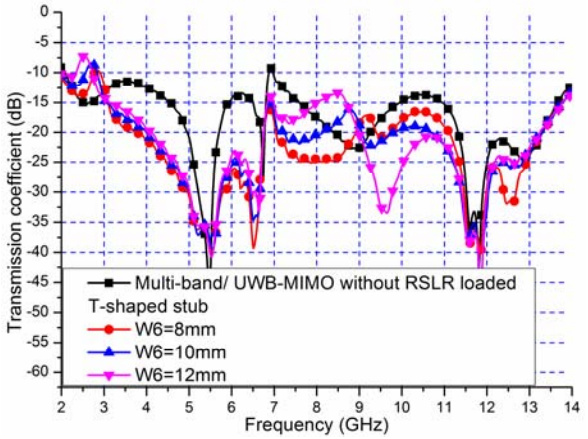

(b)

Fig. 11. Variation of the (a) reflection and (b) transmission coefficients with parameter W6.

The correlation coefficient, which represents the coupling between the antenna elements, is an important parameter in the design of the MIMO antenna. The lower the correlation coefficient is,

the better the diversity gain is. The correlation coefficient can be usually calculated from the 3-D radiation patterns generated by exciting different antenna ports or S-parameters. Here, we use the S-parameters to calculate the correlation coefficient based on equation (2), which represents the average correlation between the total powers radiated by the antenna within a 3D space [18],

$$\rho = \frac{\left|S_{11}^{*}S_{12} + S_{21}^{*}S_{22}\right|^{2}}{(1-\left|S_{11}\right|^{2}-\left|S_{21}\right|^{2})(1-\left|S_{22}\right|^{2}-\left|S_{12}\right|^{2})}. \quad (2)$$

There exists an approximate relationship between the diversity gain G_{app} and the correlation coefficient ρ that can be described mathematically [18] as given in equation (3),

$$G_{app} = 10 * \sqrt{1-\left|\rho\right|}. \quad (3)$$

According to the investigation aforementioned, the correlation coefficient of the MIMO antenna is shown in Fig. 12. The correlation coefficients are calculated from the S-parameters of the investigated results above. It is found that the correlation coefficient is less than -30 dB except the 6.8 GHz band, as shown in Fig. 12, which corresponds to a high diversity gain. This is due to the proposed RLSR, which can provide a good isolation and thus improves the correlation coefficient. In the RFID band, 6.8 GHz, the correlation coefficient may be attributed to the weak response of the inverted π-shaped slot.

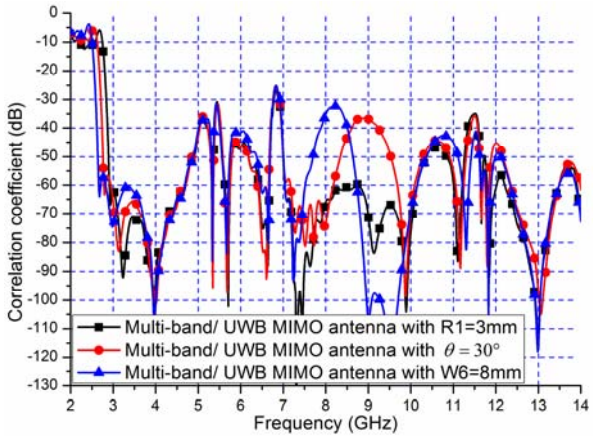

Fig. 12. Correlation coefficient of the proposed multi-band/UWB MIMO antenna.

IV. RESULTS AND DISCUSSIONS

To evaluate the proposed multi-band/UWB MIMO antenna, the designed MIMO antenna is fabricated and measured. The multi-band/UWB MIMO antenna is optimized based on the parametric studies. The geometric parameters are listed as follows (all units are in mm): L = 15, W = 16, W1 = 2, W2 = 30, W3 = 4.7, W4 = 9, W5 = 3.2, L2 = 16.2, L3 = 3.7 L4 = 2.2, L5 = 4.1, L6 = 6.2, g2 = 0.8, W6 = 8, W7 = 14, R1 = 3, L9 = 1, L8 = 9.8, and θ = 60º. The dimensions of the DMS-BSF are L1 = 6mm, g = 0.5mm, and g1 = 0.4 mm. The proposed multi-band/UWB MIMO antenna with the RSLR loaded T-shaped stub is fabricated, as shown in Fig. 13. The measured results are shown in Fig. 14. It can be seen from Fig. 14 that the measured results agree well with the simulated ones. The slight mismatch between the simulated and measured results might be due to the fabrication errors. The measured radiation patterns of the proposed multi-band/UWB MIMO antenna at 3.5 GHz, 6.2 GHz and 9.5 GHz are shown in Fig. 15. In the measurement of the radiation patterns, port 1 is excited while port 2 is terminated with a 50 Ω load. It can be seen from Fig. 15 that the radiation patterns of the proposed multi-band/UWB MIMO antenna are reliable in the operation bands. The patterns in the y-z plane are similar to those in Fig. 15 (a), but not true in the x-z and x-y planes. The difference in the radiation pattern in the x-y plane is useful for pattern diversity as shown in Fig. 15 (a) and (b). In addition, the proposed multi-band/UWB MIMO antenna consists of two identical and symmetric band notched UWB antennas. Therefore, when port 2 is excited and port 1 is matched by a 50 Ω load, the radiation patterns are similar to those shown in Fig. 15.

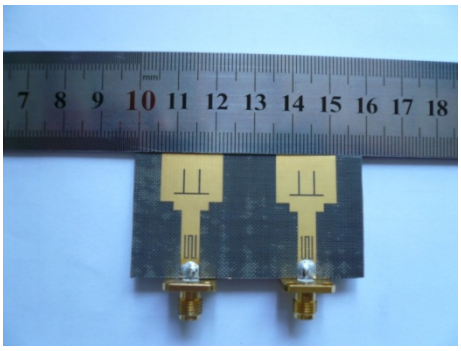

(a)

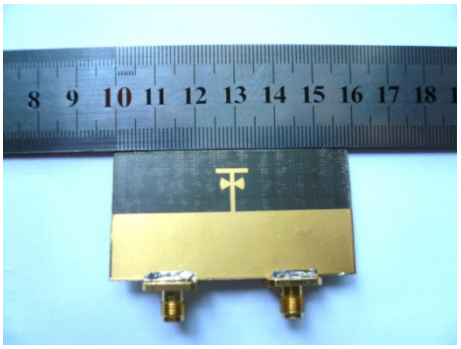

(b)

Fig. 13. Photograph of the (a) front view and (b) back view of the fabricated MIMO antenna.

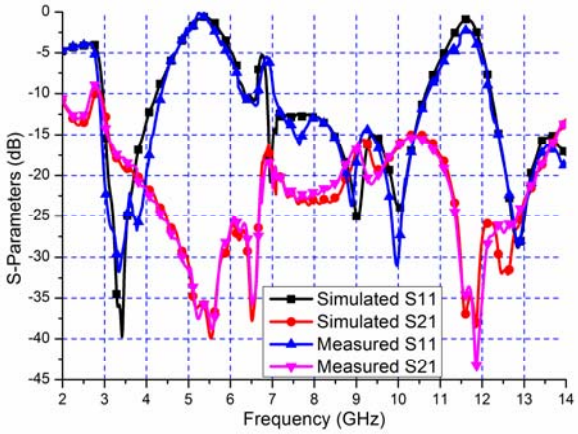

Fig. 14. S-parameters of the proposed multi-band/ UWB MIMO antenna.

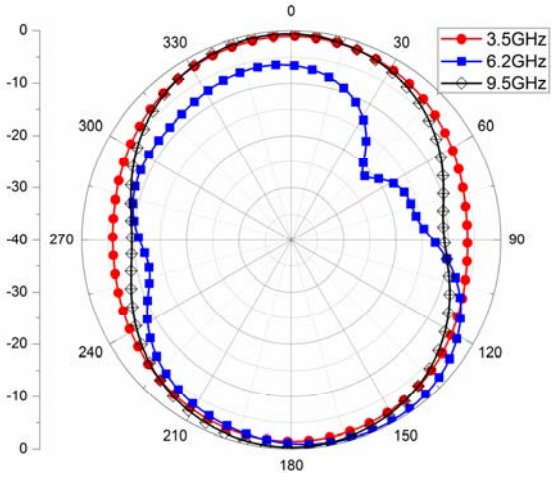

(a) x-z plane

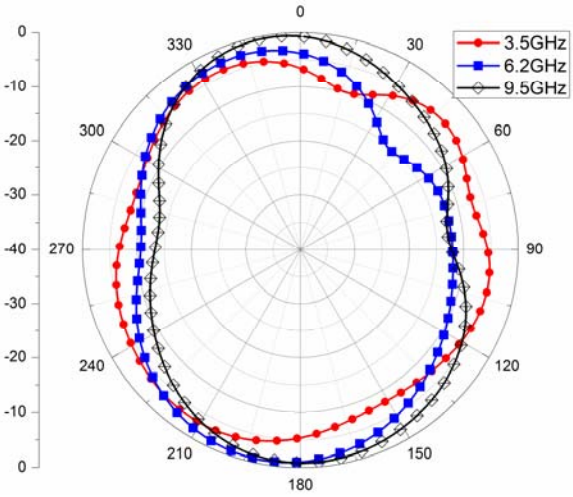

(b) y-z plane

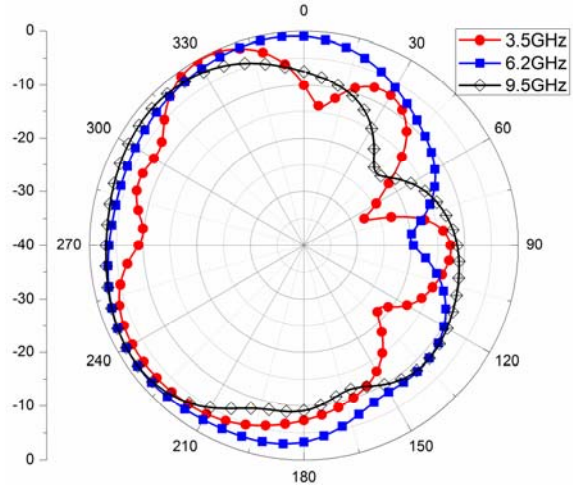

(c) x-y plane

Fig. 15. Radiation patterns of the proposed multi-band/UWB MIMO antenna at different frequencies for the three plane cuts.

The simulated total efficiencies and the maximum absolute gains of the proposed multi-band/UWB MIMO antenna with or without the RSLR loaded T-shaped stub are shown in Figs. 16 and 17, respectively. The proposed antenna has over 80 % efficiency in the operation bands except the notch bands, which are designed for reducing the potential interference between UWB and NB systems [38]. It is evident from Fig. 17 that the efficiency is improved in the lower frequency

band. This is caused by the enhanced isolation in the lower frequency band, which reduces the coupling between the two antennas. It can be noticed from Fig. 17 that the gain is reduced in the lower frequency band and that it is similar to that of the design without the RSLR loaded T-shaped stub in the higher frequency band. The variation of the gain is within 2 dBi in the entire frequency band, which is very good for wideband and multi-band systems.

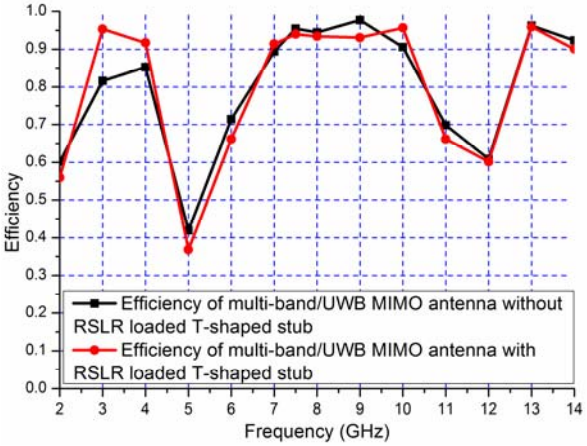

Fig. 16. Efficiency of the proposed MIMO antenna versus frequencies.

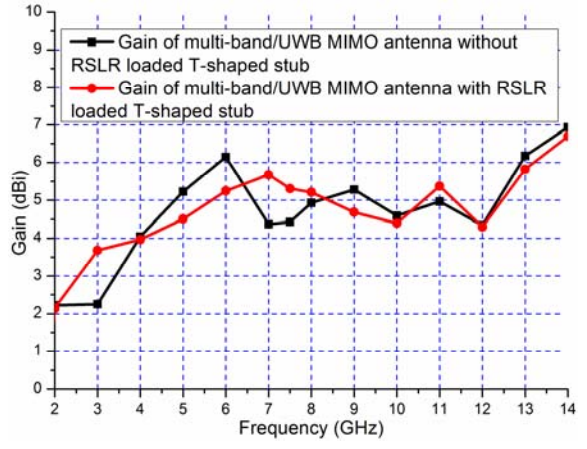

Fig. 17. Gain comparison of the proposed MIMO antenna with and without RSLR loaded T-shaped stub.

V. CONCLUSION

In this paper, a multi-band/UWB MIMO antenna with an RSLR loaded T-shaped stub is investigated numerically and experimentally. The design procedure of the MIMO antenna consists of DMS-BSF, multi-band antenna and RSLR loaded T-shaped stub. The DMS-BSF and RSLR loaded T-shaped stub are employed to generate the band notch characteristics and to increase the isolation of the MIMO antenna, respectively. By adjusting the parameters of the RSLR loaded T-shaped stub, the coupling between the two multi-band/UWB antennas has been reduced. The numerical and experimental results of the impedance bandwidth, isolation level, and radiation patterns demonstrate that the proposed multi-band/UWB MIMO antenna is suitable for multi-band MIMO and UWB MIMO antenna system and other future communication devices. In the future, we will focus on the improvement of the isolation and the design of the reconfigurable MIMO antenna. Such a model of multi-band/UWB MIMO antenna might be constructive for developing universal ultra-wideband MIMO antenna and multi-band MIMO.

ACKNOWLEDGMENT

This paper is also supported by the National Nature Science Fund of China (No.60902014), Nature Science Fund of Heilongjiang (QC2009C66) and the Fundamental Research Funds for the Central Universities (HEUCF1208). The authors are also thankful to Hebei VSTE Science and Technology Co., Ltd. for providing the measurement facility.

REFERENCES

[1] *Federal communications commission, First report and order, Revision of Part 15 of commission's rule regarding UWB transmission system FCC 02-48*, Washington, DC, April 22, 2002.

[2] K. Kiminami, A. Hirata, and T. Shiozawa, "Double-sided printed bow-tie antenna for UWB communications," *Antennas and Wireless Propagation Letters*, vol. 3, pp. 152-153, 2004.

[3] Y. S. Li, X. D. Yang, C. Y. Liu, and T. Jiang, "Compact CPW-fed ultra-wideband antenna with band-notched characteristics," *Electronics Letters*, vol. 46, no. 23, pp. 1533-1534, 2010.

[4] J. Liang, C. C. Chiau, X. Chen, and C. G. Parini, "Study of a printed circular disc monopole antenna for UWB systems," *IEEE Trans. Antennas and Propagation*, vol. 53, no. 11, pp. 3500-3504, 2005.

[5] R. Azim, M. T. Islam, and N. Misran, "Design of a planar UWB antenna with new band enhancement technique," *Appl. Comp. Electro. Society Journal*, vol. 26, no. 10, pp. 856-862, 2011.

[6] S. Sadat, M. Fardis, F. Geran, G. Dadashzadeh, N. Hojjat, and M. Roshandel, "A compact microstrip square-ring slot antenna for UWB applications," *IEEE Int. Symposium Antennas and Propagation Society*, 9-14 July, 2006.

[7] X. L. Bao and M. J. Amman, "Investigation on UWB printed monopole antenna with rectangular slitted ground plane," *Microwave and Optical Technology Letters*, vol. 49, no. 7, pp. 1585-1587, 2007.

[8] D. S. Javan and O. H. Ghouchani, "Cross slot antenna with U-shaped tuning stub for ultra wideband applications," *Appl. Comp. Electro. Society Journal*, vol. 24, no. 4, pp. 427-432, 2009.

[9] Y. Li, W. Li, and R. Mittra, "A cognitive radio antenna integrated with narrow/ultra-wideband antenna and switches," *IEICE Electronics Express*, vol. 9, no. 15, pp. 1273-1283, 2012.

[10] G. Zhang, J. S. Hong, B. Z. Wang, and G. Song, "Switched band-notched UWB/ WLAN monopole antenna," *Appl. Comp. Electro. Society Journal*, vol. 27, no. 3, pp. 256-260, 2012.

[11] Y. Li, W. Li and W. Yu, "A switchable UWB slot antenna using SIS-HSIR and SIS-SIR for multi-mode wireless communications applications," *Appl. Comp. Electro. Society Journal*, vol. 27, no. 4, pp. 340-351, 2012.

[12] R. Fallahi, A. A. Kalteh, and M. G. Roozbahani, "A novel UWB elliptical slot antenna with band-notched characteristics," *Progress In Electromagnetics Research*, vol. 82, pp. 127-136, 2008.

[13] K. S. Ryu and A. A. Kishk, "UWB antenna with single or dual band-notches for lower WLAN band and upper WLAN band," *IEEE Trans. Antennas and Propagation*, vol. 57, no.12, pp. 3942-3950, 2009.

[14] Y. Li, X. Yang, C. Liu, and T. Jiang, "Miniaturization cantor set fractal ultra-wideband antenna with a notch band characteristic," *Microwave and Optical Technology Letters*, vol. 54, no. 5, pp. 1227-1230, 2012.

[15] Y. Kim and D. H. Kwon, "CPW-fed planar ultra wide band antenna having a frequency band notch function," *Electronics Letters*, vol. 40, no.7, pp. 403-405, 2004.

[16] J. Kim, C. S. Cho, and J. W. Lee, "5.2 GHz notched ultra-wideband antenna using slot-type SRR," *Electronics Letters*, vol. 42, no. 6, pp. 315-316, 2006.

[17] A. Najam, Y. Duroc, and S. Tedjni, "UWB MIMO antenna with novel stub structure," *Progress In Electromagnetics Research C*, vol. 19, pp. 245-257, 2011.

[18] M. Jusoh, M. F. Jamlos, M. R. Kamarudin, and F. Malek, "A MIMO antenna design challenges for UWB application," *Progress In Electromagnetics Research B*, vol. 36, pp. 357-371, 2012.

[19] Y. Li, W. Li, C. Liu, and T. Jiang, "A printed diversity cantor set fractal antenna for ultra wideband communication applications," *The 10th Int. Symposium Antenna, Propagation, and EM Theory*, 22-26 October, Xi'an China, 2012.

[20] M. Han and J. Choi, "Dual-band MIMO antenna using a symmetric slotted structure for 4G USB dongle application," *IEEE Int. Symposium Antennas and Propagation (APSURSI)*, 3-8 July, 2011.

[21] Y. Li, W. Li, C. Liu, and T. Jiang, "Two UWB-MIMO antennas with high isolation using sleeve coupled stepped impedance resonators," *Asia-Pacific Conference Antennas and Propagation (APCAP)*, 27-29 August, Singapore, 2012.

[22] S. Zhang, Z. Ying, J. Xiong, and S. He, "Ultra wide band MIMO/diversity antennas with a tree-like structure to enhance wideband isolation," *Antennas and Wireless Propagation Letters*, vol. 8, pp. 1279-1282, 2009.

[23] A. R. Mallahzadeh, S. Es'haghi, and A. Alipour, "Design of an E-shaped MIMO antenna using IWO algorithm for wireless application at 5.8 GHz," *Progress In Electromagnetics Research*, vol. 90, pp. 187-203, 2009.

[24] R. A. Bhatti, J. W. Choi, and S. O. Park, "Quad-band MIMO antenna array for portable wireless communications terminals," *Antennas and Wireless Propagation Letters*, vol. 8, pp. 129-132, 2009.

[25] A. R. Mallahzadeh, S. Es'haghi, and H. R. Hassan, "Compact U-array MIMO antenna designs using IWO algorithm," *Int. Journal of RF and Microwave Computer-Aided Engineering*, vol. 19, no. 5, pp. 568-576, 2009.

[26] S. Zhang, B. K. Lau, Y. Tan, Z. Ying, and S. He, "Mutual coupling reduction of two PIFAs with a T-shape slot impedance transformer for MIMO mobile terminals," *IEEE Trans. Antennas and Propagation*, vol. 60, no. 3, pp. 1521-1531, 2012.

[27] I. Kim, C. Jung, Y. Kim, and Y. Kim, "Low-profile wideband MIMO antenna with suppressing mutual coupling between two antennas," *Microwave and Optical Technology Letters*, vol. 50, no. 5, pp. 1336-1339, 2008.

[28] G. Chaudhary, P. Kim, Y. Jeong, J. Lim, and J. Lee. "Analysis and circuit modeling method for defected microstrip structure in planar transmission lines," *Asia-Pacific Microwave Conference*, pp.999-1002, 2011.

[29] S. Fallahzadeh, H. Bahrami, A. Akbarzadeh, and M. Tayarani, "High-isolation dual-frequency operation patch antenna using spiral defected microstrip structure," *Antennas and Wireless Propagation Letters*, vol. 9, pp. 122-124, 2010.

[30] M. Kazerooni, A. Cheldavi, and M. Kamarei, "Analysis, modeling, and design of cascaded defected microstrip structure for planar circuits," *Int. Journal of RF and Microwave Computer-Aided Engineering*, vol. 20, no. 2, pp. 171-181, 2010.

[31] D. La, Y. Lu, and S. Sun, "Novel band stop filter using dual-U shaped defected microstrip structure," *Int. Symposium Signals, Systems and Electronics*, pp. 1-3, 2010.

[32] M. Naser-Moghadasi, M. Alamolhoda, and B. Rahmati, "Spurious-response suppression in microstrip parallel-coupled bandpass filters by using defected microstrip structures," *IEICE Electronics Express*, vol. 8, pp. 70-75, 2011.

[33] A. Nouri and G. R. Dadashzadeh, "A compact UWB band-notched printed monopole antenna with defected ground structure," *Antennas and Wireless Propagation Letters*, vol. 10, pp. 1178-1181, 2011.

[34] S. Zhang, J. K. Xiao, Z. H. Wang, and Y. Li, "Novel microstrip low-pass filters using a defected microstrip structure," *Microwave Journal*, vol. 49, pp. 118-128, 2006.

[35] H. Cao, W. Guan, S. He, and L. Yang, "Compact lowpass filter with high selectivity using g-shaped defected microstrip structure," *Progress In Electromagnetics Research Letters*, vol. 33, pp. 55-62, 2012.

[36] J. Wang, H. Ning, L. Mao, and M. Li, "Miniaturized dual-band bandstop filter using defected microstrip structure and defected ground structure," *IEEE MTT-S International Microwave Symposium Digest (MTT)*, Montreal, QC, Canada, 2012.

[37] D. Cheng, H.C. Yinc, and H.X. Zheng, "A compact dual-band bandstop filter with defected microstrip slot," *Journal of Electromagnetic Waves and Applications*, vol. 26, no. 10, pp. 1374-1380, 2012.

[38] W. Yu, X. Yang, Y. Liu, et al., *Advanced FDTD Methods: Parallelization, Acceleration and Engineering Applications*, Artech House, 2011,

Yingsong LI received his B.Sc. degree in Electrical and Information Engineering in 2006, and M.Sc. degree in Electromagnetic Field and Microwave Technology from Harbin Engineering University, 2006 and 2011, respectively. Now he is a Ph.D. Candidate in Harbin Engineering University, China. He is a student member of Chinese Institute of Electronics (CIE), IEEE, IEICE and The Applied Computational Electromagnetics Society (ACES). His recent research interests are mainly in microwave theory, small antenna technologies and computational electromagnetics. He serves as reviewers for the journals IEEE Antennas and Wireless Propagation Letters, IEEE Transactions on Electromagnetic Compatibility, Electronics Letters, International Journal of Electronics, Progress In Electromagnetics Research Series, Journal of Electromagnetic Waves and Applications, COMPEL: The International Journal for Computation and Mathematics in Electrical and Electronic Engineering, Wireless Personal communications and Applied Computational Electromagnetics Society Journal. He is also a reviewer of Asia-Pacific Conference on Applied Electromagnetics (APACE2012).

Wenxing LI received the B.Sc. and M.Sc. degrees from Harbin Engineering University, Harbin, Heilongjiang, China, in 1982, 1985, respectively. He is currently a full professor of College of Information and Communication Engineering, Harbin Engineering University, China. He is also the head of Research Centre of EM Engineering & RF Technology. He visited the Department of Electrical Engineering, The Pennsylvania State University, USA from June to August 2010. And he visited Oriental Institute of Technology, Taiwan from August to October, 2010. He is also the organizer of the 30th Progress in Electromagnetics Research Symposium (PIERS), IEEE International Workshop on Electromagnetics (iWEM) , TPC of 2012 Asia-Pacific Symposium on Electromagnetic Compatibility (APEMC 2012) and 2012 Global Symposium on Millimeter Waves (GSMM 2012). His recent research interests are mainly in computational electromagnetic, microwave engineering, modern antenna design and microwave and millimeter wave circuits.

Wenhua Yu joined the Department of Electrical Engineering of the Pennsylvania State University, and has been a group leader of electromagnetic communication lab since 1996. He received his PhD in Electrical Engineering from the Southwest Jiaotong University in 1994. He worked at Beijing Institute of Technology as a Postdoctoral Research Associate from February 1995 to August 1996. He has published one book on CFDTD software and two FDTD books: Conformal Finite-Difference Time-Domain Maxwell's Equations Solver: Software and User's Guide (Artech House, 2003), Parallel Finite-Difference Time-Domain (CUC Press of China, 2005, in Chinese), and Parallel Finite-Difference Time-Domain Method (Artech House, 2006). He has published over 100 technical papers and four book chapters. He developed and created the Computer and Communication Unlimited company (Http://www.2comu.com), and serves as its President. He is a Senior Member of the IEEE. He was included in Who' Who in America, Who' Who in Science and Engineering, and Who's Who in Education. He is also a visiting professor and PhD advisor of the Communication University of China. Dr. Yu's research interests include computational electromagnetic, numerical techniques, parallel computational techniques, and the theory and design of parallel computing systems.

Ultra-Wideband Bandpass Filter Based on Parallel-Coupled Microstrip Lines and Defected Ground Structure

Li Yang, Yang Hongchun, Wang Yawei, and Xiao Shaoqiu

School of Physical Electronics
University of Electronic Science and Technology of China, Chengdu, 610054, China
liyang8311@gmail.com, yhc690227@sina.com, and wangyawei667@126.com

Abstract ─ A compact planar microstrip bandpass filter with 3.1 GHz – 10.6 GHz bandwidth, below 1 dB in-band insertion loss, 0.2 ns – 0.6 ns group delay and out-of-band rejection level better than -10 dB is presented for ultra-wideband (UWB) applications. The desired UWB is realized by etching a defected ground structure (DGS) in the ground plane and loading a folded stepped-impedance stub by one of the coupling microstrip lines. This can offer two transmission zeros at lower and upper edges of the passband, which improve the passband selectivity and out-of-band rejection significantly. An equivalent lumped circuit model is introduced; the result of the circuit model fits the EM model well. The simulated and measured results are in good agreement

Index Terms - Bandpass filter, coupled microstrip lines, defected ground structure (DGS), and folded stepped-impedance stub.

I. INTRODUCTION

The ultra-wideband bandpass filter with compact size, low insertion loss, and good out-of-band rejection is always an interesting research field since the standard of ultra-wideband (UWB) communications was published by the Federal Communications Committee (FCC) in 2002 [1]. The multiple-mode resonator (MMR) [2, 3] and the defected ground structure [4-7] were adopted to implement the ultra-wideband bandpass filter. The bandwidth of the proposed filters covers the whole UWB but the insertion loss and the rejection band need further improvement. A wideband bandpass filter with simple structure and good performance based on the hybrid microstrip and coplanar waveguide (CPW) was suggested in [8], but the out-of-band rejection level at the upper frequency edge was poor.

II. UWB BANDPASS FILTER DESIGN

The structure and dimensions of the proposed UWB bandpass filter is shown in Fig. 1 (a) and (b). A folded stepped-impedance stub is loaded by one of the coupled microstrip lines and a DGS structure with two slots etched in the ground plane below the coupled transmission lines. The dimensions of Fig. 1 (b) are enlarged in order to show the structure clearly. A Rogers duroid 5880 substrate is used with thickness of 0.508 mm and relative permittivity 2.2. The folded stepped-impedance stub offers a transmission zero at the lower frequency edge and the DGS structure with two slots generates the other transmission zero at the upper frequency edge of the bandpass filter.

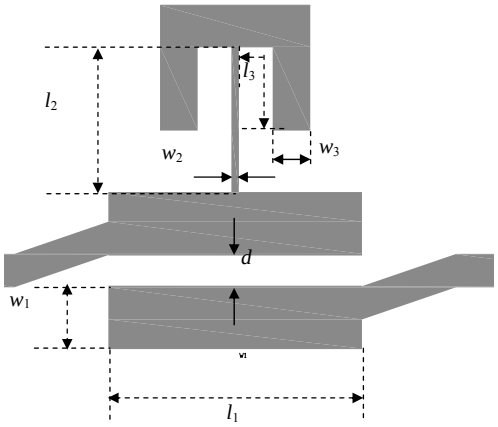

(a) Top view.

Submitted On: July 15, 2012
Accepted On: Jan. 3, 2013

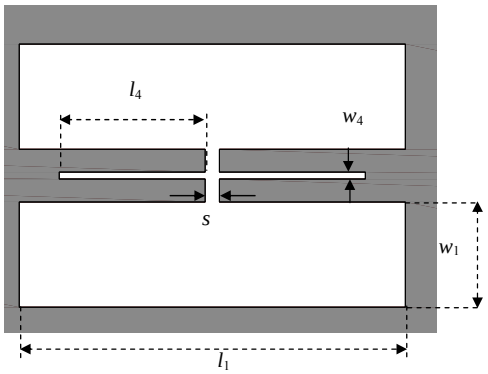

(b) Bottom view.

Fig. 1. Structure and dimensions of the proposed UWB bandpass filter for (a) coupled microstrip lines with folded stepped-impedance stub and (b) DGS with two slots.

The center frequency and the bandwidth of the proposed filter are mainly decided through the length of l_1 and the width of w_1. Figure 2 presents the simulation results of the S-parameters generated using HFSS™. Figure 2 (a) shows that the bandwidth is widened significantly when the length of l_1 is increased while the width of w_1 is fixed. Similarly, Fig. 2 (b) suggests that the bandwidth is also widened slightly when the width of w_1 decreased while the length of l_1 is fixed. The bandwidth covers 3.1 GHz – 10.6 GHz while the length of l_1 is about a half wavelength (13.5 mm) corresponding to the center frequency and the width of w_1, which is about 3 mm.

The frequency of the transmission zero at the lower edge is mainly decided by the length of l_2 and l_3 while the ratio of w_2 and w_3 is fixed as 1 : 4 (similar to the analysis of [9]). Figure 3 offers the curves of the S_{21} parameter simulated by HFSS™. The out-of-band rejection level at 3.1 GHz is below -10 dB when $l_2 = 7$ mm and $l_3 = 6$ mm. The frequency of the transmission zero at the upper edge is mainly decided by the length of l_4 when the values of w_4 is smaller than 0.5 mm. Figure 4 presents the curve of S_{21} parameter simulated using HFSS™. The out-of-band rejection level at 10.6 GHz is below -10 dB when $l_4 = 5.1$ mm and $w_4 = 0.3$ mm.

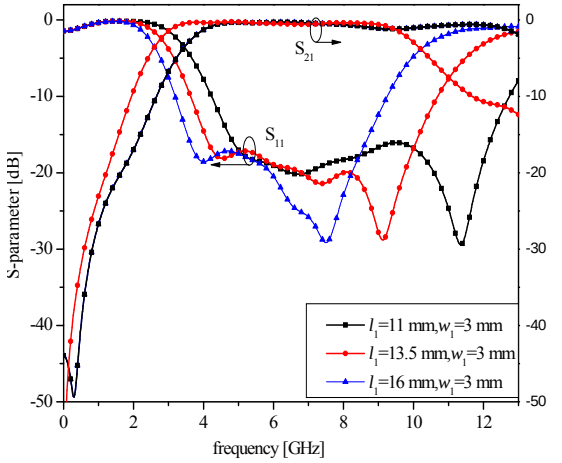

(a)

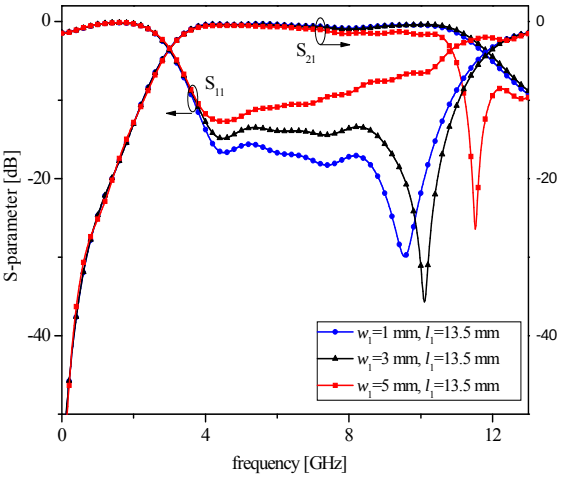

(b)

Fig. 2. (a) The simulated S-parameter curves for different l_1 values and (b) the simulated S-parameter curves for different w_1 values.

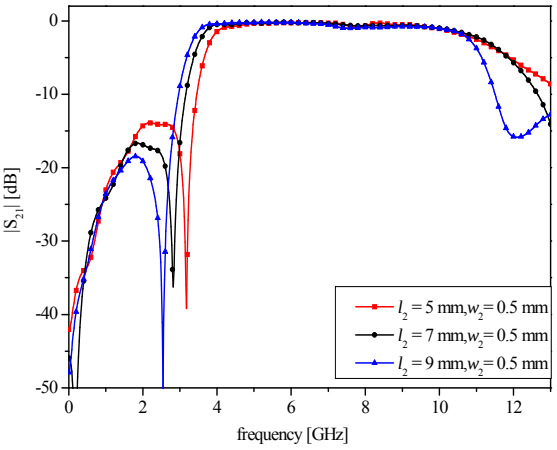

(a)

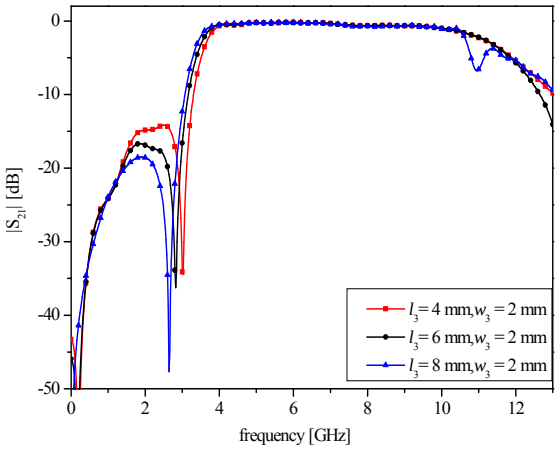

(b)

Fig. 3. (a) The simulated S_{21} for different l_2 values and (b) the simulated S_{21} for different l_3 values.

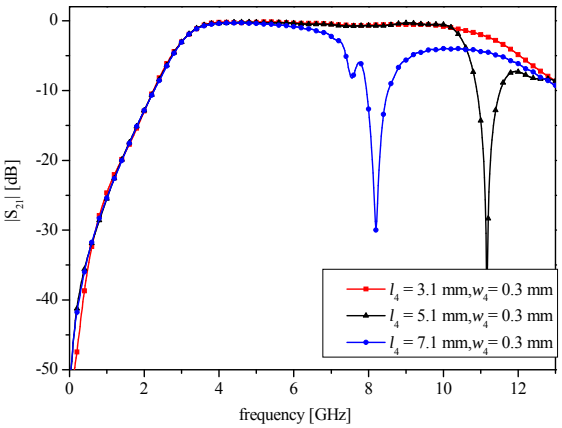

Fig. 4. The Simulated S_{21} for different l_4 values.

In Fig. 5, the surface current distribution of the proposed filter is depicted. In this figure, the current distributions at three different frequencies are presented. The first lower transmission zero is at 2.7 GHz, the upper transmission zero is at 11.3 GHz and the mid-frequency in the passband is at 7 GHz. In Fig. 5 (a), the current is mainly located at the folded stepped-impedance stub. In Fig. 5 (b), the current is mainly located at the DGS. In Fig. 5 (c), the current is uniformly distributed along the filter. This implies that the lower transmission zero is mainly due to the folded stepped-impedance stub, while the DGS introduces the upper transmission zero.

In order to further explain the roles of the proposed folded stepped-impedance stub and the defected ground structure, an equivalent lumped circuit model is introduced. Figure 6 shows the schematic diagram of the equivalent circuit. The 1st part of the circuit represents the folded stepped impedance stub, which introduces the first transmission zero at low frequency. The 2nd part represents the bandpass characteristics of the coupled microstrip lines. Finally, the 3rd part represents the role of the defected ground structure, which introduces the second transmission zero at high frequency. The capacitors and inductors in the 3rd part represent the resonant characteristic of the DGS. The resistors R1 and R2 represent the radiation losses when the operating frequency is high.

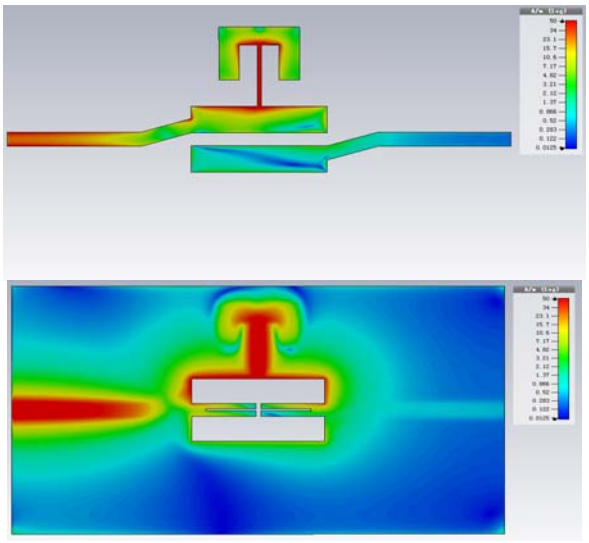

(a)

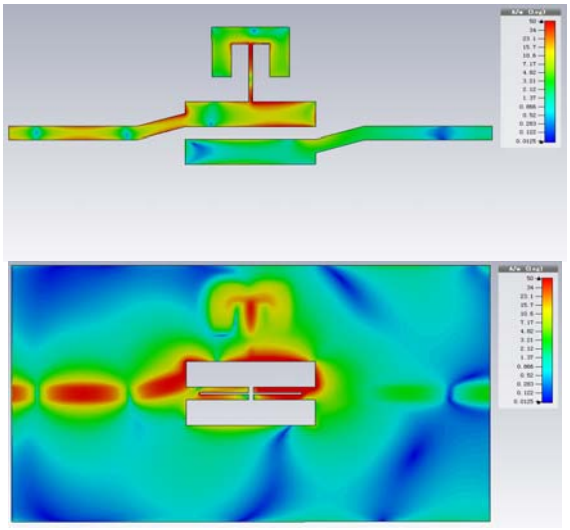

(b)

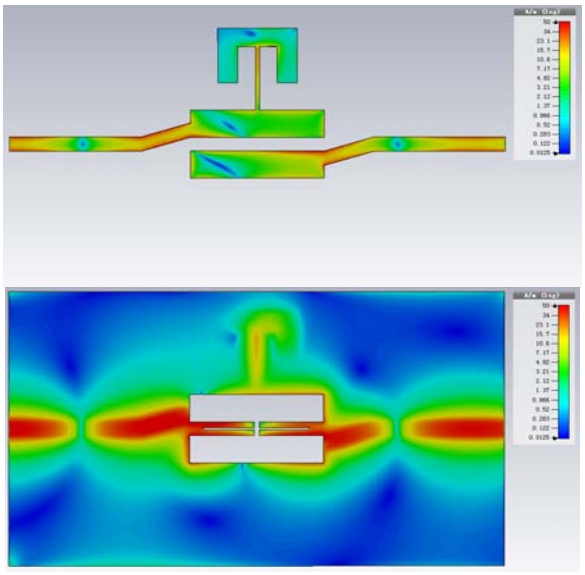

(c)

Fig. 5. The current distribution of the top plane and the ground plane at (a) 2.7 GHz, (b) 11.3 GHz, and (c) 7 GHz.

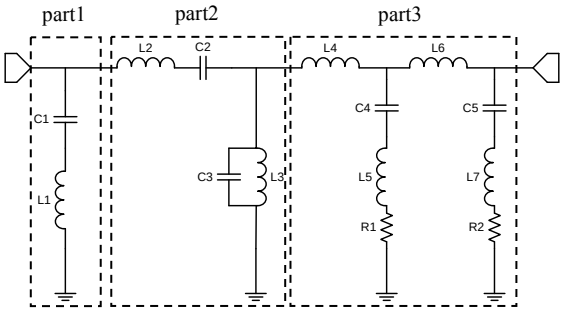

Fig. 6. The equivalent lumped circuit model.

The parameters of the equivalent lumped circuit are as follows: C1 = 1.45 pF, L1 = 2.4 nH, L2 = 0.82 nH, C2 = 0.68 pF, L3 = 1.878 nH, C3 = 0.538 pF, L4 = 0.251 nH, C4 = 0.123 pF, L5 = 1.63 nH, R1 = 0.66 Ohm, L6 = 0.64 nH, C5 = 0.197 pF, L7 = 0.714 nH, R2 = 2.36 Ohm.

Figure 7 shows the S parameters simulated using the equivalent circuit model and the EM model simulator. One can notice that both results are in good agreement.

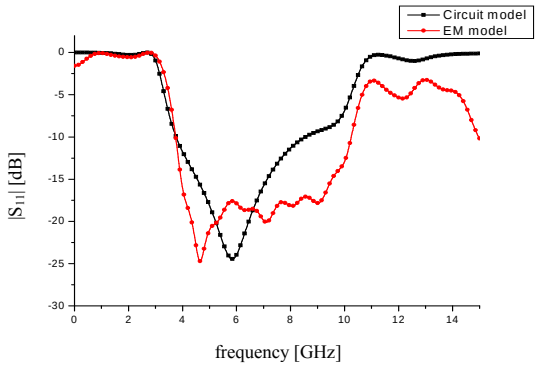

(a)

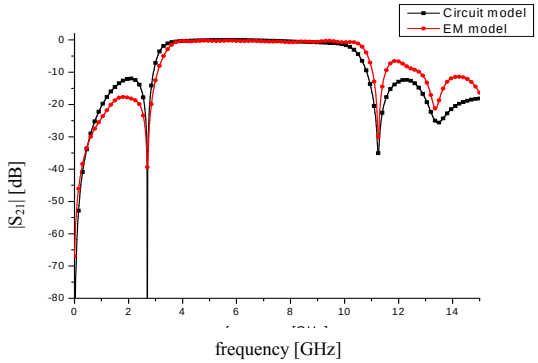

(b)

Fig. 7. The simulated (a) S_{11} and (b) S_{21} parameters of the circuit model versus EM model.

III. RESULT AND DISCUSSION

The photograph of the top and bottom view of the proposed UWB bandpass filter is shown in Fig. 8. The total size is about 50 mm × 30 mm including two SMA connectors. The optimized parameters of the filter are w_1 = 3.1, w_2 = 0.5, w_3 = 2, w_4 = 0.3, l_1 = 13.5, l_2 = 7, l_3 = 6, l_4 = 5.1, d = 1.5, and s = 0.5 (all in millimeters). The simulated and measured results of the S_{11}, S_{21}, and the group delay are shown in Fig. 9. The experimental results were measured by an Agilent E8363B vector network analyzer. Figure 9 suggests that the working bandwidth of the proposed filter covers the whole UWB bandwidth from 3.1 GHz to 10.6 GHz, with an insertion loss less than 1.5 dB through the whole passband and the in-band group delay is about 0.2 ns – 0.6 ns. The simulated and measured results are in good agreement. The deviation might be introduced by the loss tangent of the substrate material and the parasitic effects of the SMA connectors.

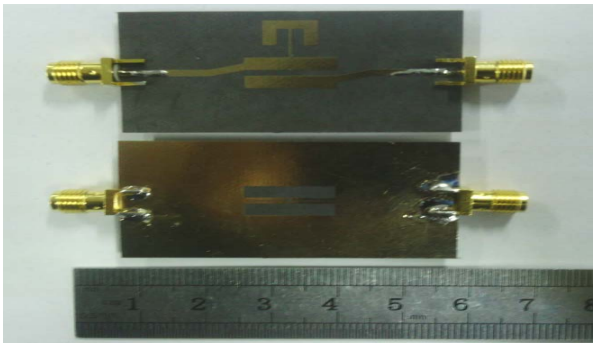

Fig. 8. Photograph of the proposed UWB bandpass filter.

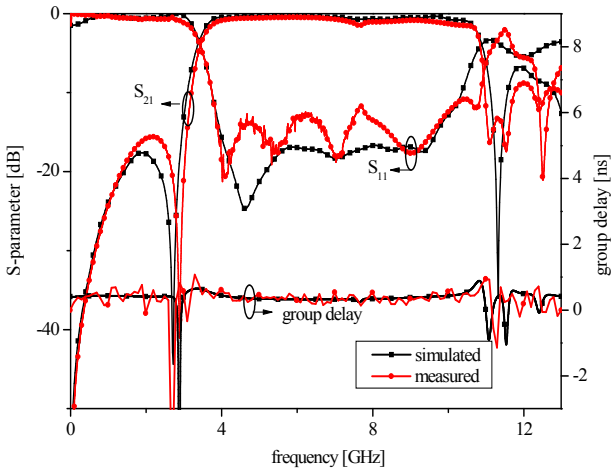

Fig. 9. The simulated and measured S-parameters and the group delay of the proposed filter.

IV. CONCLUSION

In this paper, a structure of a folded stepped-impedance stub with a defected ground structure of two slots is proposed. The proposed configuration introduces two transmission zeros at both, lower and upper edges of the passband. This is in order to improve the out band rejection, and thus the coupled microstrip lines combined with the DGS can cover the whole UWB passband. In order to explain the role of the folded stepped impedance stub and the DGS, an equivalent lumped circuit model is introduced and analyzed. The results of the simulated circuit model, the EM model simulator, and the measurements are in good agreement.

ACKNOWLEDGMENT

This project was supported by the Fundamental Research Funds for the Central Universities.

REFERENCES

[1] FCC, "Revision of part 15 of the commission's rules regarding ultra-wideband transmission systems," *Tech. Rep.,* ET-Docket 98-153, FCC02-48, April 2002.

[2] L. Zhu, S. Sun, and W. Menzel, "Ultra-wideband (UWB) bandpass filter using multiple-mode resonator," *IEEE Microw. Wirel. Compon. Lett.*, vol. 15, no. 11, pp. 796-798, 2005.

[3] K. Wu and X. Zhang, "Development of packaged ultra-wideband bandpass filters," *IEEE Trans. Microw. Theory Tech.*, vol. 58, pp. 220-228, Jan. 2010.

[4] F. Karshenas, A. R. Mallahzadeh, and J. Rashed-mohassel, "Size reduction and harmonic suppression of parallel coupled line bandpass filters using defected ground structure," *Appl. Comp. Electro. Soc. (ACES) Journal*, vol. 25, no. 2, pp. 149-155, Feb. 2010.

[5] M. Al Sharkawy, A.Boutejdar, F. Alhefnawi, and O. Luxor, "Improvement of compactness of lowpass/bandpass filter using a new electromagnetic coupled crescent defected ground structure resonators," *Appl. Comp. Electro. Soc. (ACES) Journal*, vol. 25, no. 7, pp. 570-577, July 2010.

[6] U. Sajjad and A. Sheta, "Compact bandpass filters with bandwidth control using defected ground structure (DGS)," *Appl. Comp. Electro. Soc. (ACES) Journal*, vol. 26, no. 7, pp. 624-630, July 2011.

[7] W. Shao, J.-L. Li, "Accurate modeling of a patterned ground and its application to microwave filters," *Appl. Comp. Electro. Soc. (ACES) Journal*, vol. 27, no. 7, pp. 596-602, July 2012.

[8] L. Zhu, S. Sun, and W. Menzel, "Ultra-wideband (UWB) band-pass filter with hybrid microstrip / CPW structure," *IEEE Microw. Wirel. Compon. Lett.*, vol. 15, no. 12, pp. 844-846, 2005.

[9] L. Zhu and W. Menzel, "Compact microtrip bandpass filter with two transmission zeros using a stub-tapped half-wavelength line resonator," *IEEE Microw. Wirel. Compon. Lett.*, vol. 10, no. 1, pp. 16–18, 2003.

Li Yang received the bachelor's degree and the master's degree from the Information Engineering University and the University of Electronic Science and Technology of China, in 2006 and 2009, respectively. He is currently working toward the Ph.D. degree in the University of Electronic Science and Technology of China.

Wang Yawei was born in Shanxi Province, China, in 1984. He is working toward a master's degree. His research interests include transmission line theory, and microwave passive and active components

Yang Hongchun was born in Sichuan Province, China, in 1969. He received the Ph.D. degree in radio physics from the University of Electronic Science and Technology of China (UESTC), Chengdu, China, in 2008.He is Professor of School of Physical Electronics of UESTC. His current research interests are in the areas of antenna theory and techniques, theoretical physics, electromagnetic science and technology and microwave passive components.

Xiao Shaoqiu received the Ph.D. degree in electromagnetic field and microwave engineering from the University of Electronic Science and Technology of China (UESTC), Chengdu, China, in 2003. From January 2004 to June 2004, he was with the Institute of Applied Physics, UESTC as an Assistant Professor. From July 2004 to March 2006, he was with the wireless Communications Laboratory of NICT Singapore, National Institute of Information and Communications Technology. In April 2006, he became an Associate Professor with UESTC and a Professor in 2010. His research interests include planar antenna and arrays reconfigurable antenna, antenna integration and packaging, millimeter wave circuits and systems and ultrawideband communications.

Compact Lowpass Filter with Wide Stop-Band using Open Stubs-Loaded Spiral Microstrip Resonant Cell

Auob Adinehvand and Ali Lotfi

Computer Engineering Department, Faculty of Engineering, Islamic Azad University,
Kermanshah Branch, Kermanshah, Iran
auobadinehvand@yahoo.com and lotfi_electrical@yahoo.com

Abstract ─ In this paper, a compact lowpass filter using open stubs-loaded spiral compact microstrip resonant cell (OSL-SCMRC) is presented. The proposed resonator is implemented to design the lowpass filter with the wide and high out-of-band rejection in the stop-band region. The lowpass filter has the insertion loss from DC to 5.29 GHz better than -0.1 dB and the return loss better than -19.3 dB. Moreover, the lowpass filter is shown to suppress the harmonics with -20 dB attenuation level from 6.71 GHz to 16.73 GHz result in a 10.02 GHz rejection band. The proposed resonator has an improved slow-wave factor, low radiation and scattering, with a compact size. The filter is designed, fabricated and measured. There is a good agreement between the measured and the simulated S-parameters.

Index Terms ─ Low insertion loss, lowpass filter, microstrip resonator cell, open stubs-loaded, and wide stop-band.

I. INTRODUCTION

Microstrip lowpass filter (LPF) with low insertion loss and broad stop-band are in high demand for the microwave communication systems. To meet the size requirement of the modern microwave circuits, several techniques have been proposed. One of the most interesting and popular techniques is planar resonators. These resonators due to their compact size and easy fabrication have been taken into consideration for the microwave filter design increasingly. Moreover, this resonator has a shortcoming such as: high insertion loss in the pass-band, restricted stop-band, and return loss that limits the engineering applications of these resonators, hence several methods are employed to overcome these drawbacks.

One of the interested with high demanded techniques for the syntheses of the microstrip LPF is the structure that use the photonic band gap (PBG). The one-dimension (1-D) compact microstrip resonant cell (CMRC) was presented in [1]. The use of one-dimensional (1-D) photonic band gap cell exhibits remarkable slow-wave and bandstop performance with quasi–lumped circuit element. Spiral compact microstrip resonant cell (SCMRC) and compensated spiral compact microstrip resonant cells (C-SCMRC) are proposed in [2] and [3], respectively. It has been shown that the resonator can further enhance the slow-wave effect for the circuit size reduction and enlarge the stop-band bandwidth for better performance, and it can achieve the goal of the deep suppression of harmonics. The rectangular patch CMRC (RPCMRC) and defected ground structure are proposed in [4], while the CMRC based on the defected ground structure is proposed in [5]. However, these two structures owing to etching in the ground plane cannot have application on the metal surface and cannot give a robust mechanical endurance against the strain. A tapered periodical CMRC topology with non-uniform cell dimension is proposed to develop a lowpass filter [6].

The lowpass filter using a SCMRC proposed in [7] suffers from two drawbacks, i.e., high insertion loss in the pass-band and a restricted stop-band. Other types of the CMRC configurations have been proposed such as: a slit-loaded tapered CMRC (SL-TCMRC) in order to develop a lowpass filter [8], a front coupled

Submitted On: Sep. 11, 2012
Accepted On: Dec. 21, 2012

tapered CMRC (FC-TCMRC) [9], and a comb compact microstrip resonant cell (CCMRC) [10]. Other techniques have been proposed for the syntheses of the microstrip lowpass filter such as: the miniaturized stepped impedance [11], open loop resonators [12], triangular patch resonator with fractal defection [13], the meander open-loop resonator for syntheses of lowpass filter [14], and photonic band-gap structure (PBG) [15-20]. Although, all these structures have low insertion loss and compact size, the wide stop-band with its superior suppression remain the main challenge for the proposed filters. The open stub-loaded spiral compact microstrip resonant cell (OSL-SCMRC) is proposed in order to design a lowpass filter with low insertion loss in the pass-band, with a wide stop-band and compact size.

The proposed structure is simulated using an EM-simulator (ADS), fabricated and measured. The simulation and measurement results show enhanced performance of the designed filter in the pass-band and stop-band regions. Both results are illustrated, and good agreement between them is achieved.

II. DESIGN OF THE FILTER STRUCTURE

Figure1 shows our designed, open stubs-loaded spiral compact microstrip resonant cell (OSL-SCMRC). The inductance and capacitance obtained from CMRC will be enhanced without any additional lumped components. Due to the added transmission zeros in the stop-band, the new resonator has extended stop-band and improved slow-wave characteristics, which leads to circuit size reduction.

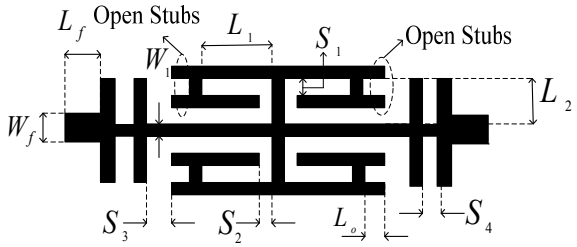

Fig. 1. Schematic diagram of the proposed OSL-SCMRC.

The transmission-line model of the proposed open stubs-loaded spiral compact microstrip resonant cell (OSL-SCMRC) is shown in Fig. 2.

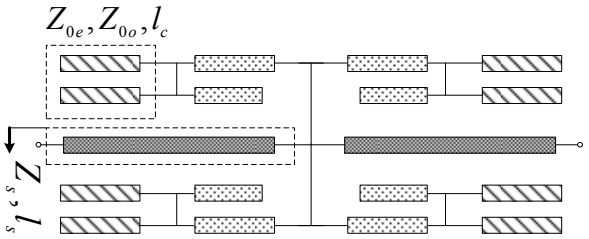

Fig. 2. Transmission line model of the proposed OSL-SCMRC.

It can be noticed from Fig. 2 that the model is composed of two-coupled transmission lines and a central narrow micorstrip line. The equivalent circuit of the two coupled transmission lines and a single transmission line model are shown in Fig. 3 (a) and (b), respectively.

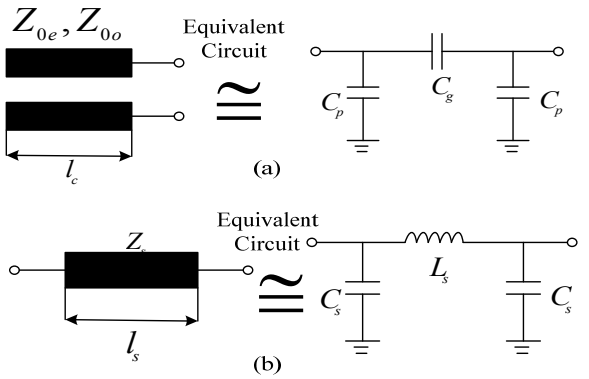

Fig. 3. (a) Two-coupled transmission line model with its equivalent circuit, (b) Single transmission line model with its equivalent circuit.

The symmetric parallel coupled lines are modelled as an equivalent capacitive π-network and the *ABCD* matrix of the lossless parallel coupled lines is expressed as [21],

$$\begin{bmatrix} A_1 & B_1 \\ C_1 & D_1 \end{bmatrix} = \begin{bmatrix} \dfrac{Z_{0e}+Z_{0o}}{Z_{0e}-Z_{0o}} & \dfrac{-j2Z_{0e}Z_{0o}\cot(\beta_c l_c)}{Z_{0e}-Z_{0o}} \\ \dfrac{-j2}{(Z_{0e}-Z_{0o})\cot(\beta_c l_c)} & \dfrac{Z_{0e}+Z_{0o}}{Z_{0e}-Z_{0o}} \end{bmatrix} \quad (1)$$

where β_c is the phase constant of the coupled lines. The *ABCD* matrix of the equivalent capacitive π - network can be obtained as follow,

$$\begin{bmatrix} A_1 & B_1 \\ C_1 & D_1 \end{bmatrix} = \begin{bmatrix} 1+Z_gY_p & Z_g \\ Y_p(2+Z_gY_p) & 1+Z_gY_p \end{bmatrix}. \quad (2)$$

In equation (2), $Z_g = 1/j\omega C_g$ and $Y_p = j\omega C_p$. From equations (1) and (2), the equivalent capacitances of the π -network can be written as,

$$C_g = \frac{Z_{0e} - Z_{0o}}{2\omega Z_{0e} Z_{0o} \cot(\beta_c l_c)}.(F) \quad (3\text{-a})$$

$$C_p = \frac{1}{\omega Z_{0e} \cot(\beta_c l_c)}.(F). \quad (3\text{-b})$$

The single transmission line is shown in Fig. 3 (b), this transmission line can be modelled as an equivalent *L-C* π -network. The *ABCD* matrix can be defined as,

$$\begin{bmatrix} A_2 & B_2 \\ C_2 & D_2 \end{bmatrix} = \begin{bmatrix} \cos(\beta_s l_s) & jZ_s \sin(\beta_s l_s) \\ jY_s \sin(\beta_s l_s) & \cos(\beta_s l_s) \end{bmatrix}. \quad (4)$$

In equation (4) the phase constant and the characteristic admittance of the single transmission line can be defined as β_s and $Y_s = 1/Z_s$, respectively. The *ABCD* matrix of the equivalent *L-C* π -network is defined as,

$$\begin{bmatrix} A_2 & B_2 \\ C_2 & D_2 \end{bmatrix} = \begin{bmatrix} 1+Z_LY_c & Z_L \\ Y_c(2+Z_LY_c) & 1+Z_LY_c \end{bmatrix} \quad (5)$$

where $Z_L = j\omega L_s$ and $Y_c = j\omega C_s$, in which L_s and C_s are the equivalent inductance and capacitance of the single transmission line. The angular frequency is defined as ω, from equations (4) and (5) the value of L_s and C_s are expressed by,

$$L_s = \frac{Z_s \sin(\beta_s l_s)}{\omega}.(H) \quad (6\text{-a})$$

$$C_s = \frac{1-\cos(\beta_s l_s)}{\omega Z_s \sin(\beta_s l_s)}.(F). \quad (6\text{-b})$$

Therefore, the *ABCD* matrix of the proposed resonator can be used to describe the electrical characteristics and performance predication of the open stubs-loaded spiral compact microstrip resonant cell (OSL-SCMRC). It can be clearly observed that increasing the capacitance within the structure is by using a gap between the central narrow line and open stubs, so it can give attenuation poles in the stop-band. Consequently, it will have a wide stop-band. The demonstrated resonator is implemented on (RT/Duroid 5880) substrate with relative permittivity equals to 2.2, thickness of 10 mil, and a loss tangent equals to 0.0009. The simulated S-parameters of the proposed resonator as functions of L_1, L_o and S_1 are shown in Fig. 4 (a), (b), and (c), respectively.

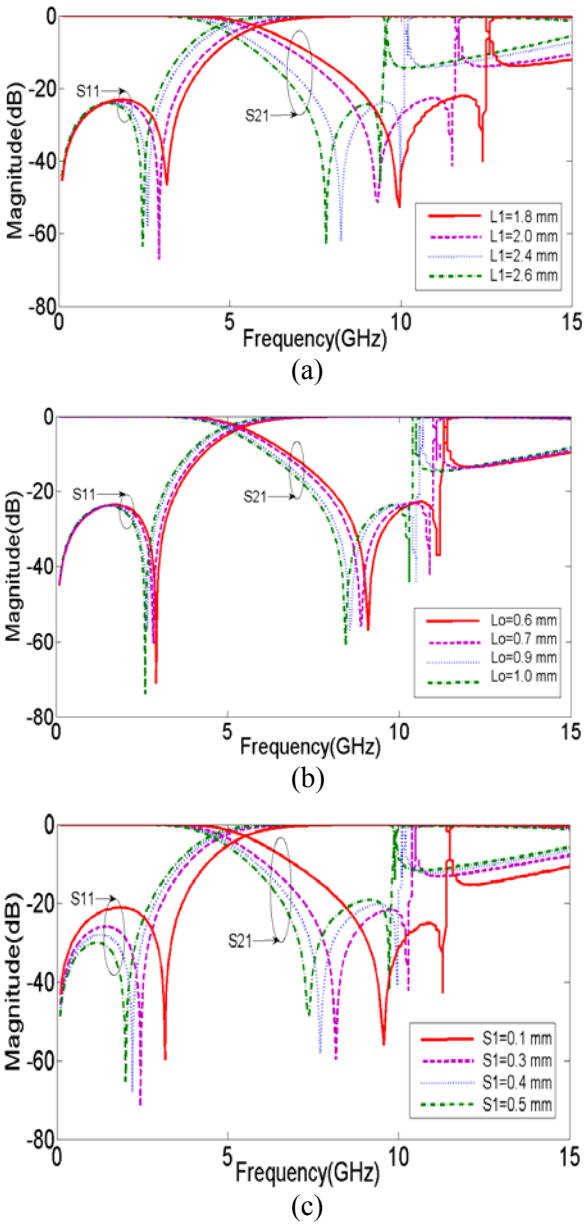

Fig. 4. (a) S-parameters simulation of the proposed resonator as a function of L_1, (b) S-parameters simulation of the proposed resonator as a function of L_o, and (c) S-parameters simulation of the proposed resonator as a function of S_1.

As seen in Fig. 4 (a), when L_1 increases from 1.8 mm to 2.6 mm, the transmission zero at 9.96 GHz approaches the lower frequency. Similarly, in Fig. 4 (b) by decreasing L_o from 1.0 mm to 0.6 mm, the transmission zero at 8.44 GHz starts to move away from the lower frequency. In Fig. 4 (c) by decreasing S_1 from 0.5 mm to 0.1 mm due to the decrement of the effective series inductance, the transmission zero at 7.39 GHz also starts to move away from the lower frequency. Hence, the location of transmission zeros can be controlled by a parallel capacitance with a series inductance, as the attenuation zeros location became lower, which is due to the increment of the series inductance and the decrement of the resonant frequency of the equivalent *LC* circuit. This can be concluded from Fig. 2 and the equivalent circuit elements defined in equation (1) to equation (6).

The two neighbouring open stubs are coupled, which not only enhance the equivalent capacitance of the loading capacitor, but also provide the finite attenuation poles. If the dimensions of the internal open stubs are arbitrarily selected, the harmonics and the spurious will not be suppressed well, and only a narrow rejection bandwidth will be obtained.

Therefore, the internal open stubs need to be optimized. The dimensions of the proposed structure shown in Fig. 1 are as follows: L_1 = 2.2, L_2 = 0.8, L_o = 0.8, S_1 = 0.2, S_2 = 0.2, S_3 = 0.2, S_4 = 0.2, W_1 = 0.2, L_f = 0.7, and W_f = 0.6 (all in mm). The simulated S-parameters of the proposed resonator with these dimensions are shown in Fig. 5, the stop-band has been observed from 7.75 GHz to 10.80 GHz, with -20 dB, and from 6.55 GHz to 10.85 GHz with -10dB attenuation level. The insertion loss from DC to 4.45 GHz is less than -1 dB, and the return loss in the pass-band is better than -28 dB. The return loss in the stop-band is close to 0 dB. Therefore, the small radiation loss can be ignored. The radiation and the scattering effects of the open stubs-loaded spiral compact microstrip resonant cell (OSL-SCMRC) are defined by $1-|S_{11}|^2-|S_{21}|^2$ and are shown in Fig. 6 (a). The radiation and the scattering effects are maintained at low levels while the operating frequency is below 10.9 GHz. The maximum percentage of both, radiation and scattering is 39.44%.

The slow-wave factor (SWF) of the open stubs-loaded spiral compact microstrip resonant cell is defined as follows,

$$SWF = \frac{\lambda_0 \Delta\theta}{360L} + \sqrt{\varepsilon_{eff}} \tag{7}$$

$$\varepsilon_{eff} = \frac{\varepsilon_r + 1}{2} + \frac{\varepsilon_r - 1}{2}\left(1 + 12\frac{h}{W}\right)^{-0.5}, \tag{8}$$

where L and W are the length and width of the microstrip line, respectively. The symbol λ_0 is the free space wavelength, $\Delta\theta$ is the phase difference (in degrees) between the conventional microstrip and the OSL-SCMRC. Finally, ε_{eff} is the effective microstrip permittivity.

Figure 6 (b) shows a comparison between the slow-wave factor (SWF) of the conventional microstrip line and the OSL-SCMRC. It can be seen that the obtained SWF of the conventional microstrip line is 1.357 in the pass-band region at 5.3 GHz, where the proposed OSL-SCMRC increased the SWF by 335.88% to 5.915.

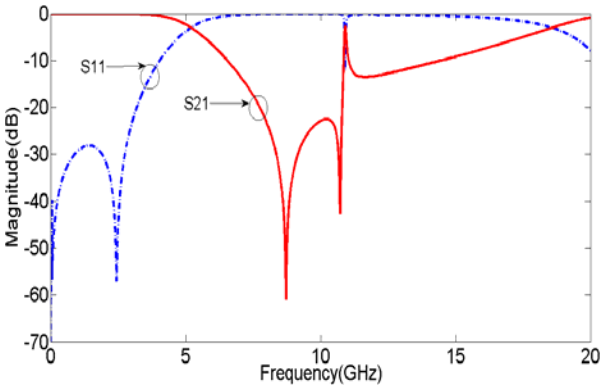

Fig. 5. S-parameter simulation of the proposed resonator.

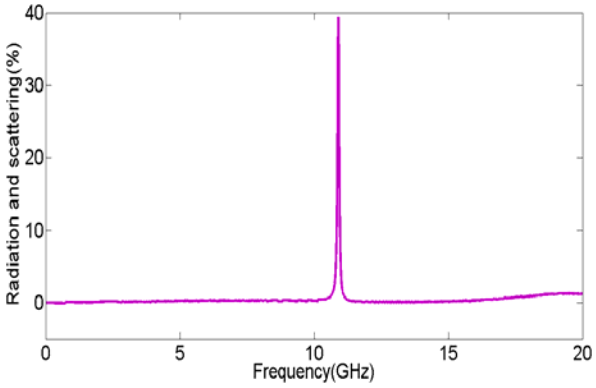

(a)

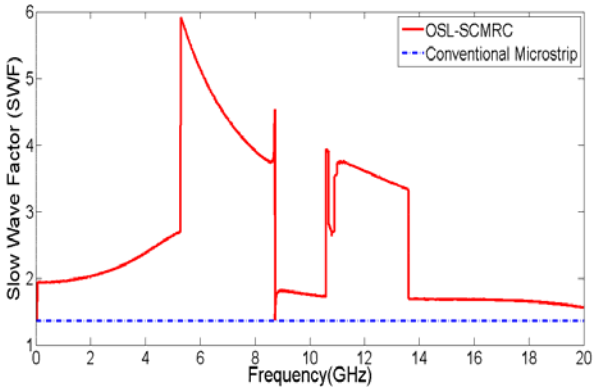

(b)

Fig. 6. (a) Radiation and scattering effects of the proposed OSL-SCMRC and (b) slow-wave factor of the proposed OSL-SCMRC and the conventional microstrip.

The results reveal that the SWF of the conventional microstrip line is improved by using OSL-SCMRC. So the size of the proposed lowpass filter has been reduced as compared to the lowpass filter using the conventional SCMRC. Furthermore, the effect of the coupled capacitance can suppress the first spurious stop-band response near the pass-band, so the actual stop-band of such lowpass filter can be extended.

By connecting several resonators in series form, the periodic structure presents manifest slow-wave effect and bandstop characteristics. The resonators with periodic structures and different dimensions, because of their different cutoff frequency, results in obtaining the lowpass filter with wide stop-band; hence the flaw in stop-band was avoided.

III. SIMULATION AND MEASUREMENT RESULTS

The lowpass filter in the stop-band region exhibits harmonics, thus the stop-band is restricted. To overcome this problem, three resonators with different dimensions cascaded in a series form are designed and their dimensions were optimized to gain a wide stop-band with a compact size. The wide stop-band can be achieved because of the resonators with the multi cutoff frequencies.

The EM–simulator (ADS) is used for the optimization of the dimensions of the resonator to obtain the LPF as shown in Fig. 7, with the desired characteristics.

As shown in Fig. 8 (a) by increasing S_1 from 0.1 mm to 0.4 mm, the S_{21} is attenuated. Therefore, the suppression of the unwanted harmonic in the stop-band can be achieved. In Fig. 8 (b) L_1 has increased from 1.8 mm to 2.6 mm, and the transmission zero at 9.84 GHz has been moved to a lower frequency. Consequently, the transmission zeros in the stop-band can be easily controlled by the dimensions of the proposed resonator. The dimensions of the obtained LPF shown in Fig. 7 are: $L_1 = 2.2$, $S_3 = 0.2$, $S_1 = 0.2$, $L_o = 0.8$, $L_{21} = 1.5$, $L_{22} = 0.5$, $L_{2o} = 0.4$, $S_{21} = 0.1$, $S_{22} = 0.2$, $S_{23} = 0.3$, $S_{24} = 0.1$, $W_{22} = 0.4$, $L_s = 0.3$, $L_f = 1$, and $W_f = 0.6$ (all in mm).

The photograph of the fabricated filter is shown in Fig. 9 (a). The filter has a size of 20 mm × 1.8 mm. The design is verified by an EM-simulator (ADS), and the measurement is done using an Agilent Network Analyzer N5230A. Both simulation and measurement results of the lowpass filter using OSL-SCMRC structure are illustrated in Fig. 9 (b). Obviously, the lowpass filter behaves well in the pass-band and stop-band regions. As seen from Fig. 9 (b), the designed filter has an insertion loss from DC to 5.29 GHz better than -0.1 dB and a return loss better than -19.3 dB and even reaches to -41.5 dB at 2.25 GHz, where the transmission pole is located.

The stop-band region, from 6.71 GHz to 16.73 GHz with -20 dB attenuation level, result in a 10.02 GHz rejection band. This is considered a wide rejection band. The designed filter has two transmission zeros, 7.11 GHz with -56.13 dB and 7.91 GHz with -68.09 dB. This results in a sharp skirt characteristic to the lowpass filter. Obviously, the two symmetrical open stubs-loaded spiral compact microstrip resonant cells (OSL-SCMRC) patches can help to achieve a wide stop-band. Hence our design has low insertion loss, wide stop-band, and a very compact size. The proposed resonator can be easily tuned to the desired frequency by adjusting the length of the open stubs. Therefore, it can be employed in the microwave applications.

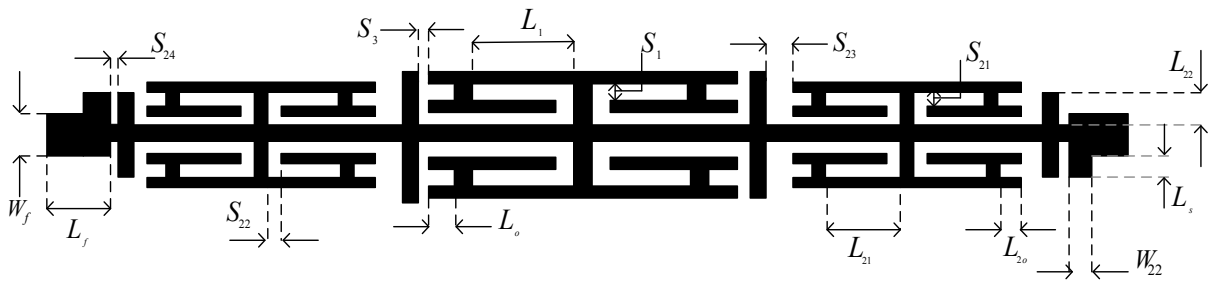

Fig. 7. Schematic diagram of the designed LPF.

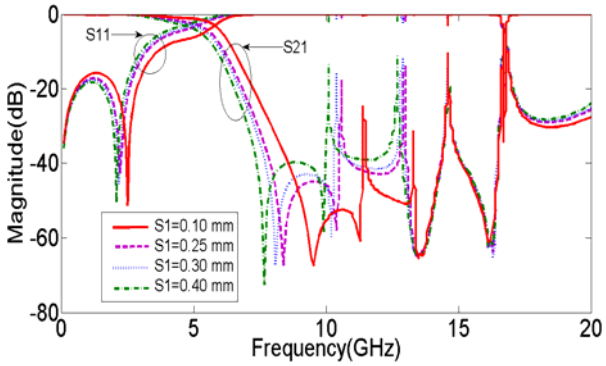

(a)

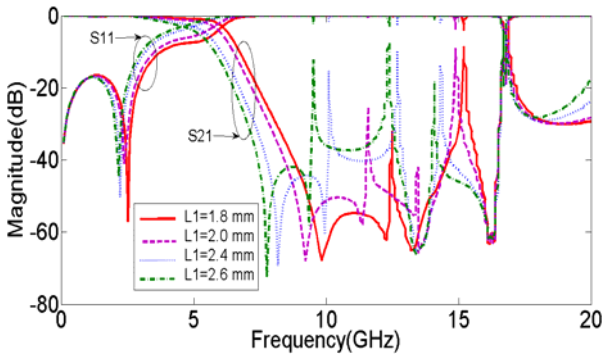

(b)

Fig. 8. Simulated S-parameters of the designed LPF as a function of (a) S_1 and (b) L_1.

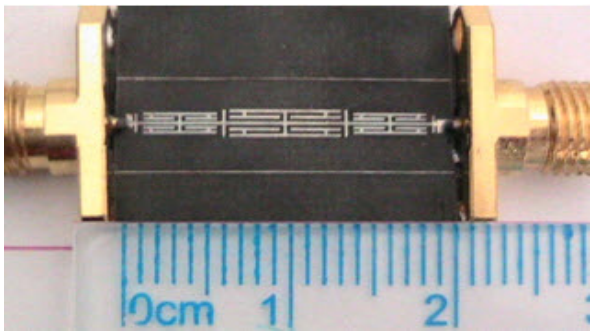

(a)

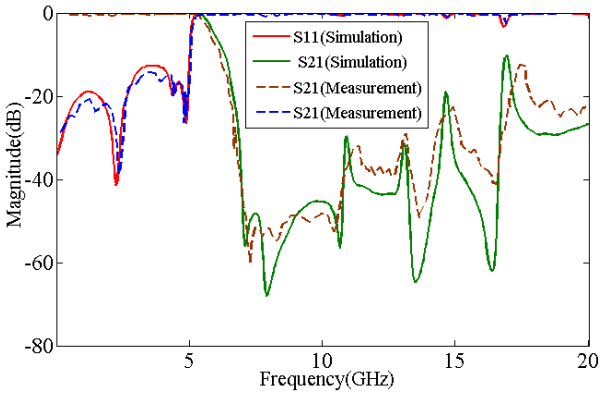

(b)

Fig. 9. (a) The photograph of the fabricated filter and (b) the simulated and measured S-parameters of the proposed LPF.

IV. CONCLUSION

In this work, a novel compact microstrip lowpass filter using an open stubs-loaded spiral compact microstrip resonant cell is presented. The proposed structure of the lowpass filter has some good characteristics. The designed resonator has low radiation and scattering effects due to the lower relative permittivity constant and thinned out substrate. The lowpass filter has low insertion loss in the pass-band region, high return loss, wide stop-band region, and a very compact size. The designed filter uses resonators of different dimensions with different cutoff frequencies, resulting in a wide stop-band. The measured and simulated results are in good agreement. The designed structure can be employed, where lowpass filters with the wide stop-band, high return loss, low insertion loss, and compact size are needed in the microwave applications.

REFERENCES

[1] Q. Xue, K. M. Shum, and C. H. Chan, "Novel 1-D microstrip PBG cells," *IEEE Microwave and Guided Wave Letters*, vol. 10, no. 10, pp. 403-405, Oct. 2000.

[2] T. Y. Yum, Q. Xue, and C. H. Chan, "Novel sub harmonically pumped mixer incorporating dual-band stub and in-line SCMRC," *IEEE Trans. on Microwave Theory and Technique*, vol. 51, no. 12, pp. 2538-2547, Dec. 2003.

[3] J. Gu and X. Sun, "Miniaturization and harmonic suppression rat-race coupler using C-SCMRC resonators with distributive equivalent circuit structure," *IEEE Microwave and Wireless Components Letters*, vol. 15, no. 12, pp. 880-882, Dec. 2005.

[4] S. Dwari and S. Sanyal , "Compact wide stop-band lowpass filter using rectangular patch compact microstrip resonant cell and defected ground structure," *Microwave Optical Technology Letters*, vol. 49, no. 4, pp.798-800, April 2007.

[5] Y. -J. Chen, "Novel compact lowpass filter with CMRC based on defected ground structure," *Microwave Optical Technology Letters*, vol. 48, no. 4, pp.695-697, April 2006.

[6] L. Li, Z. F. Li, and Q. F. Wei, "Compact and selective lowpass filter with very wide stop-band using tapered compact microstrip resonant cells," *Electronic Letters*, vol. 45, no. 5, pp. 267-268, Feb. 2009.

[7] J. Gu and X. Sun, "Compact lowpass filter using spiral compact microstrip resonant cells," *Electronic Letters*, vol. 41, no. 19, pp. 1065-1066, Sep. 2005.

[8] M. Hayati and A. Lotfi, "Elliptic-function lowpass filter with sharp cutoff frequency using slit-loaded tapered compact microstrip resonator cell," *Electronic Letters*, vol. 46, no. 2, pp. 143-144, Jan. 2010.

[9] M. Hayati and A. Lotfi, "Compact lowpass filter with high and wide rejection in stop-band using front coupled tapered CMRC," *Electronic Letters*, vol. 46, no. 12, pp. 846-848, June 2010.

[10] C. F. Zhang, "Compact and wide stop-band lowpass filter with novel comb CMRC," *International Journal of Electronics*, vol. 96, no. 7, pp. 749-754, July 2009.

[11] S. -H. Fu, C. -M. Tong, X. -M. Li, W. Zhang, and K. Shen, "Compact miniaturized stepped impedance low-pass filter with sharp cutoff characteristic," *Microwave Optical Technology Letters*, vol. 51, no. 10, pp. 2257-2258, Oct. 2009.

[12] K. R. Jha and N. Nehra, "Microstrip low-pass filter using open loop resonators," *Microwave Optical Technology Letters*, vol. 50, no. 11, pp. 2983-2986, Nov. 2008.

[13] J. -K. Xiao, Q. -X. Chu, and H. -F. Huang, "New microstrip low pass filter with transmission zero and wide stop-band," *Microwave Optical Technology Letters*, vol. 51, no. 3, pp. 830-831, March 2009.

[14] J. X. Chen and Q. Xue, "A novel compact microstrip lowpass filter using a meander open-loop resonator," *Microwave Optical Technology Letters,* vol. 45, no. 1, pp. 66-67, April 2005.

[15] S. K. Parui and S. Das, "A microstrip filter using split-ring PBG to get wide, deep and sharp stop-band," *International Journal of Electronics*, vol. 94, no. 6, pp. 645-652, June 2007.

[16] M. Al Sharkawy, A. Boutejdar, F. Alhefnawi, and O. Luxor, "Improvement of compactness of lowpass/Bandpass filter using a new electromagnetic coupled crescent defected ground structure (DGS) resonators," *Appl. Comp. Electro. Society (ACES) Journal*, vol. 25, no. 9, July 2010.

[17] R. N. Baral and P. K. Singhal, "Design and analysis of micorstrip photonic band gap filter for suppression of periodicity," *Appl. Comp. Electro. Society (ACES) Journal*, vol. 25, no. 2, Feb. 2010.

[18] A. Boutejdar, M. Challal, and A. Azrar , " A novel band-stop filter using octagonal-shaped patterned ground structures along with interdigital and compensated capacitors ," *Appl. Comp. Electro. Society (ACES) Journal*, vol. 26, no. 4, pp. 312-318, April 2011.

[19] F. Karshenas, A. R. Mallahzadeh, and J. Rashed-Mohassel, "Size reduction and harmonic suppression of parallel coupled-line bandpass filters using defected ground structure," *Appl.*

Comp. Electro. Society (ACES) Journal, vol. 25, no. 2, pp. 149-155, Feb. 2010.

[20] N. M. Garmjani and N. Komjani, "Improved microstrip folded tri-section stepped impedance resonator bandpass filter using defected ground structure," *Appl. Comp. Electro. Society (ACES) Journal*, vol. 25, no. 11, pp. 975-983, Nov. 2010.

[21] M. Sagawa, K. Takahashi, and M. Makimot, "Miniaturized hairpin resonator filters and their application to receiver front-end MIC's," *IEEE Trans. on Microwave Theory and Technique*, vol. 37, no. 12, pp. 1991-1997, Dec. 1989.

Auob Adinehvand was born in kouhdasht, Iran in 1982. He received his B.Sc. in Computer Hardware from Islamic Azad University, Arak, Iran in 2007 and M.Sc. in Computer Systems Architecture from the same university in 2009. He is currently working toward the Ph.D. degree in the Department of Electrical Engineering, RAZI University, Kermanshah, Iran. His research interests include QCA circuit design and Microwave active and passive components.

Ali Lotfi received the B.Sc. degree in Electrical Engineering from the Iran University of Science and Technology (I.U.S.T), Tehran, Iran, in 2004, and the M.Sc. degree in Electronics Engineering from the Department of Electrical Engineering, RAZI University, Kermanshah, Iran, in 2010, (with honors), where, he is currently working toward the Ph.D. degree in Electronics Engineering. His research interests include RF and Microwave active and passive components.

A Miniaturized Microstrip Dual-Band Bandpass Filter using Folded UIR for Multimode WLANs

M. Hayati [1, 2], A. Khajavi [1], and H. Abdi [1]

[1] Department of Electrical Engineering, Faculty of Engineering
University of Razi, Kermanshah, 67149-Iran
mohsen_hayati@yahoo.com, azadeh_khajavi_ee@yahoo.com, and Hamdiabdi@razi.ac.ir

[2] Computational Intelligence Research Center, Faculty of Engineering
University of Razi, Kermanshah, 67149 Iran

Abstract ─ A novel microstrip dual-band bandpass filter (BPF) using folded half-wavelength uniform impedance resonator (UIR) with high selectivity is presented. The proposed filter with two tuneable passbands has advantages such as compact size and simple structure. The passband frequencies have been adjusted for 2.4 GHz and 5.2 GHz wireless local area networks (WLANs). The overall size is reduced by 30 % in comparison with the two section radial stepped impedance resonator (SIR). The measured insertion loss is less than 0.18 dB and 0.5 dB in the first and second passbands, respectively. Also the measured return loss is more than 30 dB and 20.73 dB in the first and second passbands, respectively. There is a good agreement between the measured and the simulated results.

Index Terms ─ Bandpass filter, stepped impedance resonator, and uniform impedance resonator.

I. INTRODUCTION

In recent years, dual-band BPFs are widely used for microwave and wireless systems such as global system for mobile communication (GSM) and (WLAN). The center frequency of the second passband of the conventional half-wavelength UIR is two times of the fundamental frequency, so it seriously suffers from unwanted harmonics and has a large size. To solve this problem, the use of non-uniform line resonators such as two section SIRs is considered [1]. So an SIR exhibits advantages in the size reduction and good harmonics suppression as compared to a UIR. The filter in [1] with three SIRs has a minimum insertion loss of 2dB in the fundamental passband. In [2], a highly selective dual-band BPF is presented using radial SIR and input-output T-shaped lines with minimum insertion loss of 1.6 dB, 2.2 dB, and 3 dB bandwidth of 2.5 % and 2.2 % in two passbands. In [3], two dual-bands BPF are presented using resonator-embedded cross-coupled structure for GSM (900/1800 MHz) with minimum insertion loss of 3 dB and 4 dB and WLAN (2.4/5.2 GHz) with minimum insertion loss of 2 dB and 2.5 dB in its passbands. In [4], a BPF using a three section SIR with the minimum insertion loss of 2.5 dB at the fundamental frequency is presented. In [5], a compact BPF to suppress spurious harmonics with minimum insertion loss of 1.75 dB and 3 dB bandwidth of 1.8 % at the fundamental frequency (2.22 GHz) is presented using the UIR and three sections SIR.

In all these structures, the length reduction of the SIRs results in the increment of the width, which finally increases the filter size. Also due to cascaded structures [1, 4] and weak coupling between the resonators [2, 3, 5], their insertion losses in the passbands are not good.

In [6], a BPF using folded hairpin octagonal double hairpin-shaped resonators with side coupled structure has achieved compact size due to the slow-wave performance and self-capacitance. But its minimum insertion loss is 2 dB at the fundamental frequency. The stopband

Submitted On: Sep. 15, 2012
Accepted On: Dec. 30, 2012

with the attenuation level of -20 dB is only from DC to 900 MHz and from 940 MHz-1200 MHz. The dual-band BPF in [7] is composed of folded open loop half-wavelength resonators and stepped impedance structures. This filter has a small size, but it has high insertion losses. In [8], pseudo-interdigital SIRs are used to design the BPF with dual-band response. This filter has a large size and high insertion losses. In [9], a dual-band BPF using SIRs is designed. This filter has good harmonics attenuation, but it has large size and high insertion losses. In [10], a triple band BPF using hairpin SIRs is presented. This filter has the advantage of having triple band, but it suffers from having a very large size. Also it has high insertion losses in three passbands in spite of cascaded structure.

In [11, 12], two SIR BPFs using defected ground structure (DGS) are presented. Although, these filters have improved rejection bands, their insertion losses in the passbands are not so good, and their total dimensions by considering two layers are large. Also in the DGS structure, it has not been a robust mechanical endurance against strain due to etching in the ground plane.

In this paper, a new miniaturized dual-band BPF with low insertion loss and high selectivity using folded half-wavelength UIR is presented. The conventional half-wavelength UIR has been folded to eliminate spurious harmonics. By tuning the spaces between the stubs, the second band frequency can be adjusted. Moreover, the modified UIR results in an overall size reduction as compared to the SIR, due to the slow-wave effect.

II. BANDPASS FILTER DESIGN

The conventional half-wavelength UIR is shown in Fig. 1 (a), which is folded to achieve a capacitive loading between the arms and also to minimize the length. This can be shown in Fig. 1 (b) with a good slow-wave performance.

The LC equivalent circuit of the proposed resonator is shown in Fig. 2, where L_a, L_b, L_c, L_d, and L_e represent the inductances of the stubs d_1, d_2, d_3, d_4, and d_5, respectively. Furthermore, C_{g1} is the capacitance of the gap between the stub d_3 and d_5. The capacitances C_{g2} and C_{g3} represent the gap between the centred folded stubs. The capacitance C_p is that of the stub d_5 with respect to the ground.

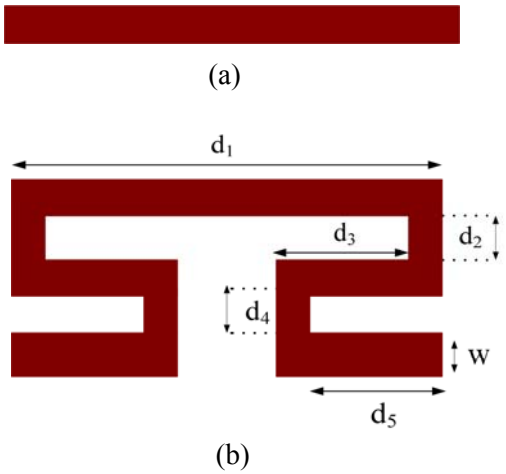

Fig. 1. A schematic view of the (a) conventional UIR and (b) the proposed folded UIR.

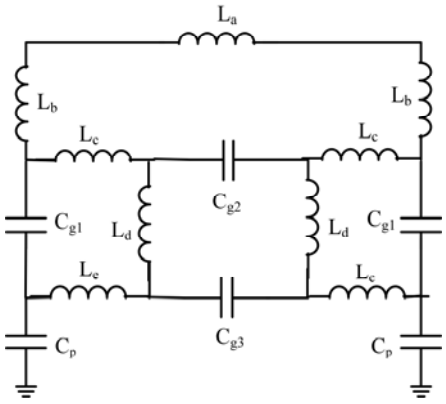

Fig. 2. LC equivalent circuit of the proposed resonator.

A capacitive loaded lossless transmission line resonator is shown in Fig. 3 (a) and its LC equivalent circuit is shown in Fig. 3 (b), where the proportion of the first spurious resonant frequency to the fundamental frequency as shown in [13] is,

$$\frac{f_2}{f_1} = 2\frac{v_{p2}}{v_{p1}} \tag{1}$$

where v_{p1} and v_{p2} are the phase velocities of the loaded line at the fundamental and the first spurious resonant frequencies, respectively. The dispersion equation as shown in [13] is given by,

$$\cos(\beta d) = \cos\theta_a - \frac{1}{2}\omega C_L Z_a \sin\theta_a \tag{2}$$

where C_L, Z_a, β, d and, θ_a are the loaded capacitance, characteristic impedance, the

propagation constant, the length of the unloaded line, and the electrical length, respectively.

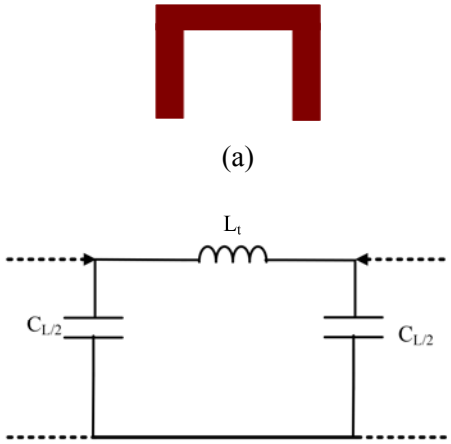

Fig. 3. (a) Capacitively loaded transmission line resonator structure and (b) the LC equivalent circuit of the structure.

By plotting the dispersion curves based on equation (1), it can be shown that the dispersion effect results in the increment of the ratio of the first spurious resonant frequency to the first fundamental [13]. Therefore, this property can be used to design a bandpass filter with a wider upper stopband. Thus, the LC equivalent circuit of the proposed resonator consists of more self-capacitances than the resonator in [13]. This is in order to improve the slow-wave performance.

The electrical length (θ) of a conventional half-wavelength UIR is defined as shown in [14] by equation (3) as follows,

$$\theta = \beta l \qquad (l = \pi) \tag{3}$$

where

$$\beta = 2\pi/\lambda_g\,, \tag{4}$$

$$\varepsilon_{re} = \frac{\varepsilon_r + 1}{2} + \frac{\varepsilon_r - 1}{2}\left(1 + 12\,h/W\right)^{-0.5}, \tag{5}$$

$$\lambda_g = \frac{300}{f(GHz)\sqrt{\varepsilon_{re}}}(mm), \tag{6}$$

where β, l, λ_g , ε_{re}, f, ε_r, W, and h are the propagation constant, physical length, guided wavelength, effective dielectric constant, fundamental frequency, relative dielectric constant, and the width and thickness, respectively. The fundamental frequency is adjusted by the proper physical length at 2.4 GHz, so by changing the total length of the resonator ($d_1 + 2d_2 + 2d_3 + 2d_4 + 2d_5$), the fundamental frequency changes. In the conventional half-wavelength UIR, the spurious frequencies resonate at $f = nf_1$ (n = 2, 3, …). On the other hand, the proposed structure exhibits variations of gaps between the stubs i.e., d_2 and d_4, which results in changing the spurious frequencies, especially the gap d_4 is an effective parameter in controlling the spurious frequencies of the filter.

The S- parameter simulation of the proposed resonator as a function of d_4 is shown in Fig. 4. The decrement of the gap d4, which results in the increment of the capacitive loading, increases the second band frequency. Therefore, the proportion of the centre frequency of the second passband to the fundamental frequency (f_2/f_1) gets bigger.

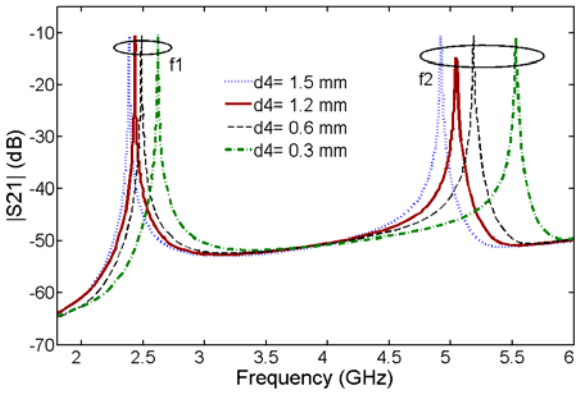

Fig. 4. Simulated insertion loss of the new resonator with varying d_4.

The proposed filter is shown in Fig. 5, where d_4 = 1.2 mm results in f_2/f_1 = 2.16. The T-shaped coupling lines are used to realize parallel coupling to the folded UIRs and also create two finite transmission zeros. The dual-band BPF is designed for two passbands, located at 2.4 GHz and 5.2 GHz. The dimensions of the filter are shown in Fig. 5.

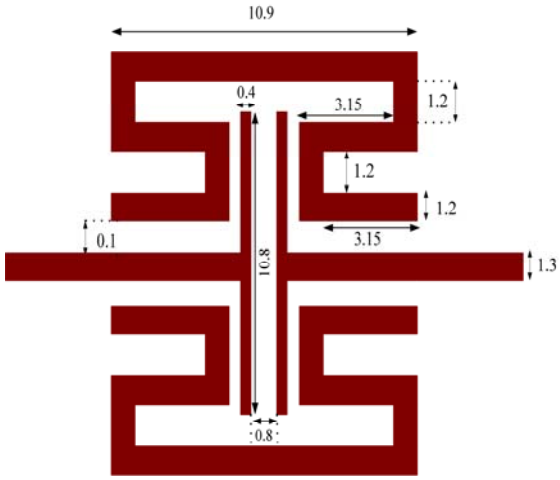

Fig. 5. The layout of the designed filter (unit: in mm).

III. SIMULATED AND MEASURED RESULTS

The photograph of the fabricated filter is shown in Fig. 6 (a). The BPF is fabricated on a substrate with relative dielectric constant of 6.15, thickness of 31 mil and loss tangent equals to 0.0009. The filter is simulated by the method of moments in ADS software. HP8757A network analyzer is used for measurements. The simulated and the measured results are in good agreement as can be shown in Fig. 6 (b).

The measured centre frequencies of the two passbands are located at 2.4 GHz and 5.2 GHz. The measured insertion loss has an improvement of 780 % and 340 % in comparison to the two section radial SIR. Also the measured return loss has an improvement of 36 % and 5 %, in comparison to the two section radial SIR. The 3 dB bandwidth of 3% and 1.3 % is obtained for the two passbands. The return loss in the stopband region is very close to 0 dB, indicating negligibly small radiation loss. The filter size is 10.9 mm × 13.5 mm (0.2 λg × 0.24 λg). A comparison of the designed filter with previous works is shown in Table 1, where IL_1, IL_2, f_1, and f_2 corresponds to the insertion loss in the first passband, insertion loss in second passband, first passband, and the second passband, respectively. It is observed that, the proposed filter has a small size and good performance.

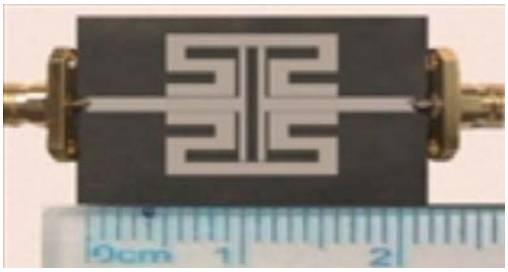

(a)

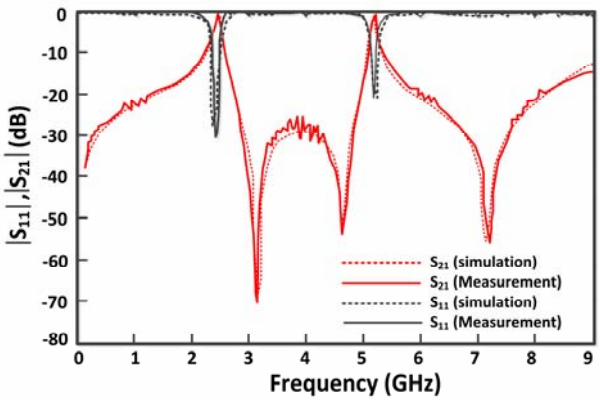

(b)

Fig. 6. (a) The photograph of the fabricated filter and (b) the simulated and measured results of the proposed filter.

Table 1: Comparison between the proposed filter and previous works.

Ref.	Resonator Type	IL_1 (dB)	IL_2 (dB)	f_1 (GHz)	f_2 (GHz)	Size (mm^2)
[2]	two section radial SIR	1.6	2.2	2.45	5.2	209.4
[3]	miniaturized hairpin resonator and stepped impedance hairpin resonator	1.2	2.3	2.4	5.2	850.3
[7]	folded open loop half-wavelength resonators and SIR	0.6	1	2.45	5.7	168.5
[8]	pseudo-interdigital SIRs	0.8	1.2	2.4	5.2	192.9
[9]	SIRs	2.12	2.33	2.45	5.8	1905
Filter	**Folded UIR**	**0.18**	**0.5**	**2.4**	**5.2**	**147.1**

IV. CONCLUSION

In this paper, a miniaturized dual-band BPF using folded half-wavelength UIR with high selectivity is presented for WLAN signals, which has been designed, fabricated, and measured. The proposed resonator has a significant improvement for the insertion loss and the return loss in its passbands. Moreoevr, a favorable size reduction has been achieved.

REFERENCES

[1] M. Makimoto and S. Yamashita, "Bandpass filters using parallel coupled stripline stepped impedance resonators," *IEEE Trans. on Microwave Theory and Techniques*, vol. 28, no. 12, pp. 1413-1417, Dec. 1980.

[2] J. Wang, Y. X. Guo, B. Z. Wang, L. C. Ong, and S. Xiao, "High-selectivity dual-band stepped-impedance bandpass filter," *Electronics Letters*, vol. 42, no. 9, pp. 538-540, April 2006.

[3] S. Chaimool and P. Akkaraekthalinl, "Resonator-embedded four-pole cross-coupled dual-band microstrip bandpass filters," *International Symposium on Communications and Information Technology*, Bangkok, Tailand, pp. 1076-1079, Oct. 2006.

[4] H. Zhang and K. J. Chen, "A tri-section stepped-impedance resonator for cross-coupled bandpass filters," *IEEE Microwave and wireless components letters*, vol. 15, no. 6, pp. 401-403, June 2005.

[5] Y. Wang, B. Z. Wang, and J. Wang, "The design of coupled resonator bandpass filter with wide stop-band," *IEEE Microwave and wireless components letters*, vol. 18, no. 4, pp. 251-253, April 2008.

[6] H. W. Liu and W. M. Li, "Miniaturised microstrip bandpass filter using octagonal hairpin resonators with side-coupled technique," *Electronics Letters*, vol. 44, no. 24, pp. 1410-1411, Nov. 2008.

[7] C. Y. Chen, C. Y. Hsu, and H. R. Chuang, "Design of miniature planar dual-band filter using dual-feeding structures and embedded resonators," *IEEE Microwave and wireless components letters*, vol. 16, no. 12, pp. 669-671, Dec. 2006.

[8] M. H. Weng, H. W. Wu, and Y. K. Su, "Compact and low loss dual-band bandpass filter using pseudo-interdigital stepped impedance resonators for WLANs," *IEEE Microwave and wireless components letters*, vol. 17, no. 3, pp. 187-189, Mar. 2007.

[9] M. Jiang, L. M. Chang, and A. Chin, "Design of dual-passband microstrip bandpass filters with multi-spurious suppression," *IEEE Microwave and wireless components letters*, vol. 20, no. 4, pp. 199-201, April 2010.

[10] A. Eroglu and R. Smith, "Triple band bandpass filter design and implementation using SIRs," *26th Annual Review of Progress in Applied Computational Electromagnetics* Finland, pp. 862-865, 26-29 April 2010.

[11] S. U. Rehman, A. F. A. Sheta, and M. A. S Alkanhal, "Compact bandpass filters with bandwidth control using defected ground structure (DGS)," *Appl. Comp. Electro. Society (ACES) Journal,* vol. 26, no. 7, pp. 624-630, July 2011.

[12] N. M. Garmjani and N. Komjani, "Improved microstrip folded tri-section stepped impedance resonator bandpass filter using defected ground structure," *Appl. Comp. Electro. Society (ACES) Journal,* vol. 25, no. 11, pp. 975-983, Nov. 2010.

[13] J. S. Hong and M. J. Lancaster, "Theory and experiment of novel microstrip slow-wave open-loop resonator filters," *IEEE Trans. on Microwave Theory and Techniques*, vol. 45, no. 12, pp. 2358-2365, Dec. 1997.

[14] J. S. Hong and M. J. Lancaster, *Microstrip Filters for RF/Microwave Applications*, Wiley, New York, 2001.

Mohsen Hayati received the B.Eng. in Electronics and Communication Engineering from Nagarjuna University, India, in 1985, and the M.Eng. and PhD in Electronics Engineering from Delhi University, Delhi, India, in 1987 and 1992, respectively. He joined the Electrical Engineering Department, Razi University, Kermanshah, Iran, as an Assistant Professor in 1993. He is currently an Associate Professor with the Electrical Engineering Department, Razi University. He has published more than 110 papers in international and domestic journals and conferences. His current research interests include microwave and millimeter wave devices and circuits, application of computational intelligence, artificial neural networks, fuzzy systems, neuro-fuzzy systems, electronic circuit synthesis, modeling and simulations.

Azadeh Khajavi received the B.Sc. degree in Medical Engineering from Isfahan University, Isfahan, Iran in 2004, and the M.Sc. degree in Electrical Engineering from Razi University, Kermanshah, Iran in 2011. Since 2008, she has been with the Computational Intelligence Research Center, Razi University. Her research interests include the analysis and design of high-frequency electronics and microwave passive circuits.

Hamdi Abdi received his B.Sc. degree from Tabriz University, Tabriz, Iran in 1995; M.Sc. and Ph.D. degrees from Tarbiat Modares University, Tehran, Iran, in 1999 and 2006, respectively, all in Electrical Engineering. Currently, he is an Assistant Professor in the Department of Electrical Engineering, Razi University of Kermanshah, Kermanshah, Iran. His research interests include power system operation and planning, restructuring and market design, transmission expansion planning, renewable energies, optimization and application of computational intelligence and design of electrical and control systems for industrial plants.

A New Model for the FDTD Analysis of Sub-Structures on Infinite Plates

Run Xiong[1], Bin Chen[1], Yun-Fei Mao[1, 2] and Zhao-Yang Cai[1]

[1]National Key laboratory on Electromagnetic Environment and electro-optical Engineering
PLA University of Science and Technology. Nanjing, 210007, Jiangsu, China
xiongrun1983@hotmail.com, emcchen@163.com, myf4494@126.com, resingsun@163.com

[2]China Satellite Maritime Tracking and Control Department
Yuan Wang III, Jiangyin 214400, China

Abstract ─ In this work, a new model has been proposed for the finite-difference time-domain analysis (FDTD) of sub-structure coupling problems. By stretching the total-field/scattered-field (TF/SF) boundary and the perfect electric conductor (PEC) plane into the convolution PML (CPML) layers, the coupling of sub-structures loaded on infinite planes induced by plane waves can be simulated. The validity of the proposed model has been approved from the comparison of the results obtained from the proposed model with the analytical and the open region results. The CPML performances of this model are compared in different parameters, furthermore the optimal constructive parameters of the CPML have been chosen for the high-resolution simulation of the proposed model, which can help for development of optimal sub-structure coupling.

Index Terms ─ Convolution PML (CPML), Finite-difference time-domain method (FDTD), Sub-structure, Total-field/scattered-field (TF/SF)

I. INTRODUCTION

Coupling through sub-structures (e.g., holes and seams) in conducting screens is of greater concern as the speed of the electronic designs increases [1-3]. The sub-structures may be located on conducting walls for CD-ROM's, heat vents, and input/output (I/O) cables among others. These coupling problems can be mostly simplified as one problem, which is the coupling of sub-structures located on an infinite conducting wall. Understanding the coupling mechanisms involving seams is important for estimating and reducing electro-magnetic interference.

The finite-difference time-domain (FDTD) method, which provides a simple and efficient way of solving Maxwell's equations for a variety of problems, has been widely applied in solving many types of electromagnetic coupling problems, for it has numerous time-domain and frequency-domain information.

The standard FDTD simulation with a sufficient structure resolution can be useful for analyzing the coupling mechanisms, and is frequently used as a reference to verify the subcell methods [1-5].

In [1], Wang presents a model to simulate the slot on a finite metal plate, but the truncating electric and magnetic walls wok as a waveguide and the reflection from the walls occurred. The total-field/scattered-field technique (TF/SF) [6-7] is always occupied to induce the plane wave, but it is difficult to simulate infinite scatterers illuminated by a plane wave, for the TF/SF boundary must be large enough to surround the scatterers.

In this work, a new model has been proposed for the FDTD analysis of structures on infinite planes illuminated by plane waves. The convolution perfect matched layer (CPML) [8-10] is used to truncate the computational domain. The TF/SF boundary is occupied to induce the infinite plane wave by extending the TF/SF boundary into the CPML layers. The perfect electric conductor (PEC) plate, where the sub-structure is loaded, is

Submitted On: Apr. 11, 2012
Accepted On: Dec. 24, 2012

stretched into the CPML layers to model the infinite metal plates.

In the present model, the reflection from the electric and magnetic wall of [1] can be avoided, and infinite scatterers illuminated by plane waves can be simulated without resulting in huge computational resources.

In this model, the integrality of the CPML layer is destroyed, thus the CPML performance is greatly affected, especially when the high-resolution grid is adopted. The CPML performance in this model are compared in different parameters, furthermore the optimal constructive parameters of the have been chosen for the high-resolution simulation of the proposed model, which can help for development of optimal sub-structure coupling.

II. THE MODEL FOR THE FDTD ANALYSIS OF INFINTE PLATES

To analyze the sub-structure coupling mechanism, the PEC plane where the supposed structure is located must be large enough to eliminate the edge effect. The conventional total-field/scattered-field technique (TF/SF) [6] is always occupied to induce the plane wave, but it is difficult to illuminate infinite scatterer for the total-field region must be large enough to surround the scatter.

To overcome the shortage, we stretched both the PEC plate and TF/SF boundary into the CPML layers to simulate the infinite plate illuminated by plane waves with the minimal computational usage, as shown in Fig. 1.

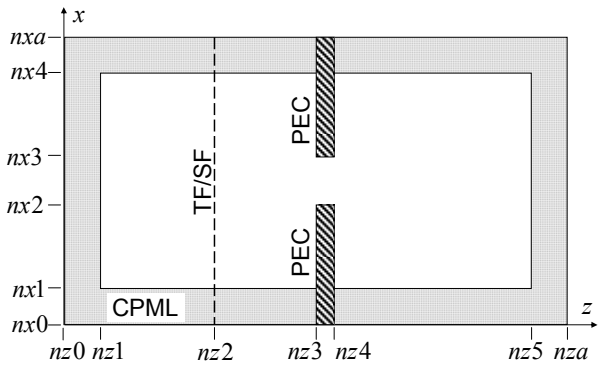

Fig. 1. The model for the FDTD analysis of sub-structures located in an infinite plate which is illuminated by a plane wave.

In this work, the CPML [8] is used to truncate the computational domain and the time-marching equation for the magnetic field component H_y in the CPML can be written as

$$H_y^{n+\frac{1}{2}}(i+\tfrac{1}{2},k+\tfrac{1}{2})=\frac{2\mu-\sigma_m\Delta t}{2\mu+\sigma_m\Delta t}H_y^{n-\frac{1}{2}}(i+\tfrac{1}{2},k+\tfrac{1}{2}) - \frac{1}{\kappa_z\Delta_z}\left[E_x^n(i+\tfrac{1}{2},k+1)-E_x^n(i+\tfrac{1}{2},k)\right], + \frac{1}{\kappa_x\Delta_x}\left[E_z^n(i+1,k+\tfrac{1}{2})-E_z^n(i,k+\tfrac{1}{2})\right] + \psi_{m_{yx}}^n(i+\tfrac{1}{2},k+\tfrac{1}{2})-\psi_{m_{yz}}^n(i+\tfrac{1}{2},k+\tfrac{1}{2}) \quad (1)$$

where μ is the permeability, σ_m is the equivalent magnetic loss, κ_x and κ_z are constitutive parameters, and the $\psi_{m_{yx}}$ and $\psi_{m_{yz}}$ are derived from

$$\psi_{m_{yx}}^n(i+\tfrac{1}{2},k+\tfrac{1}{2})=b_x\psi_{m_{yx}}^{n-1}(i+\tfrac{1}{2},k+\tfrac{1}{2}) + \frac{a_x}{\Delta_x}\left[E_z^n(i+1,k+\tfrac{1}{2})-E_z^n(i,k+\tfrac{1}{2})\right], \quad (2)$$

$$\psi_{m_{xz}}^n(i+\tfrac{1}{2},k+\tfrac{1}{2})=b_z\psi_{m_{xz}}^{n-1}(i+\tfrac{1}{2},k+\tfrac{1}{2}) + \frac{a_z}{\Delta_z}\left[E_x^n(i+\tfrac{1}{2},k+1)-E_x^n(i+\tfrac{1}{2},k)\right]. \quad (3)$$

The updating equation for the electric field E_x in the CPML can be written as

$$E_x^{n+1}(i+\tfrac{1}{2},k)=\frac{2\varepsilon-\sigma\Delta t}{2\varepsilon+\sigma\Delta t}E_x^n(i+\tfrac{1}{2},k)-\frac{1}{\kappa_z\Delta_z} \left[H_y^{n+\frac{1}{2}}(i+\tfrac{1}{2},k+\tfrac{1}{2})-H_y^{n+\frac{1}{2}}(i+\tfrac{1}{2},k-\tfrac{1}{2})\right], -\psi_{e_{xz}}^{n+\frac{1}{2}}(i+\tfrac{1}{2},k) \quad (4)$$

where ε is the permittivity, σ is the equivalent electric loss, and

$$\psi_{e_{xz}}^{n+\frac{1}{2}}(i+\tfrac{1}{2},k)=b_z\psi_{e_{xz}}^{n-\frac{1}{2}}(i+\tfrac{1}{2},k)+\frac{a_z}{\Delta_z} \left[H_y^{n+\frac{1}{2}}(i+\tfrac{1}{2},k+\tfrac{1}{2})-H_y^{n+\frac{1}{2}}(i+\tfrac{1}{2},k-\tfrac{1}{2})\right]. \quad (5)$$

The updating equation for the electric field E_z in the CPML can be written as

$$E_z^{n+1}(i,k+\tfrac{1}{2})=\frac{2\varepsilon-\sigma\Delta t}{2\varepsilon+\sigma\Delta t}E_z^{n}(i,k+\tfrac{1}{2})+\frac{1}{\kappa_x\Delta_x}\left[H_y^{n+\frac{1}{2}}(i+\tfrac{1}{2},k+\tfrac{1}{2})-H_y^{n+\frac{1}{2}}(i-\tfrac{1}{2},k+\tfrac{1}{2})\right]+\psi_{e_{zx}}^{n+\frac{1}{2}}(i,k+\tfrac{1}{2}) \quad (6)$$

where

$$\psi_{e_{zx}}^{n+\frac{1}{2}}(i,k+\tfrac{1}{2})=b_x\psi_{e_{zx}}^{n-\frac{1}{2}}(i,k+\tfrac{1}{2})+\frac{a_x}{\Delta_x}\left[H_y^{n+\frac{1}{2}}(i+\tfrac{1}{2},k+\tfrac{1}{2})-H_y^{n+\frac{1}{2}}(i-\tfrac{1}{2},k+\tfrac{1}{2})\right] \quad (7)$$

The coefficient a and b can be obtained from

$$b_i=exp\left[-(\frac{\sigma_i}{\kappa_i}+\alpha_i)\frac{\Delta t}{\varepsilon_0}\right],\quad i=x,z, \quad (8)$$

$$a_i=\frac{\sigma_i}{\sigma_K\kappa_i+\kappa_i^2\alpha_i}\left[\exp\left(-(\frac{\sigma_i}{\kappa_i}+\alpha_i)\frac{\Delta t}{\varepsilon_0}\right)-1\right],\ i=x,z. \quad (9)$$

Within the CPML layers, the constitutive parameters are scaled using polynomial scaling [12]:

$$\sigma(\rho)=\sigma_{max}(\rho/D)^m, \quad (10)$$

$$\kappa(\rho)=1+(\kappa_{max}-1)(\rho/D)^m, \quad (11)$$

$$\alpha(\rho)=\alpha_{max}(1-\rho/D)^m, \quad (12)$$

where ρ indicates the distance from the air-CPML interface into the CPML layer, D is the depth of the CPML, and m is the order of the polynomial and is chosen to be 4 in this work. The choice for σ_{max} suggest in [13] is expressed as

$$\sigma_{opt}=\frac{m+1}{150\pi\Delta_i},\quad i=x,z, \quad (13)$$

where Δ_i is the grid spacing along the x and z axis.

To simulate a seam located in an infinite plate, we extended the PEC wall into the CPML layers, shown as the hatching areas in Fig. 1, which is:

$$E_x(x,nz3:nz4)=\begin{cases}E_x(x,nz3:nz4), & x\in(nx2,nx3)\\ 0, & x\in(nx0,nx2)\cup(nx3,nxa)\end{cases} \quad (14)$$

Note that some segments of the PEC plates lie in the CPML region.

The TF/SF technique is extensively used to induce the plane wave, but TF/SF connecting surface is always a closed surface and the scatterer is fully imbedded in the total field region, as shown in [6, Fig. 2]. Therefore, to simulate the plane wave illuminating the infinite PEC plate, one has to use a very large total-field domain to embed the plate, which will result in huge memory usage, especially when high-resolution simulation is involved.

In this work, the TF/SF boundary is stretched into the CPML layer to induce a plane wave illuminating an infinite PEC plate, shown as the dashed line in Fig. 1. Therefore, the connecting surface has only one face and the FDTD updating equations at the boundary can be written as:

$$H_y^{n+\frac{1}{2}}(x,nz2-\tfrac{1}{2})=H_y^{n+\frac{1}{2}}(x,nz2-\tfrac{1}{2})_{FDTD}+\frac{\Delta t}{\mu\Delta_z}E_{x,i}^{n}(nz2),\ \ x\in(nx0,nxa) \quad (15)$$

$$E_x^{n+1}(x,nz2)=E_x^{n+1}(x,nz2)_{FDTD}+\frac{\Delta t}{\varepsilon\Delta_z}H_{y,i}^{n+\frac{1}{2}}(nz2-\tfrac{1}{2}),\ \ x\in(nx0,nxa) \quad (16)$$

It is worth to note that the TF/SF boundary dimension in the x direction of both the E_x and H_y are from *nx0* to *nxa*, which is from the down CPML edge to the up CPML edge.

When the incidence of oblique propagation directions is involved, the generalized TF/SF (G-TF/SF) [11] technique is used.

$$\psi_{inc}^{num}=X_0^{num}A_{PML}(\theta_{inc},\xi_x,\xi_y). \quad (17)$$

Here, ψ_{inc}^{num} represents the required incident $E_{x,i}^{n}$ or $H_{y,i}^{n+\frac{1}{2}}$ field component in (15) and (16) in the CPML region. X_0^{num} is the corresponding free space incident field. $A_{PML}(\theta_{inc},\xi_x,\xi_y)$ is the appropriate multiplying factor at the observation point in the CPML region, where: θ_{inc} is the incident angle of the plane wave; $\xi_x=d_x\zeta_{x,PML}$; $\xi_z=d_z\zeta_{z,PML}$; $\zeta_{x,PML}$ and $\zeta_{z,PML}$ are the electric or magnetic loss constants at the observation point in the CPML region in the x and z directions, respectively; and d_x and d_z are the depths of the observation point inside the CPML region in the x and z directions, respectively. $A_{PML}(\theta_{inc},\xi_x,\xi_y)$ can be derived from [11] for the up and down CPML areas respectively.

The segments of the TF/SF boundary and the PEC plates that lie in free space are treated exactly like the conventional TF/SF [6] boundary and PEC plates. While in the CPML regions, special treatment are needed. The flowchart of the field update in the CPML regions is shown in Fig. 2. For other regions, the conventional time-marching equations can be useful.

There is a key advantage to this methodology, that the area at the right side of the TF/SF boundary is the entire total field region. Therefore, only a limited computational domain can model the infinite scatterer illuminated by an infinite plane wave.

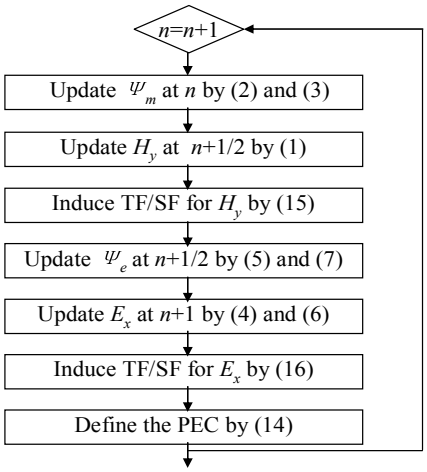

Fig. 2. Flowchart of field in the CPML region.

III. NUMERICAL VALIDATION OF THE PROPOSED ODEL

A. Validation of the proposed TF/SF boundary

In this section, numerical examples are implemented to validate the TF/SF boundary of the proposed model. The computational domain is shown in Fig. 3, where the PEC plane is removed. The TF/SF boundary is set to be 12 cells away from the left air-CPML interface, and 28 cells from the right air-CPML interface. The computational domain is 25 cells from the up air-CPML interface to the down interface. The computational domain is truncated along the *x*- and *z*-directions by 10 additional CPML layers, which results in a 45×60 cells lattice. The electric field component E_x is monitored at the center of the reference plane, which is 16 cells away from the TF/SF boundary.

The sinusoidal modulated Gaussian pulse is excited as the normal incident pulse

$$E_x(t)=\exp\left[-4\pi\left(\frac{t-T_c}{T_d}\right)^2\right]\sin\left[2\pi f_c\left(t-T_c\right)\right], \quad (18)$$

where f_c=1 GHz, $T_d=2/f_c$, $T_c=0.6T_d$.

The source is induced through the proposed TF/SF boundary (15) and (16), where *nz*2=22. Square cells are used, with the grid size Δ=1 cm, and the time step is $\Delta t=\Delta/2c$, where *c* is the speed of light in the free space.

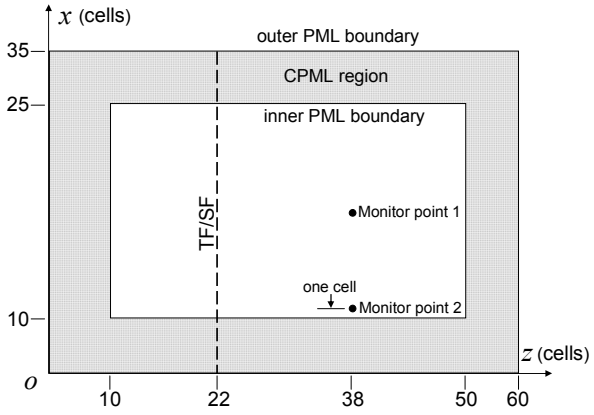

Fig. 3. Computational domain.

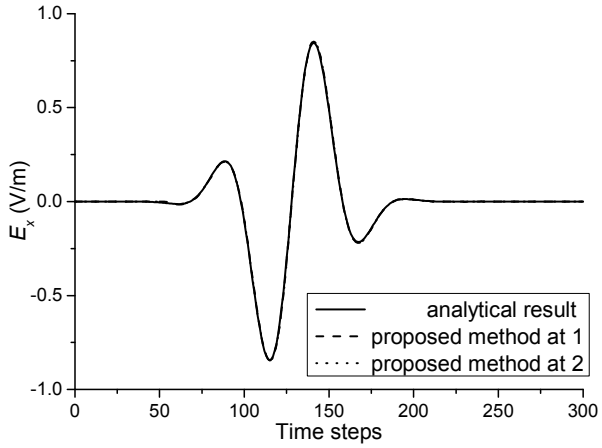

Fig. 4. Comparison of the electric field component got from the proposed method with analytical result.

To verify the validity of the proposed TF/SF boundary, which is stretched into the CPML layers, the electric field component at the two monitor points is compared with the analytical result. The reference Point 1 is at the center of the plane 16 cells from the TF/SF boundary, and the Point 2 is one cell from the down air-CPML interface.

Figure 4 plots the waveforms calculated at the two points, where the analytical result is also presented as a benchmark. It is clear that the fields predicted by the proposed method are in good agreement with the analytical result. Comparison

of the fields at other positions indicates the same conclusion.

B. Validation of the proposed PEC boundary

In this section, numerical examples are implemented to validate the proposed PEC boundary, which is stretched into the CPML layers. The computational domain is the same as Fig. 3, where the PEC plate is set to be 12 cells from TF/SF boundary and 15 cells from the right CPML interface, and the PEC plate is 1 cell thick. The slot, which is 1 cell wide, is located at the center of the PEC plate. Other conditions are the same as the above section.

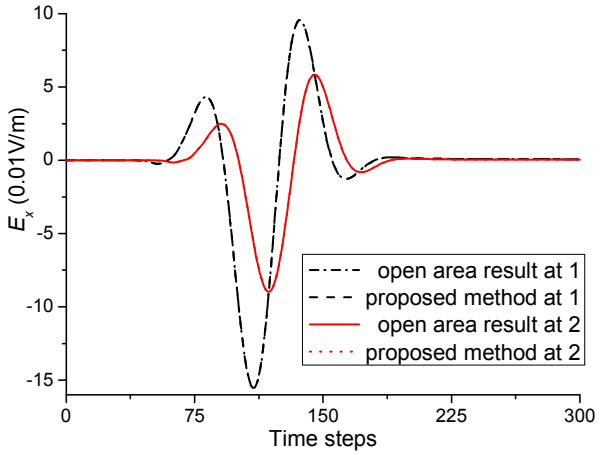

Fig. 5. Waveforms of the electric field component E_x as computed from the proposed model and the open area results.

To provide a benchmark for comparison, an open area result is needed. To this end, the same mesh is extended by 150 cells in the x and z dimensions, leading to a 340×350 cells lattice. We compared the electric field component as computed from the proposed model and that from the reference solution, showing a very good mutual agreement at both the two measure points, as shown in Fig. 5.

IV. CPML PARAMETERS FOR THE HIGH-RESOLUTION SIMULATION

When the FDTD method is adopted to analyze the sub-structure coupling, the grid dimension is always chosen to be small compared with the supposed structure size (e.g., w/15 or d/15, where w and d are the slot width and depth respectively), in order to satisfy the precision demand on the slot resolution [2]. It can be seen from Figs. 4-5 that the CPML performance is excellent with the ordinary resolution, but the CPML performance with high-resolution has not been analyzed. In the present model, the integrality of the CPML layer is destroyed, thus the CPML performance is greatly affected, especially when the high-resolution grid is adopted.

To check the CPML performance of the proposed model, the computational domain shown in Fig. 6 is adopted, where the configuration is also shown. The source of (18) is chosen to be the incident pulse, and square FDTD cells are adopted with the size Δ=0.3 mm. The depth of the slot plate is 20 cells. The slot, which is located at the centre of plate, is 15 cells wide. 10-cell-thick CPML layers terminate the grid, which results in a 55×166 cells lattice.

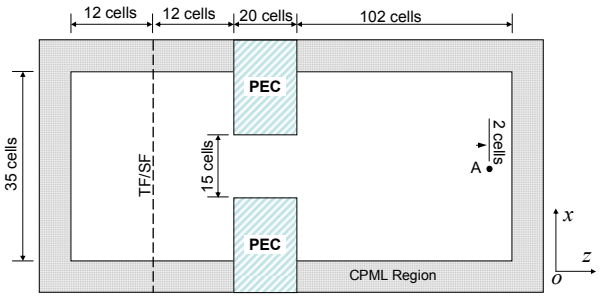

Fig. 6. Computational domain of the 2-D structures, where the observation point is 2 cells from the CPML boundary.

To study the reflection error due to the CPML in this model, a reference problem is also simulated. The same mesh is extended by 4500 cells in the x and z dimensions, leading to a 9055×9166 cells lattice. The fields within the lattice are then excited by an identical source, and the time-dependent fields are recorded within the region representing the original lattice. The error relative to the reference solution (in decibels) is computed as a function of time using:

$$R_{dB} = 20\log_{10}\frac{\left|E_x^R(t) - E_x^T(t)\right|}{max\left|E_x^R(t)\right|}, \qquad (19)$$

where $E_x^T(t)$ represents the field computed in the test domain and $E_x^R(t)$ is the reference field computed using the larger domain.

There are literatures about the parameters of

the CPML [8], [12]. In [8], κ_{max}=5, $\sigma_{max}/\sigma_{opt}$=1.3, and α varies in the CPML layers with α_{max}=0.05. In [12], κ_{max}=25, $\sigma_{max}/\sigma_{opt}$=1.6, while α=0.003 and is held constant through the CPML layers. The reflective error of the CPML with the two parameters at the measurement Point *A*, which is 2 cells (0.6 mm) away from the CPML interface computed via (19) is recorded, as shown in Fig. 7. It is shown that the reflection error can reach as large as -50 dB for this case when the CPML is adopted with the parameters of [8] and [12].

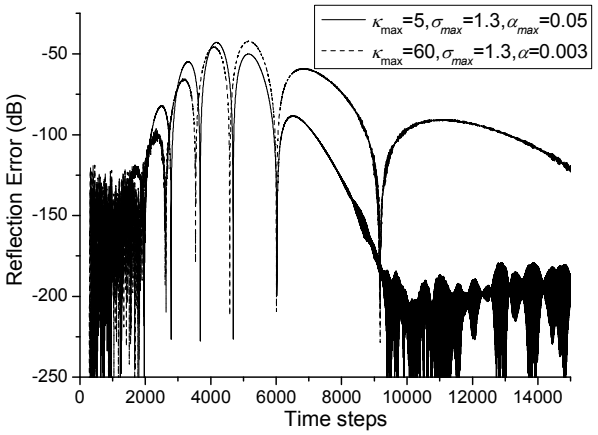

Fig. 7. Error in the electric field intensity relative to the field's maximum amplitude versus time for the CPML of the parameters of [8] and [12].

To get a better CPML performance, the α_i is chose to decrease to zero away from the boundary interface as (12), and the relative reflection error is calculated via (19) with varied CPML constitutive parameters. Figure 8 plots contours of the maximum relative error in dB as a function of κ_{max} and $\sigma_{max}/\sigma_{opt}$ at Point A, with α_{max}=1.25. It can be seen that the maximum relative reflection error as low as -115 dB is achieved by selecting κ_{max}=40, $\sigma_{max}/\sigma_{opt}$=0.9 and α_{max}=1.25.

V. VALIDATION THE POPOSED MODEL IN 3-D PROBLEMS

To verify the proposed model with the supposed constitutive parameters, the three-dimensional slot-coupling problem is included, and the computational domain is shown in Fig. 9. The depth of the slot plane is 2 mm, and the conducting wall is introduced by the supposed PEC boundary. The size of the slot, which is located at the center of the conducting wall, is $L\times w$=150×1 mm. The slot plane is illuminated by a normal incidence, and the pulse in [14] is excited through the supposed TF/SF boundary

$$E_x^{inc}(t)=\frac{1}{0.8258}\frac{1}{e^{[-20(t-t_0)/\beta]}+e^{[(t-t_0)/\beta]}}, \qquad (20)$$

where t_0=6.67×10^9, and β=6.67×10^9.

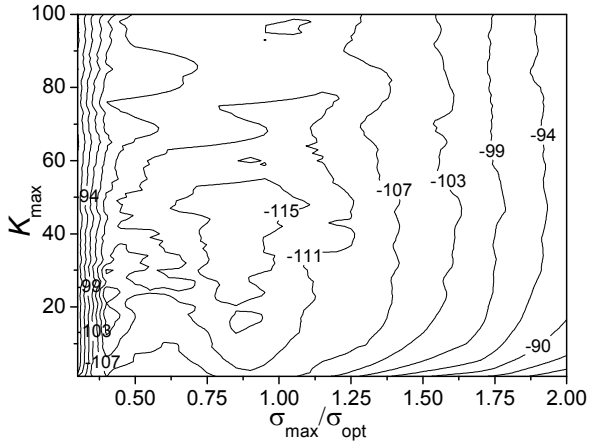

Fig. 8. Maximum relative error at Point A as a function of κ_{max} and $\sigma_{max}/\sigma_{opt}$ (with D=10 cells, α_{max}=1.25 and m=4)

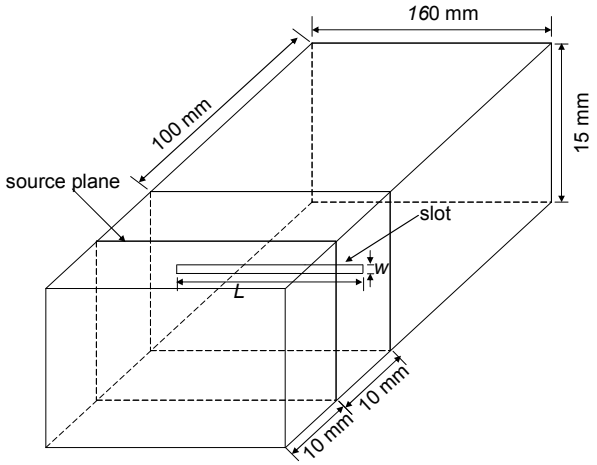

Fig. 9. Computational domain of the three-dimensional slot coupling.

Cubic FDTD cell is used, and the spatial step is 1/11 mm, while the time step is 0.06 ps. The computational domain is truncated by a 10-cell layer CPML, and the problem is simulated with the CPML parameters of [8], [12] and this study. The penetrating electric field component is monitored at the center of the reference plane, which is 90 mm away from the slot plane at the

shadow side.

Figure 10 shows the waveforms of the electric field at the observation point. It can be seen that obvious reflections from the CPML occurred for the constitutive parameters given by [8] and [12], while the CPML performs well with the constitutive parameters in this work.

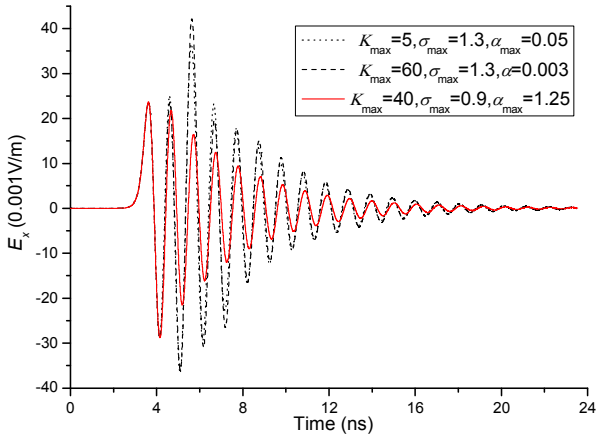

Fig. 10. Waveforms of the penetrating electric field component E_x^p calculated by the proposed model with the constitutive parameters of [8], [12], and this study.

VI. CONCLUSIONS

In this work, a new model has been proposed for the high-resolution FDTD analysis of sub-structures on the infinite plates induced by plane waves. The CPML is used to truncate the computational domain. The PEC plate, where the sub-structure is loaded, is stretched into the CPML to model the infinite plane. The TF/SF boundary is occupied to induce the plane wave illuminating the infinite PEC by extending the TF/SF boundary into the CPML layers.

It has been approved that the set of the TF/SF boundary and the PEC boundary in the proposed model are numerically efficient. The CPML performances are compared in different parameters, furthermore the optimal constructive parameters of the CPML have been chosen for the high-resolution simulation of the proposed model, which can help for development of optimal sub-structure coupling. Three-dimensional slot coupling results are also used to verify the efficiency of the proposed model with the supposed parameters.

The present model can be used for the high-resolution FDTD analysis of the sub-structure coupling located on infinite conducting walls illuminated by plane waves.

REFERENCES

1. B.-Z. Wang, “Enhanced Thin-Slot Formalism for the FDTD Analysis of Thin-Slot Penetration,” *IEEE Microw. Guided Wave Lett.*, vol. 5, pp. 142-143, May 1995.
2. M. A. Gkatzianas, C. A. Balanis and R. E. Diaz, “The Gilbert–Holland FDTD Thin Slot Model Revisited: an Alternative Expression for the In-Cell Capacitance,” *IEEE Microw. Wireless Compon. Lett.*, vol. 14, pp. 219-221, May 2004.
3. D. W. Sun, J. H. Yu, “Extending the 2-D Contour Path Method to the 3-D,” *Applied Computational Electromagnetics Society (ACES) Journal*, vol. 10, pp. 655-657, 2011.
4. R. Xiong, B. Chen, Q. Yin and Z.-Y. Cai, “Improved Formalism for the FDTD Analysis of Thin-Slot Penetration by Equivalence Principle,” *IEEE Antennas and Wireless Propag. Lett.*, vol. 10, pp. 655-657, 2011.
5. C. M. Ruiz, J. J. Simpson, “Ultra High-Resolution FDTD Modeling of a High-Performance VLSI Package for Identifying Resonances and Coupling,” *Applied Computational Electromagnetics Society (ACES) Journal*, vol. 26, no. 4, pp. 284-294, April 2011.
6. K. Umashankar, A. Taflove, "A Novel Method to Analyze Electromagnetic Scattering of Complex Objects," *IEEE Trans. Electromag. Compat.*, vol. EMC-24, no. 4, pp. 397-405, Nov. 1982.
7. H. A. Abdallah, “An Optimized High-Order Implicit FDTD Solver with One-Sided TF/SF for Simulation of Photonic Devices,” *Applied Computational Electromagnetics Society (ACES) Journal*, vol. 20, no. 1, pp. 78-85, March 2005.
8. J. A. Roden, and S. D. Gedney, “Convolution PML (CPML): an Efficient FDTD Implementation of the CFS-PML for Arbitrary Media”, *Microwave and Opt. Technol. Lett.*, vol. 27, no. 5, pp. 334-339, Dec. 2000.
9. N. Okada, J. B. Cole, “Nonstandard Finite Difference Time Domain Algorithm for Berenger’s Perfectly Matched Layer,” *Applied Computational Electromagnetics Society (ACES) Journal*, vol. 26, no. 2, pp. 153-159, February 2011.
10. M. Wong, A. R. Sebak, “The Floating PML Applied to Practical FDTD Applications,” *Applied Computational Electromagnetics Society (ACES) Journal*, vol. 23, no. 2, pp. 110-119, June 2008.
11. V. Anantha and A. Taflove, "Efficient Modeling of Infinite Scatterers using a Generalized Total-Field/Scattered-Field FDTD Boundary Partially Embedded within PML," *IEEE Trans.*

Antennas. Propagat., vol. 39, no. 2, pp. 147-155, May 2002.

12. Z.-Y. Cai, B. Chen, K. Liu, Y.-T. Duan, and Y.-F. Mao, "The CFS-PML for Periodic Laguerre-Based FDTD Method," *IEEE Microw. Wireless Compon. Lett.*, vol. 22, no. 4, pp. 487-489, 2012.
13. A. Taflave and S. C. Hagness, *Computational Electrodynamics: The Finite-Difference Time-Domain Method*, 2nd ed, Boston, Artech House, 175-134, 2000.
14. K.-P. Ma, M. Li, J. L. Drewniak, T. H. Hubing and T. P. V. Doren, "Comparison of FDTD Algorithms for Subcellular Modeling of Slots in Shielding Enclosures," *IEEE Trans. Electro*mag. Compat., vol. 39, no. 2, pp. 147-155, May 1997.

Run Xiong was born in Sichuan province, China, in 1983. He received the B.S. and M.S. degrees in electric systems and automation from Engineering Institute of Corps of Engineers, PLA University of Science and Technology, Nanjing, China, in 2005 and 2010 respectively, where he is currently working toward the Ph.D. degree. He is now with the National Key laboratory on Electromagnetic Environment and electro-optical Engineering, and his research interests include computational electromagnetics and EMC.

Bin Chen was born in Jiangsu, China, in 1957. He received the B.S. and M.S. degrees in electrical engineering from Beijing Institute of Technology, Beijing, China, in 1982 and 1987, respectively, and the Ph.D. degree in electrical engineering from Nanjing University of Science and Technology, Nanjing, China, in 1997. Currently, he is a Professor at National Key laboratory on Electromagnetic Environment and electro-optical Engineering, PLA University of Science and Technology. His research includes computational electromagnetics, EMC and EMP.

Yunfei Mao was born in Zhejiang province, China, in 1984. He received the B.S. degrees in electric systems from Engineering Institute of Corps of Engineers, PLA University of Science and Technology, Nanjing, China, in 2006 and 2009 respectively, where he is currently working toward the Ph.D. degree. He is now with the National Key laboratory on Electromagnetic Environment and electro-optical Engineering. His research interests include computational electromagnetics.

Zhaoyang Cai was born in Henan province, China, in 1985. He received the B.S. degrees in electric systems from Engineering Institute of Corps of Engineers, PLA University of Science and Technology, Nanjing, China, in 2007 and 2011 respectively, where he is currently working toward the Ph.D. degree. He is now with the National Key laboratory on Electromagnetic Environment and electro-optical Engineering. His research interests include computational electromagnetics.

Combination of Asymptotic Phase Basis Functions and Matrix Interpolation Method for Fast Analysis of Monostatic RCS

Yuejin Zhang [1], Dechang Huang [1], Jiaqi Chen [2]

[1] School of Information Engineering
East China Jiaotong University, Nanchang, 330013, China
zyjecjtu@foxmail.com, huangdechang2006@126.com

[2] College of Computer and Information
Hohai University, Nanjing, 210098, China
cjq19840130@163.com

Abstract ─ The combination of asymptotic phase basis functions and matrix impedance method is proposed and used for fast computation of monostatic scattering from electrically large object. Since asymptotic phase (AP) basis function can be defined on large patches, less number of unknowns is required than that when using traditional Rao-Wilton-Glisson (RWG) vector basis function. In order to efficiently compute electromagnetic scattering, the flexible general minimal residual (FGMRES) iterative solver is applied to compute the coefficients of the basis functions and the sparse approximate inversion (SAI) preconditioning technique is used to accelerate the iterative solver. However, the impedance matrix varies with incident angles, resulting in significant computation time cost for construction of impedance and SAI preconditioning matrices. This difficulty can be alleviated by using the model-based parameter estimation (MBPE) technique. Both the impedance and SAI preconditioning matrices are interpolated at intermediate angles over a relatively large angular band with rational function interpolation method. Numerical results demonstrate that this method is efficient for monostatic RCS calculation with high accuracy.

Index terms ─ Interpolation, linear phase basis function, preconditioning technique, monostatic RCS, electromagnetic scattering

I. INTRODUCTION

Electromagnetic wave scattering problems address the physical issue of detecting the diffraction pattern of the electromagnetic radiation scattered from a large and complex body when illuminated by an incident incoming wave. A good understanding of these phenomena is crucial to radar cross section (RCS) calculation, antenna design, electromagnetic compatibility, and so on. All these simulations are very demanding in terms of computer resources, and require efficient numerical methods to compute an approximate solution of Maxwell's equations. Using the equivalence principle, Maxwell's equations can be recast in the form of integral equations that relate the electric and magnetic fields to the equivalent electric and magnetic currents on the surface of the object. Amongst integral formulations, the surface integral equation (SIE) is widely used for electromagnetic wave scattering problems as it can handle the most general geometries. The matrix associated with the resulting linear systems is large, dense, complex and non-Hermitian [1]. It is basically impractical to solve SIE matrix equations using direct methods because they have a memory requirement of $O(N^2)$, where N refers to the number of unknowns. This difficulty can be circumvented by use of iterative methods, and the required matrix-vector product operation can be efficiently evaluated by multilevel fast multipole algorithm (MLFMA) [2, 3]. The use of MLFMA reduces the memory requirement to $O(N\log N)$ and the computational complexity of per-iteration to $O(N\log N)$.

Generally, the scattering of arbitrary metallic object can be accurately computed by Rao-Wilton-Glisson (RWG) basis function and MoM-MLFMA. Using traditional RWG basis functions, the required number of unknowns is on the order of 100 per square wavelength making electrically large problems impractical [20]. For large smooth objects, the rapid spatial

Submitted On: Apr. 27, 2012
Accepted On: Dec. 25, 2012

variation in the current is due to phase variations rather than magnitude variations. By using the asymptotic phase (AP) basis functions [5-8], drastically computation time can be reduced for large and smooth bodies. However, the AP based impedance matrix varies with incident angles, resulting in significant computation time cost for impedance matrix construction for monostatic calculations. This can be computationally prohibitive despite the increased power of the present generation of computers.

Since the LP-RWG based impedance matrix is not constant for monostatic RCS computation, traditional current interpolation techniques [15-19] are not suitable for fast angular sweep. To efficiently obtain the monostatic RCS using AP-RWG basis function, the impedance matrix interpolation method can be applied to avoid the construction of impedance matrices repeatedly [11-13]. MBPE is the abbreviation of model-based parameter estimation and the rational function approximation is used in MBPE. Using integral equation and moment method to compute the scattering, the elements of impedance matrix are calculated by integral of Green's function. Since the Green's function takes the form of exponential function which is easily to be approximated by rational function, the MBPE could be able to perform good results in impedance matrix interpolation.

Interpolating impedance matrix is able to save much time for constructing impedance matrix but can do nothing for iterative solution repeatedly. Using SAI preconditioning method [9,10] can accelerate iterative solution but increases large time for constructing SAI matrices. Thus, new method is required to circumvent this difficulty. Due to SAI matrix is an approximate inverse of impedance matrix, it is still a continuous function of angle. Moreover, inaccurate preconditioning matrix can not impact the precise of linear system. Consequently, using interpolation technique is a good way to accelerate the construction of SAI matrices. In this paper, the combination of the impedance matrix interpolation and the preconditioning matrix interpolation is proposed to efficient computation of monostatic RCS over broad angular band.

The remainder of this paper is organized as follows. Section II demonstrates the theory and formulation of asymptotic phase basis function. Impedance and SAI preconditioning matrix interpolation technique is discussed in section III. Numerical experiments of several geometries are presented to demonstrate the efficiency of this proposed method in Section IV. Conclusions are provided in Section V.

II. FORMULATIONS OF INTEGRAL EQUATIONS WITH ASYMPTOTIC PHASE BASIS

For electromagnetic scattering from perfect electrical conductor (PEC), the SIE includes electric field integral equation (EFIE) and magnetic field integral equation (MFIE). In order for avoiding resonance problem, the combination form of EFIE and MFIE which names combined field integral equations (CFIE) is widely used for closed structure [4]. The CFIE formulation of electromagnetic wave scattering problems using planar Rao-Wilton-Glisson (RWG) basis functions for surface modeling is presented in [20]. The resulting linear systems from CFIE formulation after Galerkin's testing are briefly outlined as follows:

$$\sum_{n=1}^{N} Z_{mn} a_n = V_m, \qquad \mathrm{m} = 1, 2, ..., N \tag{1}$$

where Z_{mn} is the element of the impedance matrix. V_m is the element of the right hand side.

$$Z_{mn}^{EFIE} = jk\eta \int_{S_m} \mathbf{\Lambda}_m \int_{S_n} \left(\bar{\bar{\mathbf{I}}} + \frac{\nabla\nabla}{k^2} \right) G(\mathbf{r}, \mathbf{r}') \mathbf{\Lambda}_n d\mathbf{r}' d\mathbf{r}$$

$$Z_{mn}^{MFIE} = \frac{1}{2} \int_{S_m} \mathbf{\Lambda}_m \mathbf{\Lambda}_n d\mathbf{r} - \int_{S_m} \mathbf{\Lambda}_m \cdot \hat{\mathbf{n}} \times \nabla \times \int_{S_n} G(\mathbf{r}, \mathbf{r}') \mathbf{\Lambda}_n d\mathbf{r}' d\mathbf{r}$$

$$V_m = \int_{S_m} \mathbf{\Lambda}_m \cdot \left[\alpha \frac{\mathbf{E}^{inc}}{\eta} + (1-\alpha) \hat{\mathbf{n}} \times \mathbf{H}^{inc} \right] d\mathbf{r}$$

Here G($\mathbf{r}$, $\mathbf{r}'$) refers to the Green's function in free space and $\{a_n\}$ is the column vector containing the unknown coefficients of the surface current expansion with RWG basis functions. Also, as usual, $\mathbf{r}$ and $\mathbf{r}'$ denote the observation and source point locations. $\mathbf{E}^{inc}$(r) and $\mathbf{H}^{inc}$(r) is the incident excitation plane wave, and η and k denote the free space impendence and wave number, respectively. Once the matrix equation (1) is solved by numerical matrix equation solvers, the expansion coefficients $\{a_n\}$ can be used to calculate the scattered field and RCS. In the following, we use $\mathbf{A}$ to denote the coefficient matrix in equation (1), $\mathbf{x} = \{a_n\}$, and $\mathbf{b} = \{V_m\}$ for simplicity. Then, the CFIE matrix equation (1) can be symbolically rewritten as:

$$\mathbf{Ax} = \mathbf{b} \tag{2}$$

Following the conventional MoM formulation, the induced current $\mathbf{J}$ is expanded in terms of subsectional basis functions $\mathbf{f}_n$. On the smooth regions of S, where the induced surface currents

present an asymptotic behaviour, the current density is expanded in terms of the so-called linearly phased Rao–Wilton–Glisson (LP-RWG) vector basis functions proposed in [5-8], whose formulation is included here for the sake of completeness:

$$\mathbf{f}_n(\mathbf{r}) = \begin{cases} \mathbf{\Lambda}_n^+ e^{-j\mathbf{k}_n^+\cdot\left(\boldsymbol{\rho}_n^+ - \boldsymbol{\rho}_{nc}^+\right)} & \mathbf{r}\in T_n^+ \\ \mathbf{\Lambda}_n^- e^{-j\mathbf{k}_n^-\cdot\left(\boldsymbol{\rho}_n^- - \boldsymbol{\rho}_{nc}^-\right)} & \mathbf{r}\in T_n^- \\ 0 & otherwise \end{cases} \tag{3}$$

where $\mathbf{\Lambda}_n^{\pm} = \pm\frac{l_n}{2A_n^{\pm}}\boldsymbol{\rho}_n^{\pm}$ and $\mathbf{\Lambda}$ is the RWG basis function. l_n is the length of the common edge to the triangles $T_n^{\pm}$ conforming the basis function, $A_n^{\pm}$ is the area of each triangle, $\boldsymbol{\rho}_n^{\pm}$ is the corresponding vector from the free vertex of $T_n^{\pm}$ to a point $\mathbf{r}$ on the triangle, and $\boldsymbol{\rho}_{nc}^{\pm}$ is the vector from the free vertex of triangle $T_n^{\pm}$ to the midpoint of the common edge $\mathbf{r}_{nc}$. Finally, $\mathbf{k}_n$ is the vector wavenumber associated to the phase of the current density on the function. Compared with traditional RWG basis functions, drastic reduction of the required number of unknowns can be achieved by using the linearly-phased RWG basis functions.

To solve the equation (2) by an iterative method, the matrix-vector products are needed at each iteration step. Physically, a matrix-vector product corresponds to one cycle of iterations between the basis functions. The basic idea of the fast multipole method (FMM) is to convert the interaction of element-to-element to the interaction of group-to-group. Here a group includes the elements residing in a spatial box. The mathematical foundation of the FMM is the addition theorem for the scalar Green's function in free space. Using the FMM, the matrix-vector product $\mathbf{Ax}$ can be written as:

$$\mathbf{Ax} = \mathbf{A}_N\mathbf{x} + \mathbf{A}_F\mathbf{x} \tag{4}$$

Here $\mathbf{A}_N$ is the near part of $\mathbf{A}$ and $\mathbf{A}_F$ is the far part of $\mathbf{A}$.

In the FMM, the calculation of matrix elements in $\mathbf{A}_N$ remains the same as in the MoM procedure. However, those elements in $\mathbf{A}_F$ are not explicitly computed and stored. Hence they are not numerically available in the FMM. It has been shown that the operation complexity of FMM to perform $\mathbf{Ax}$ is $O(N^{1.5})$. If the FMM is implemented in multilevel, the total cost can be reduced further to $O(NlogN)$ [2,3].

III. IMPEDANCE AND PRECONDITIONING MATRIX INTERPOLATION METHOD

The methodology on how to efficient calculation of monostatic scattering with asymptotic phase basis function is discussed in this section. When asymptotic phase basis is applied for construction of the impedance matrix, each element of the matrix is not constant over the interested angular band. Repeated impedance matrix construction cost plenty of time. Accordingly, interpolation method is used to accelerate monostatic scattering calculation. First of all, the impedance matrix interpolation method is introduced. Then SAI preconditioning matrix interpolation method is proposed. Finally, a hybrid method combines both of the two interpolation methods is discussed, which make a good way to the efficient analysis of wide-band scattering.

Using method of moment, the current density at certain angle can be obtained by solving equation (2). For a wide angular band, we have to repeat this procedure at a set of discrete frequencies to get the monostatic response. For structures with a large electrically scale, the required solution is highly computationally expensive. In order to reduce the matrix filling time of equation (2), the MBPE interpolation is employed to obtain the impedance matrix over a wide band.

$$Z^{ij}(f) = \frac{c_0 + c_1 f + \cdots + c_p f^p}{1 + d_1 f + \cdots + d_q f^q} \tag{5}$$

where Z^{ij} denotes the element of the impedance matrix $\mathbf{Z}$, the superscripts i and j are the serial number of row and column, respectively. c_0, …, c_p and d_1, …, d_q are coefficients determined by the solution of following linear equations:

$$\begin{bmatrix} 1 & \cdots & f_1^p & -Z_1^{ij}f_1 & \cdots & -Z_1^{ij}f_1^q \\ \vdots & & \vdots & \vdots & & \vdots \\ 1 & \cdots & f_{p+1}^p & -Z_{p+1}^{ij}f_{p+1} & \cdots & -Z_{p+1}^{ij}f_{p+1}^q \\ 1 & \cdots & f_{p+2}^p & -Z_{p+2}^{ij}f_{p+2} & \cdots & -Z_{p+2}^{ij}f_{p+2}^q \\ \vdots & & \vdots & \vdots & & \vdots \\ 1 & \cdots & f_{p+q+1}^p & -Z_{p+q+1}^{ij}f_{p+q+1} & \cdots & -Z_{p+q+1}^{ij}f_{p+q+1}^q \end{bmatrix} \cdot \begin{bmatrix} c_0 \\ \vdots \\ c_p \\ d_1 \\ \vdots \\ d_q \end{bmatrix} = \begin{bmatrix} Z_1^{ij} \\ \vdots \\ Z_{p+1}^{ij} \\ Z_{p+2}^{ij} \\ \vdots \\ Z_{p+q+1}^{ij} \end{bmatrix} \tag{6}$$

Equation (6) can be solved by a direct matrix inversion, since the order of the matrix $p + q + 1$ is low in this case. To accelerate the solution of (2), the octree structure based fast multiple method [2,3] is applied to MoM. Then equation (2) can be rewritten as

$$(\mathbf{Z}_{\text{near}} + \mathbf{Z}_{\text{far}})\cdot\mathbf{I} = \mathbf{V} \tag{7}$$

where $\mathbf{Z}_{\text{near}}$ is the near field impedance matrix evaluated by the MoM and $\mathbf{Z}_{\text{far}}$ is the far field part evaluated by the MLFMA. The set of $\mathbf{Z}_{\text{near}}$

are interpolated by the MBPE while $\mathbf{Z}_{far}$ are evaluated by the MLFMA method efficiently.

Although the impedance matrix interpolation method can avoid filling impedance matrix repeatedly, iterative solution of matrix equations is still required at each angular point. Thus, computational efficiency is challenged by ill-conditioned linear equations. Preconditioning technique, such as SAI, can greatly improve condition number of the system so as to accelerate the convergence of the iterative solver. The formulation of preconditioning technique can be described by

$$\mathbf{M}\cdot\mathbf{ZI} = \mathbf{M}\cdot\mathbf{V} \tag{8}$$

where $\mathbf{M}$ is the SAI preconditioning matrix in this paper, the purpose of preconditioning is to make the preconditioned matrix $\mathbf{MZ}$ better conditioned than matrix $\mathbf{Z}$. Generally, $\mathbf{Z}_{near}$ is used as the basis for constructing preconditioner. Thus, it suffices to solve a single problem for each minimum group at the lowest level as in [9, 10]. Since the operation on all edges of the same group is done at a time, it can reduce the construction of SAI significantly. However, it is still time-consuming to construct SAI preconditioning matrix repeatedly at each frequency point. According to the theory of SAI, it is apparent that preconditioning matrix is a sparse matrix for computation and storage, which makes the utilization of interpolation method possible. Therefore, matrix interpolation by the MBPE can be transplanted to interpolate SAI preconditioning matrix.

$$M^{ij}(f) = \frac{c_0 + c_1 f + \cdots + c_p f^p}{1 + d_1 f + \cdots + d_q f^q} \tag{9}$$

Also the unknown coefficients of the numerator and denominator are uniquely determined by matching the $p + q + 1$ sampling M^{ij} as equation (6).

IV. NUMERICAL RESULTS

In this section, a number of numerical results are presented to demonstrate the accuracy and efficiency of the preconditioning matrix interpolation method for fast calculation of RCS over wide band. The flexible general minimal residual (FGMRES) [21,22] algorithm is applied to solve linear systems. The dimension size of Krylov subspace is set to be 30 for outer iteration and the dimension is set to be 10 for inner iteration. The tolerance of inner iteration is 0.1 in this paper. All experiments are conducted on an Intel Core(TM) II Duo with 3.45 GB local memory and run at 2.40 GHz in single precision. The iteration process is terminated when the 2-norm residual error is reduced by 10^{-3}, and the limit of the maximum number of iterations is set as 1000.

As well known, the impedance matrix with traditional RWG basis is constant for monostatic scattering computation. Using traditional RWG basis functions, the required number of unknowns is on the order of 100 per square wavelength making electrically large problems impractical. In order to alleviate this difficulty, the asymptotic phase RWG basis is used for construction impedance matrix. However, the impedance matrix is not constant over the angular band. Fortunately, the element of impedance matrix is a trigonometric function of the incident angle and can be interpolated by MBPE successfully. Three geometries are applied to illustrate the performance of our method. They consist of a metallic cylinder (10λ ×4λ) with 5279 unknowns, a PEC Cube (15λ× 15λ×15λ) with 7137 unknowns, and a metallic plane with 10968 unknowns. The incident wave is the plane wave with vertical polarization. That is, if the incident angle is θ and φ, the vector of incident direction is (-sinφ, cosφ). The frequency of incident wave is 300 MHz for both cylinder and cube. The frequency is 600MHz for PEC plane.

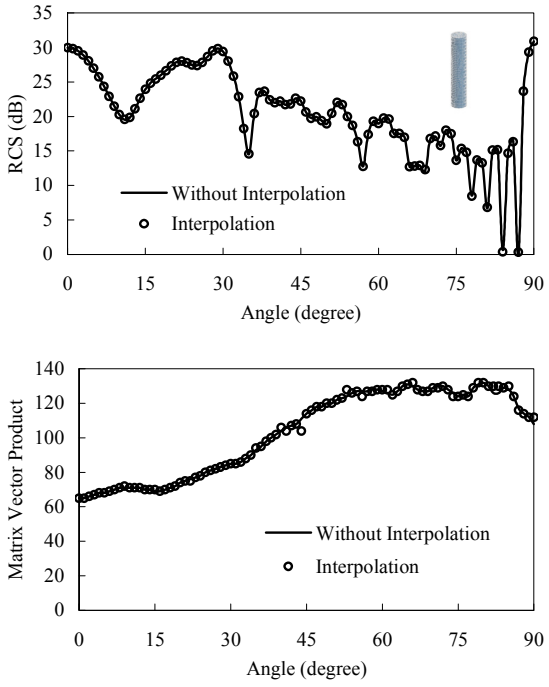

Fig. 1. Cylinder: (a) RCS for VV-polarization, 300 MHz; (b) Number of matrix vector products.

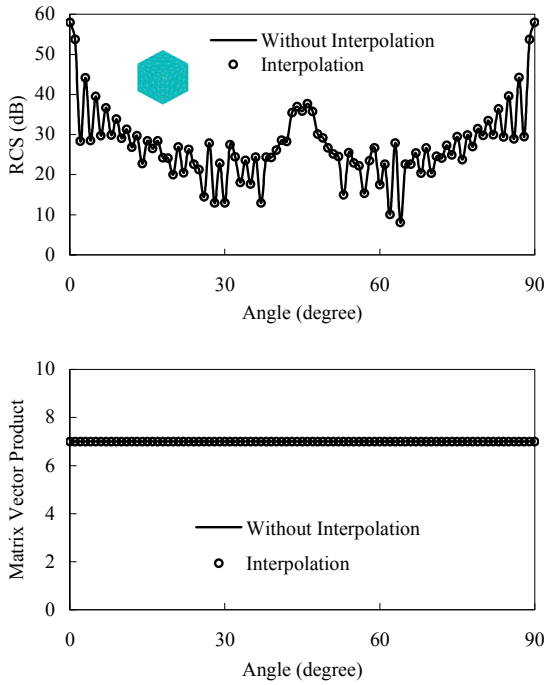

Fig. 2. Cube: (a) RCS for VV-polarization, 300 MHz; (b) Number of matrix vector products.

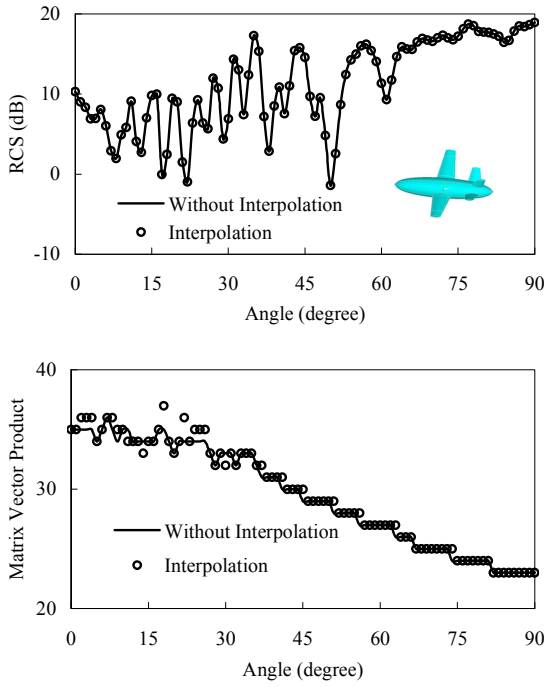

Fig. 3. Plane: (a) RCS for VV-polarization, 600 MHz; (b) Number of matrix vector products.

In our simulations, 6 uniform samples are required in the impedance matrix interpolation method for these three examples. As shown in Fig. 1(a), Fig. 2(a) and Fig. 3(a), it can be seen that the impedance matrix interpolation method is an accurate method and the impedance matrix interpolation method is more efficient than the traditional method. As shown in Fig. 1(b), Fig. 2(b) and Fig. 3(b), there is no difference for the number of the matrix-vector production when the SAI matrices are interpolated. It can be concluded that almost the same convergence can be obtained whether the SAI matrix is constructed by interpolation method or not.

Since the elements of the impedance matrix is a simple function of the angle, only few sampling angles are needed for a wide angular band. That is, only few solution processes of the linear system constructed by method of moment are needed for a wide angular band. This property is also valid for frequency sweep. In this paper, the angular sweep is focused on and only 6 uniform samples are computed for every example. The number 6 is an experience parameter. Generally speaking, interpolation results are inaccurate. In this paper, the interpolation method is used to interpolating the impedance matrix and preconditioning matrix. Definitely, there is some difference between the exact results and interpolation results. The difference will influence the surface electrical current distribution. However, the RCS is the logarithmic function of current. Accordingly, the difference will not impact the RCS greatly.

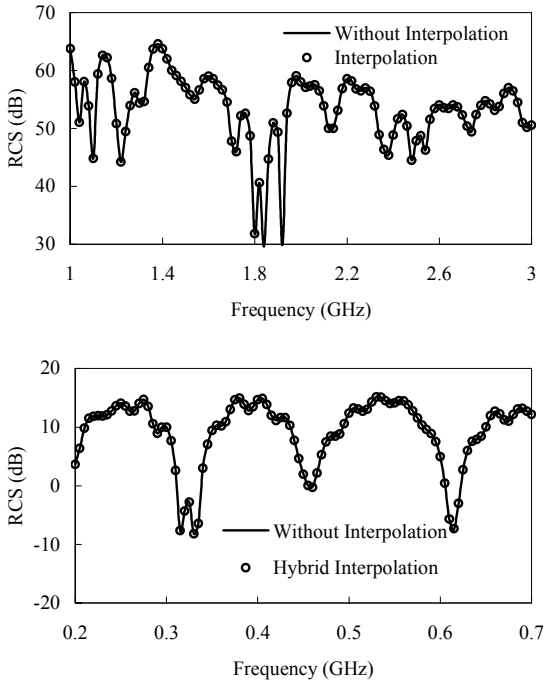

Fig. 4. RCS for frequency sweep: (a) Cube, 1 GHz ~ 3 GHz; (b) Plane, 200 MHz ~ 700 MHz.

In order to better understanding the proposed method, the results of frequency sweep are given from Fig. 4. Since this paper focuses on the monostatic RCS, only the RCS of the last two examples (Cube and Plane) are computed with respect to frequency.

From Fig. 4, it is concluded that the proposed method can also be used for frequency sweep. The interpolation results are almost the same as the reference results. Either angle sweep or frequency sweep, the elements of the impedance matrix are calculated by integral of Green's function. Since the Green's function takes the form of exponential function which is easily to be approximated by rational function, the MBPE could be able to perform good results in impedance matrix interpolation.

When the method of moment is used for the computation of radar cross section, the main problem is to solve the linear system $\mathbf{Ax} = \mathbf{b}$. For computation of monostatic RCS, especially asymptotic phase basis is used, the impedance matrix $\mathbf{A}$ will be modified according to the incident angle. The interpolation method can not be applied for induced current $\mathbf{x}$. A good way for better efficient simulation is to interpolating the impedance matrix. That is, cost more memories to achieve less computation time. From the results of this paper, MBPE performs well for interpolating both impedance matrix and pre-conditioner matrix.

Table 1: Construction time for impedance matrix (Time: second)

Object	Unknown	Impedance without Interpolation	Impedance with Interpolation
Cylinder	4279	7211	628
Cube	7137	9980	1041
Plane	10968	63742	7734

Table 2: Construction time for SAI preconditioning matrix (Time: second)

Object	Unknown	SAI without Interpolation	SAI with Interpolation
Cylinder	4279	1527	143
Cube	7137	543	58
Plane	10968	19080	2045

Table 3: Total solution time for fast frequency sweep (Time: second)

Object	Unknown	Frequency	Angular Band	Without Interpolation	Hybrid Interpolation
Cylinder	4279	300 MHz	0~90°	10423	3954
Cube	7137	300 MHz	0~90°	12654	3872
Plane	10968	600 MHz	0~90°	92718	19877

As shown in Tab.1, the construction time of near field impedance matrices are compared between traditional method and interpolation method for these three examples. As shown in Tab.2, the construction time of SAI matrices are compared between traditional method and interpolation method for these three examples. It can be found that the computational cost of the interpolation method is much less. The main cost of impedance and SAI interpolation method is the construction time and memory requirement for those angular sampling points. The memory requirement to save samples of near-field impedance matrices and preconditioning matrices is 147 MB for the first example, 254 MB for the second example and 1.34GB for these three examples. As shown in Tab. 3, the total computation time is compared for the frequency sweep. "*Without Interpolation*" means impedance matrix constructed directly and SAI pre-conditioner constructed directly. "*Hybrid Interpolation*" means impedance matrix interpolation and SAI preconditioning method interpolation with the

rational interpolation method. It can be also found by comparison that the large calculation time can be saved when the hybrid interpolation technique is used.

V. CONCLUSION

In this paper, the asymptotic phase basis function and impedance matrix interpolation method is combined together to analyze the monostatic scattering from electrically large objects over a wide angular band. The impedance matrix is approximately constructed by MBPE method at each incident angle. The MLFMA and Krylov subspace iterative solver are used and the SAI is used to accelerate the convergence. In order to further reduce the computation time of constructing SAI preconditioning matrix, the MBPE technique is used for construction of SAI matrices at each angle. Numerical experiments demonstrate that our proposed hybrid interpolation method is more efficient when compared with the traditional method for electromagnetic scattering from the electrically large objects.

ACKNOWLEDGEMENTS

The authors would like to thank the support of National Science Foundation of China (No: 61261005, No: 61061002), Youth Science Foundation of Jiangxi (No: 20122BAB211018), Youth Science Foundation of Education Department of Jiangxi (No: GJJ11112) and East China Jiaotong University Foundation (No: 11XX01).

References

[1] R. F. Harrington, *Field Computation by Moment Methods*, Malabar, Fla.: R. E. Krieger, 1968.

[2] W. C. Chew, J. M. Jin, E. Michielssen, and J. M. Song, *Fast and Efficient Algorithms in Computational Electromagnetics*. Boston, MA: Artech House, 2001.

[3] J. M. Song, C. C. Lu and W. C. Chew, "Multilevel Fast Multipole Algorithm for Electromagnetic Scattering by Large Complex Objects," *IEEE Trans*. *Antennas Propagat*., vol. 45, no. 10, pp. 1488-1493, 1997.

[4] J. R. Mautz and R. F. Harrington, "H-field, E-field, and Combined Field Solution for Conducting Bodies of Revolution," Arch. Elecktron. Übertragungstech (AEÜ), vol. 32, pp. 157-164, 1978.

[5] Z. Nie, S. Yan, S. He, and J. Hu, "On the Basis Functions with Travelling Wave Phase Factor for Efficient Analysis of Scattering from Electrically Large Targets," *Progress In Electromagnetics Research*, PIER 85, pp. 83-114, 2008.

[6] Su Yan, Shiquan He, Zaiping Nie, and Jun Hu, "Calculating the Wide Band Responses from Metallic Objects by Employing the Phase Extracted Basis Functions," *IEEE International Symposium on Antennas and Propagations*, 2008.

[7] John Robert Gulick, "A Combination of Rao-Wilton-Glisson and Asymptotic Phase Basic Functions to Solve the Electric and Magnetic Field Integral Equations," Master of science Department of Electrical and Computer Engineering, 2001.

[8] I. G.-T., J. M. Taboada, J. L. R, F. Obelleiro, and L. Landesa, "Efficient Asymptotic-Phase Modeling of the Induced Currents in the Fast Multipole Method," *Microwave and Optical Technology Letters*, vol. 48, no. 8, Aug. 2006.

[9] M. Benzi and M. Tuma, "A Sparse Approximate Inverse Preconditioner for Nonsymmetric Linear Systems," *SIAM Journal on Scientific Computing*, vol. 19, pp. 968-994, 1998.

[10] P. L. Rui and R. S. Chen, "An Efficient Sparse Approximate Inverse Preconditioning for FMM Implementation," *Micro*. *Opt*. *Tech*. *Lett*., vol. 49, no. 7, pp. 1746-1750, 2007.

[11] E. H. Newman, "Generation of Wide-band Data from the Method of Moments by Interpolating the Impedance Matrix," *IEEE Trans*. *Antennas Propagat*, vol. 36, no. 12, pp. 1820-1824, 1988.

[12] K. L. Virga and Y. R. Samii, "Efficient Wide-Band Evaluation of Mobile Communications Antennas using Z or Y Matrix Interpolation with the Method of Moments," *IEEE Trans*. *Antennas Propagat*, vol. 47, no. 1, pp. 65-76, 1999.

[13] X. C. Wei, E. P. Li, "Wide-band EMC Analysis of On-platform Antennas using Impedance-Matrix Interpolation with the Moment of Method-Physical Optics Method," *IEEE Trans*. *Electromagnetic Compatibility*, vol. 45, no. 3, pp. 552-556, 2003.

[14] G. J. Burke, E. K. Miller, S. Chakrabarthi, and K. Demarest, "Using Model-Based Parameter Estimation to Increase the Efficiency of Computing Electromagnetic Transfer Functions," *IEEE Trans*. *Magn*., vol. 25, pp. 2807-2809, July 1989.

[15] C. J. Reddy, M. D. Deshpande, C. R. Cockresll, and F. B. Beck, "Fast RCS Computation Over a Frequency Band using Method of Moments in Conjunction with Asymptotic Waveform Evaluation Technique," *IEEE Trans*. *Antennas Propagat*, vol. 46, no. 8, pp. 1229-1233, August 1998.

[16] Y. E. Erdemli, J. Gong, C. J. Reddy, and J. L.Volakis, "Fast RCS Pattern Fill Using AWE Technique," *IEEE Trans*. *Antennas Propagat*, vol. 46, no. 11, pp. 1752-1753, November 1998.

[17] R. D. Slong, R. Lee, and J. F. Lee. "Multipoint Galerkin Asymptotic Waveform Evaluation for Model Order Reduction of Frequency Domain

FEM Electromagnetic Radiation Problems," *IEEE Trans. Antennas Propagat*, vol. 49, no. 10, pp. 1504-1513, October 2001.

[18] M. S. Chen, X. L. Wu, W. Sha and Z. X. Huang, "Fast and Accurate Radar Cross-Section Computation over a Broad Frequency Band using the Best Uniform Rational Approximation," *IET Micro. Antennas Propag.*, vol. 2, no. 2, pp. 200-204, 2008.

[19] Z. W. Liu, D. Z. Ding, Z. H. Fan, and R. S. Chen, "Adaptive Sampling Bicubic Spline Interpolation Method for Fast Computation of Monstatic RCS," *Micro. Opt. Tech. Lett*. vol. 50, no. 7, pp. 1851-1857, July 2008.

[20] S. M. Rao, D. R. Wilton, and A. W. Glisson, "Electromagnetic Scattering by Surfaces of Arbitrary Shape," *IEEE Trans. Antennas Propagat*, vol. 30, no. 3, pp. 409-418, 1982.

[21] Y. Saad and M. Schultz, "GMRES: A Generalized Minimal Residual Algorithm for Solving Nonsymmetric Linear Systems," *SIAM J. Sci. Stat. Comput.*, vol. 7, no. 3, pp. 856-869, 1986.

[22] Valeria Simoncini, and Daniel B. Szyld, "Flexible Inner-Outer Krylov Subspace Methods," *SIAM J. Numer. Anal.*, vol. 40, no. 6, pp. 2219-2239, 2003.

[23] Z. H. Fan, Z. W. Liu, D. Z. Ding, R. S. Chen, "Preconditioning Matrix Interpolation Technique for Fast Analysis of Scattering over Broad Frequency Band," *IEEE Trans. Antenna and Propagation*, vol. 58, no. 7, pp. 2484-2487, July 2010.

[24] B. M. Kolundzija, M. S. Tasic, D. I. Olcan, D. P. Zoric, S. M. Stevanetic, "Advanced Techniques for Efficient Modeling of Electrically Large Structures on Desktop PCs," *Applied Computational Electromagnetics Society* (*ACES*) *Journal*, vol. 27, no. 2, pp. 123-131, February 2012.

[25] Z. N. Jiang, R. S. Chen, Z. H. Fan, S. G. Shen, X. Q. Hu, "Efficient Multilevel Compressed Block Decomposition for Large-Scale Electromagnetic Problems Using Asymptotic Phasefront Extraction," *Applied Computational Electromagnetics Society* (*ACES*) *Journal*, vol. 26, no. 11, pp. 876-885, November 2011.

[26] Z. Liu, R. Chen, J. Chen, Z. Fan, "Using Adaptive Cross Approximation for Efficient Calculation of Monostatic Scattering with Multiple Incident Angles," *Applied Computational Electromagnetics Society* (*ACES*) *Journal*, vol. 26, no. 4, pp. 325-333, April 2011.

[27] Z. N. Jiang, Z. H. Fan, D. Z. Ding, R. S. Chen, K. W. Leung, "Preconditioned MDA-SVD-MLFMA for Analysis of Multi-scale Problems," *Applied Computational Electromagnetics Society* (*ACES*) *Journal*, vol. 25, no. 11, pp. 914-925, November 2010.

[28] R. J. Burkholder, Ç. Tokgöz, C. J. Reddy, W. O. Coburn, "Iterative Physical Optics for Radar Scattering Predictions," *Applied Computational Electromagnetics Society* (*ACES*) *Journal*, vol. 24, no. 2, pp. 241-258, April 2009.

[29] R. Mittra, "Characteristic Basis Function Method (CBFM)—an Iteration-Free Domain Decomposition Approach in Computational Electromagnetics," *Applied Computational Electromagnetics Society* (*ACES*) *Journal*, vol. 24, no. 2, pp. 204-223, April 2009.

Yuejin Zhang was born in Hubei, China in 1978. He received B.S. degree in Communication Engineering from PLA Second Artillery Command College in 2002, M.S. degree in Computer Application Technology from East China Jiaotong University in 2008, respectively. He is currently working at School of Information Engineering, East China Jiaotong University. His research interests focus on the theory of electromagnetic scattering and inverse scattering.

Dechang Huang was born in Jiangxi, China in 1982. He received B. S. and M. S. degree in Communication Engineering from East China Jiaotong University in 2006 and 2011, respectively. He is currently working at School of Information Engineering, East China Jiaotong University. His research interests focus on the high frequency circuit and electromagnetics.

Jiaqi Chen was born in Gansu, China. He received the B.S. degrees in communication engineering from Nanjing University of Science and Technology (NUST), in 2005, and Ph.D. degree in Nanjing University of Science & Technology in 2012, respectively. He was with the Center for Sensor systems (ZESS), University of Siegen, Siegen, Germany, as a visiting scholar in 2009. He is currently working at Computer and Information College, Hohai University. His research interests include computational electromagnetics, SAR imaging and precipitation radar.

A Novel Compact Planar Spiral-shaped Antenna

Bing Xiao, Lei Zhong, Jing-Song Hong, and Song-Lin Li

The Institute of Applied Physics
University of Electronic Science and Technology of China, Chengdu, 610054
bxuestc@gmail.com

Abstract ― A novel compact spiral antenna with planar feed structure is presented. The proposed antenna is a two-arm Archimedean spiral antenna, which has similar properties of wideband and circular polarization to traditional one. A remarkable improvement of the proposed antenna is the completely planar feed structure. The whole antenna is compact， its spiral diameter is only 23.2mm and the balun is also small. It has an impedance bandwidth of 67% from 4.5GHz to 9GHz and a 4-dB axial-ratio bandwidth of 46.67% ranging from 4.6 GHz to 7.4 GHz. It can be widely used in wideband planar antenna array and other low profile applications.

Index Terms ― circular polarization, planar antenna arrays, spiral antennas, wideband antennas.

I. INTRODUCTION

Wideband planar antennas have been widely used in aircraft, satellite, radar, remote control, telemetry, etc., especially when bandwidth, profile, conformal installation, weight and cost are main concerns of the users. In terms of polarization of wideband planar antenna, circular polarization (CP) is more attractive than linear polarization. CP can facilitate easy orientations between transmitters and receivers and has high degree of mobility, weather penetration, and reduction in multipath reflections and other kinds of interferences [1].

Several kinds of wideband antennas can accommodate the demand of both planar structure and circular polarization. Microstrip antenna is the most commonly used antenna. Basically, there are two techniques to generate circular polarization for a single microstrip patch. One is to excite the square or circular patch by two orthogonally located feeds. The other is to employ an irregular physically perturbed patch that is excited by a single feed. However, two feed points greatly complicate the feed network, while irregular shape of the patch breaks up the symmetry radiation [2, 3]. Most of all, microstrip antenna is an inherent narrow band antenna, so it is difficult to expand bandwidth significantly. Therefore, new techniques of planar wideband circularly polarized antenna should be explored.

Spiral antennas have emerged as leading candidates for various commercial and military applications requiring wideband circularly polarized operation [4]. Spiral antennas are inherent frequency-independent antennas. For instance, they can achieve bandwidth up to 40:1 [5] and offer high-quality circular polarization, because their input impedances are near constant over the entire operating frequency range. In recent years, various spiral antennas have been developed [6-9].

However, conventional spiral antenna is always fed by a balun, which is perpendicular to the spiral plane in the center [10-12]. Therefore, they cannot be completely planar and encounter serious difficulties in the planar integration of spiral antenna.

To design a planar feed structure for spiral antenna, several attempts have been made over the past few years [13-16]. Some authors use slotlines instead of strips for the convenience of planar feed [13-15]. As we all know, slotline is a dispersion transmission line, whose phase velocity varies with the frequency. Thus it will affect the group delay time of wideband antenna. Some other spiral antennas are designed by strips, but they do not have a compact and simple structure for microstrip feed [16]. Apparently, a compact planar spiral

Submitted On: Mar. 28, 2012
Accepted On: Dec. 16, 2012

antenna fed by microstrip is much more adaptable to low profile applications, such as planar antenna array.

This article investigates the possibility of a completely planar spiral antenna. The antenna is a spiraled coplanar stripline (CPS) fed by a novel compact microstrip-to-CPS balun. It shows wideband left hand circular polarization (LHCP) on front side and right hand circular polarization (RHCP) radiation pattern on back side. The simulation and experimental results show an impedance bandwidth of 67% from 4.5GHz to 9GHz and 4-dB axial-ratio bandwidth of 46.67% from 4.6 GHz to 7.4 GHz, whose radiation characteristics are similar to center-fed spiral antenna.

II. DESIGN OF SPIRALS

Figure 1 shows the configuration of the spirals. A CPS line is wound around the center. Thus, the two strips of CPS become an inner spiral and an outer spiral. The distance from the center to a strip is defined as r, which is expressed as $r=r_0+a\varphi$, where r_0 is the initial radius, a is the growing rate, and φ is the winding angle. This expression comes from the classical Archimedean spiral antenna [11].

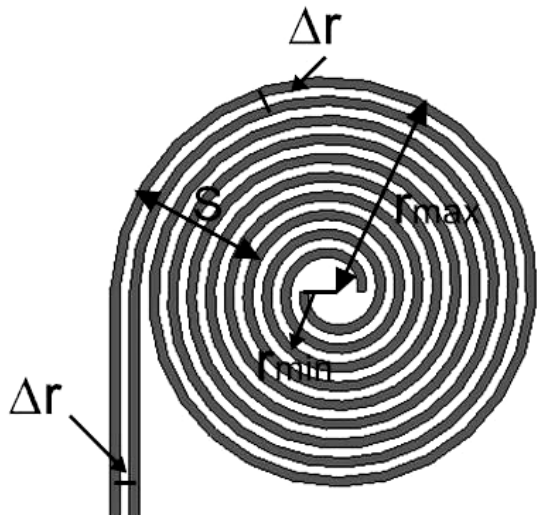

Fig. 1. Configuration of the spirals.

In order to get a symmetrical structure, the end of outer spiral is wound half a turn further in the center. According to the band theory [11], the lower frequency limit of the operation band can be determined by judging whether the currents in neighboring arms are in phase. The start of two spiral strips is a typical CPS, and the currents on the two strips are in antiphase. Therefore, the electromagnetic field is bound between the two strips and does not radiate.

However, the different radii lead to a different length between the two strips of CPS while winding. If the different length is equal to half a wavelength, the currents will be in phase, and the electromagnetic field will radiate. When a CPS line (two spiral strips) is wound by 360°, the phase difference is $2\pi\Delta r$ (Δr is the distance between every two adjacent spiral strips). Thus, we assume the radiation occurs at a distance $s \sim s+\Delta r$ along the circumference and CPS is wound by n turns, then

$$n \cdot 2\pi \cdot \Delta r = \frac{\lambda_g}{2}. \tag{1}$$

So

$$s = 2n \cdot \Delta r = \frac{\lambda_g}{2\pi}, \tag{2}$$

where λg is the guided wavelength on the spiral arms. It is worthwhile to note that the distance s is independent from both the arm spacing Δr and the number of turn n. It is only proportional to the guided wavelength of corresponding frequency. Apparently, s cannot exceed the radius of radiation part r_{max}. If the minimum frequency of the antenna is f_{min}, the maximal s can be calculated by

$$s_{(f\min)} = \frac{c_0}{2\pi\sqrt{\varepsilon_{eff}} \cdot f_{\min}}, \tag{3}$$

where c_0 is the speed of light in free space and ε_{eff} is the effective relative dielectric constant of CPS. As we use a 0.8-mm-thick RO4003C substrate (relative dielectric constant ε_r=3.38), the effective relative dielectric constant is 2.04 [17]. Thus $s_{(fmin)}$ is calculated as 5.8mm, according to (3).

In fact, r_{max} should be twice as long as $s_{(fmin)}$ in reality. Based on the principles mentioned above, if $r_{max} = s_{(fmin)}$, the effective radiation area of the minimum frequency should be the center point of the spiral strips. Since the currents are cut at this point, there cannot be any effective radiation here. So we define the initial value of r_{max} as 11.6mm. And r_{min} is designed as 1.8mm in order to keep the end of two spirals apart in the center.

Additionally, strip width Ws and gap width Wg (Wg=Δr-Ws) are designed as equal value. In the classical theory of Archimedean spiral

antenna, a self-complementary structure is modeled, when strip width is equal to gap width. The largest bandwidth and the lowest input impedance can be achieved at the same time. As spiral antenna is a travelling wave structure, the signal travels along spirals and the intensity decays gradually. Hence the input impedance of the antenna is the same as the characteristic impedance of CPS feed line.

In order to match the spirals to a 50Ω microstrip line, Ws=Wg=0.6mm are set as initial value for lower input impedance.

Growing rate of spirals, determined by Wg, Ws, and r_{max}, is set as 0.38mm/rad.

Figure 2 shows the simulated electric field intensity distribution at four different frequency points (4.7 GHz, 5.6 GHz, 6.5 GHz and 7.4 GHz). The bright area represents high intensity while the dark area represents low intensity. Radiation occurs where high intensity decreases to low intensity, because the reduced intensity has become radiation energy and radiated outward. Consistent with the theoretical analysis, the higher the frequency is, the outer the radiation area locates.

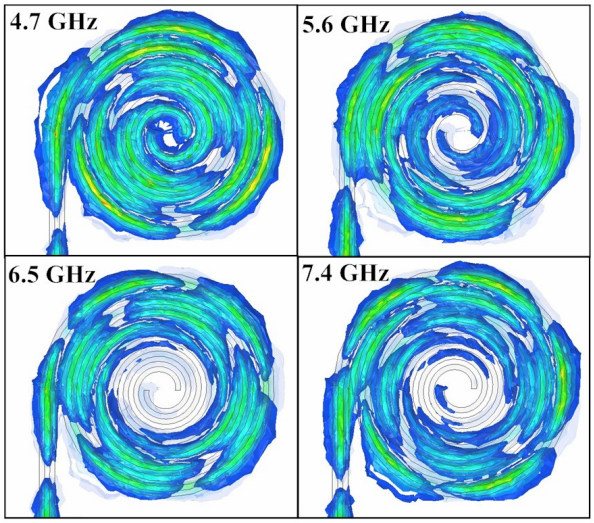

Fig. 2. Electric field intensity distributions at four different frequencies.

III. DESIGN OF CPS-TO-MICROSTRIP BALUN

The input impedance of spirals is decided by both strip width Ws and gap width Wg. Figure 3 shows the simulated real and imaginary parts of the input impedance of the spirals. Below 5GHz the input impedance changes dramatically with frequency and the spirals are difficult to match with a balun. Ranging from 5GHz to 9GHz, the two curves are less oscillatory, and the magnitude of the input impedance is nearly a constant with an average of 175Ω. We can design a microstrip-to-CPS balun to feed the CPS structure in this band, where both field matching and impedance matching need to be considered [18].

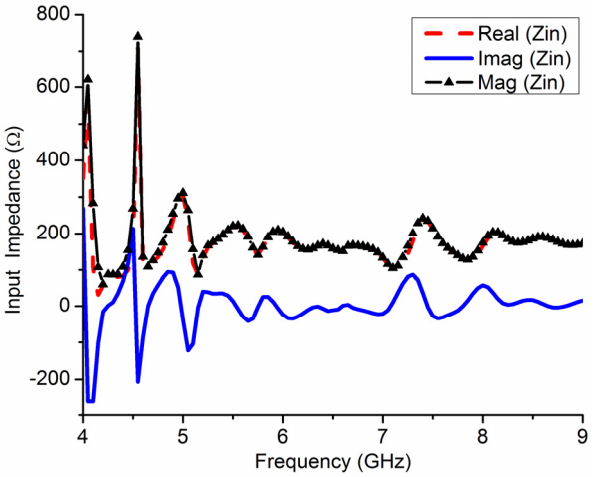

Fig. 3. Real part, imaginary part and magnitude of the input impedance of the spirals.

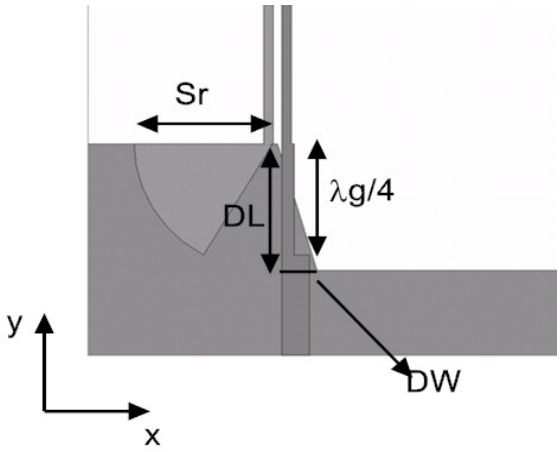

Fig. 4. Wide-band CPS-to-microstrip balun.

Recently, several CPS-to-microstrip baluns on low dielectric-constant substrate have been reported [19-21]. These baluns use a long smooth tapered microstrip line to match high characteristic impedance of CPS. The proposed structure in this paper is compact and satisfying.

Figure 4 shows the proposed wide-band CPS-to-microstrip balun based on coupling method.

The transition consists of a microstrip stepped matching transformer, a radial stub and a quadrangle-defected ground.

Since the input impedance of the CPS is about 175Ω, a 94Ω quarter-wavelength transformer is assigned to match 175Ω and 50Ω.

As the electric field in the microstrip line is parallel to z-axis and the electric field in the CPS is parallel to x-axis, a 90°electric-field rotation is needed. So a quadrangle defected ground structure (DGS) is employed to rotate the direction of electric field. The DGS can avoid mutual interference by keeping spirals and ground apart. This balun has advantages of wide bandwidth, low loss, and compactness.

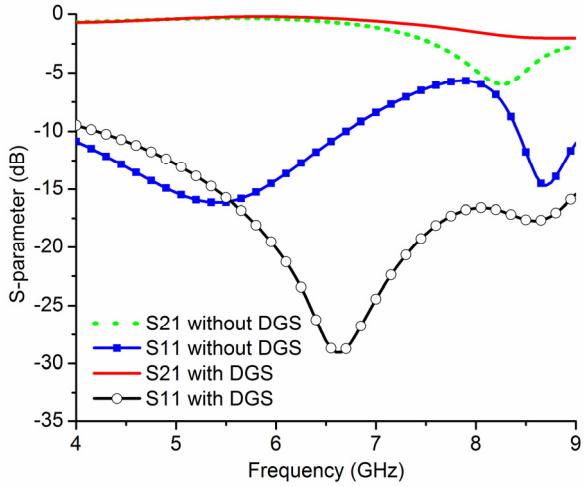

Fig. 5. S21 and S11 curves of the balun with and without the quadrangle DGS.

Figure 5 shows S21 and S11 curves of the balun with and without the quadrangle DGS. As shown in Fig. 5, the transmission coefficient is higher and the return loss is lower when the ground is truncated.

Since the quarter-wave radial stub can be seen as virtual short, it is in equal potential with the ground plane. Thus at the start of radial stub, electric field on CPS begins to couple into the ground. When the ground plane is gradually formed, the electric field intensity between strip and ground is gradually stronger (microstrip) and that between two strips (CPS) is gradually weaker. So we can reduce the reflection loss to the maximum extent, and the quasi-TEM mode of microstrip is obtained.

Additionally, *Sr* should theoretically be quarter guided wavelength of the center frequency. However, according to the results of full wave simulation, *Sr* has a relatively big impact on the axial ratio of the spiral antenna, which is probably because *Sr* decides the phase difference at the start of CPS. *Sr* is defined as 6.1mm to balance the transmission efficiency and axial ratio.

IV. SIMULATION AND MEASUREMENT RESULTS

Based on the analysis above and simulations results with Ansoft HFSS 13, the detailed dimensions of the proposed antenna are showed in Table 1.

The validity of the presented design was tested by a prototype, as shown in Fig. 6. The manufactured spiral antenna was tested by a vector network analyzer.

Figure 7 shows the simulated and measured return loss of the proposed antenna. The bandwidth of 10 dB return loss covers from 4.5 to 9GHz.The LHCP and RHCP radiation patterns at 4.7 GHz, 5.6 GHz, 6.5 GHz and 7.4 GHz are shown in Fig. 8 (a)-(d) respectively. The radiation patterns are similar to conventional center-fed spiral antenna at 4.7 GHz, 5.6 GHz and 6.5 GHz, whereas at 7.4 GHz, the radiation pattern is degraded. This is because the asymmetry brought by the feed line has a greater impact when radiation occurs at outer part of spirals. Additionally the circular polarization property is also worse, as is shown in Fig. 9. If the radius of the spiral r_{max} increases, the radiation pattern and the axial ratio at higher frequency will be probably improved, but the size will be even bigger.

Table 1: Dimensions of the Proposed Antenna

Substrate: RO4003C (ε_r=3.38, tanδ=0.002, h=0.8mm)			
r_{max}	11.6 mm	*Ws*	0.6 mm
r_{min}	1.8 mm	*Wg*	0.6 mm
DL	9 mm	*Sr*	6.1 mm
DW	2.6 mm	$\lambda_g/4$	7.9 mm
a	0.38 mm/rad	*n*	4.5

Figure 9 shows the simulated broadside axial ratio versus frequency. Generally, the 4-dB axial ratio bandwidth covers from 4.6 GHz to 7.4 GHz. The simulated broadside gain is shown in Fig. 10.

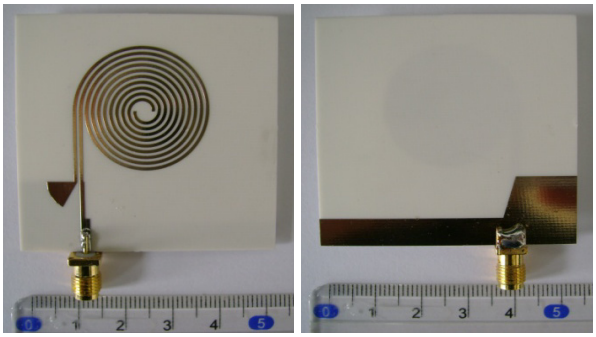

(a) The top view, (b) The bottom view,

Fig. 6. Photograph of the proposed antenna: (a) the top view, (b) the bottom view.

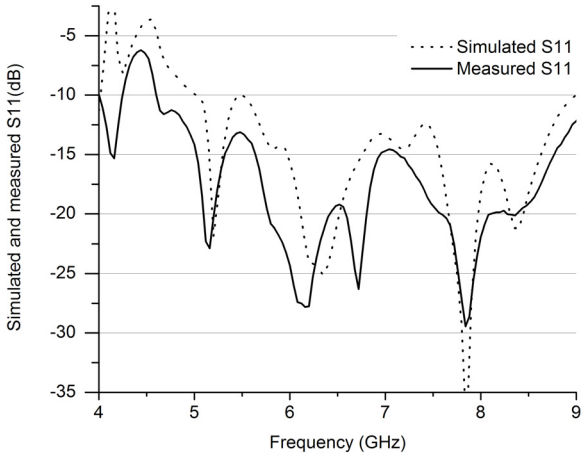

Fig. 7. The simulated and measured return loss.

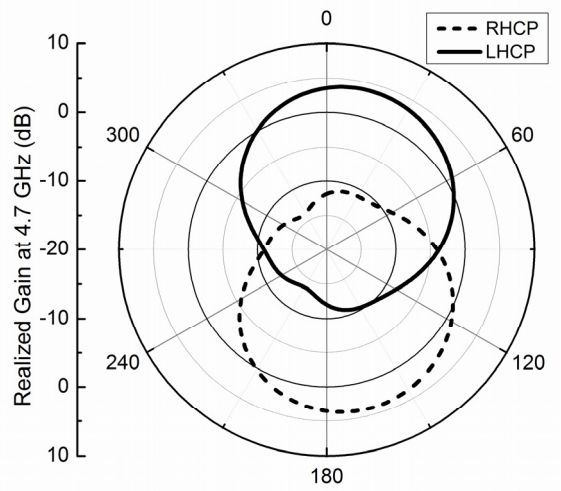

(a) 4.7 GHz,

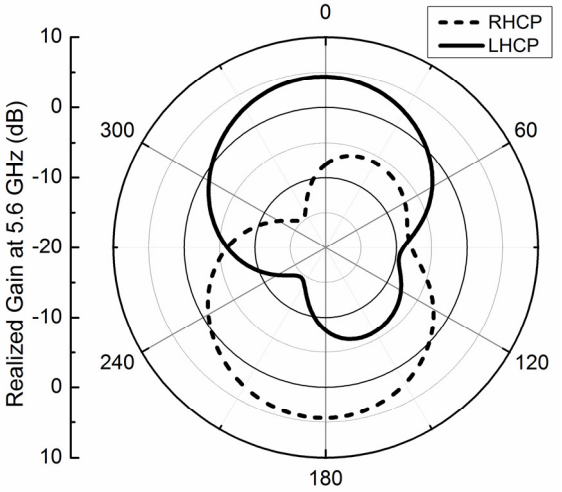

(b) 5.6 GHz,

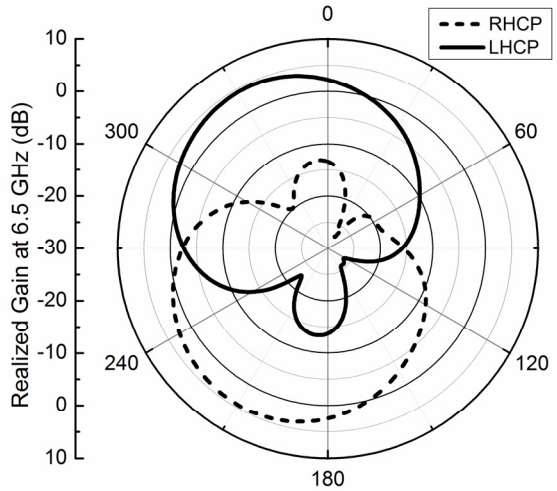

(c) 6.5 GHz,

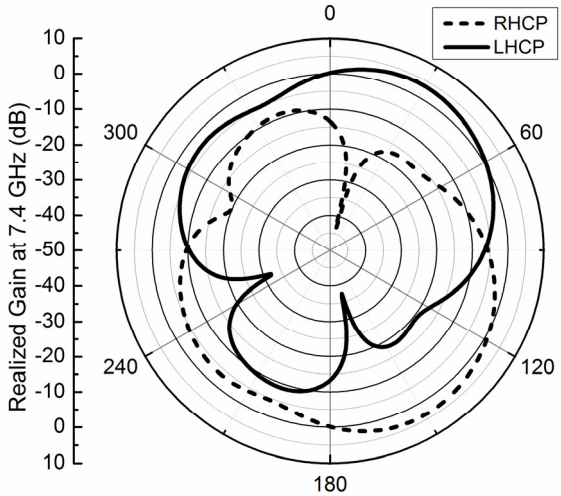

(d) 7.4 GHz,

Fig. 8. Radiation patterns at different frequencies, (a) 4.7 GHz, (b) 5.6 GHz, (c) 6.5 GHz and (d) 7.4 GHz.

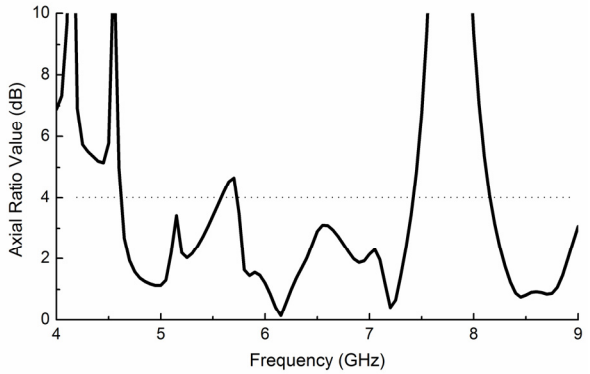

Fig. 9. Broadside axial ratio versus frequency.

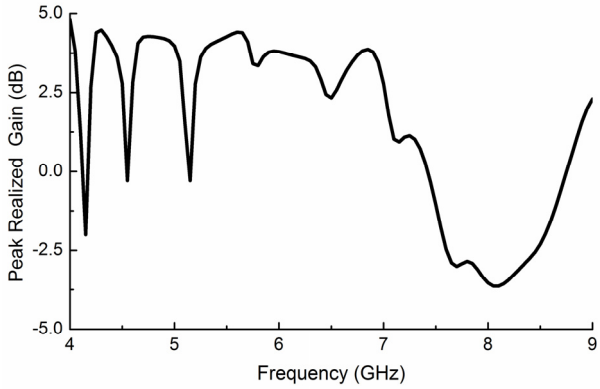

Fig. 10. Broadside gain versus frequency.

V. CONCLUSION

A compact planar spiral-shaped circularly polarized antenna is proposed. This antenna has a compact structure and wideband property, so it can be integrated in planar antenna arrays. However, the performance of this spiral antenna is not as excellent as the traditional center-fed one. Because the external feed destroys symmetry of spirals, and the ground of microstrip affects radiation characteristics especially at the higher frequency band. There is still much room for improvement of bandwidth and circular polarization for future research.

ACKNOWLEDGMENT

This work was supported by the National Natural Science Foundation of China (No.61172115 and No.60872029), the High-Tech Research and Development Program of China (No. 2008AA01Z206), the Aeronautics Foundation of China (No.20100180003), and the Fundamental Research Funds for the Central Universities (No.ZYGX2009J037).

REFERENCES

[1] R. Garg, *Microstrip Antenna Design Handbook*, Artech house publishers, 2001.

[2] A. Chen, Y. Zhang, Z. Chen, et al. "Development a Ka-Band Wideband Circularly Polarized 64-element Microstrip Antenna Array with Double Application of the Sequential Rotation Feeding Technique," *IEEE Antennas and Wireless Propagation Letters,* vol. 10, pp. 1270-1273, 2011.

[3] C. S. Ong, M. F. Karim, L. C. Ong, et al. "A Compact 2× 2 Circularly Polarized Antenna Array for Energy Harvesting," *Asia-Pacific Microwave Conference Proceedings (APMC)*, pp. 1977-1980, 2010.

[4] J. Dyson, "The Equiangular Spiral Antenna," *IRE Transactions on Antennas and Propagation.* vol. 7, no. 2, pp. 181-187, 1959.

[5] W. L. Stutzman, G. A. Thiele, *Antenna Theory and Design*, J. Wiley, 1998.

[6] N. Rahman, A. Sharma, M. Asfar, S. Palreddy, R. Cheung, "Dielectric Characterization and Optimization of Wide-band, Cavity-Backed Spiral Antennas," *Applied Computational Electromagnetics Society (ACES) Journal*, vol. 26, no. 2, pp. 123 - 130, February 2011.

[7] S. Palreddy, A. I. Zaghoul, R. Cheung, "Study of the Effects of the Back Cavityon a Broadband Sinuous Antenna and an Optimized Loaded Back Cavity," *Applied Computational Electromagnetics Society (ACES) Journal*, vol. 26, no. 8, pp. 660-666, August 2011.

[8] S. K. Khamas, G. G. Cook, "Optimised Design of a Printed Elliptical Spiral Antenna with a Dielectric Superstrate," *Applied Computational Electromagnetics Society (ACES) Journal*, vol. 23, no. 4, pp. 345-351, December 2008.

[9] C. Fumeaux, D. Baumann, R. Vahldieck, "FVTD Characterization of Substrate Effects for Archimedean Spiral Antennas in Planar and Conformal Configurations," *Applied Computational Electromagnetics Society (ACES) Journal,* vol. 20, no. 3, pp. 186-187, November 2005.

[10] E. Gschwendtner, W. Wiesbeck, "Frequency-Independent Antenna Concepts for the Use in Vehicles," *International Crimean Microwave and Telecommunication Technology*, pp. 39-42, 2000.

[11] J. Kaiser, "The Archimedean Two-Wire Spiral Antenna," *IRE Transactions on Antennas and Propagation ,* vol. 8, no. 3, pp. 312-323, 1960.

[12] M. Veysi, M. Kamyab, Bandwidth "Enhancement of Low-profile PEC-Backed Equiangular Spiral Antennas Incorporating Metallic Posts," *IEEE Trans. Antennas and Propagation,* vol. 99, no. 1, 2011.

[13] D. S. Filipovic, A. U. Bhobe, T. P. Cencich, "Low-Profile Broadband Dual-Mode Four-Arm Slot Spiral Antenna with Dual Dyson Balun Feed," *IEE Proceedings Microwaves Antennas and Propagation*, pp. 527-533, 2005.
[14] W. Z. Wu, T. H. Chang, J. F. Kiang, "Broadband Slot Spiral Antenna with External Feed and Microstrip-to-Slotline Transition," *IEEE APSI symp.*, pp. 767-770, 2004.
[15] E. Gschwendtner, D. Loffler, W. Wiesbeck, "Spiral Antenna with External Feeding for Planar Applications," *IEEE Africon,* pp. 1011-1014, 1999.
[16] E. Gschwendtner, J. Parlebas, W. Wiesbeck, "Spiral Antenna with Planar External Feeding," *29th European Microwave conference*, vol. 1, pp. 135-138, 1999.
[17] I. J. Bahl, P. Bhartia, *Microwave Solid State Circuit Design*, Wiley-Interscience, 2003.
[18] J. S. Izadian, S. M. Izadian, *Microwave Transition Design*, Artech House, 1988.
[19] Y. H. Suh, K. Chang "A Wideband Coplanar Stripline to Microstrip Transition," *IEEE Microwave and Wireless Components Letters,* vol. 11, no. 1, pp. 28-29, 2001.
[20] T. Chiu, Y. S. Shen "A Broadband Transition Between Microstrip and Coplanar Stripline," *IEEE Microwave and Wireless Components Letters,* vol. 13, no. 2, pp. 66-68, 2003.
[21] W. H. Tu, K. Chang, "Wide-Band Microstrip-to-Coplanar Stripline/Slotline Transitions," *IEEE Trans. on Microwave Theory and Techniques,* vol. 54, no. 3, pp. 1084-1089, 2006.

Bing Xiao is a graduate student major in Radio Physics in the University of Electronic Science and Technology of China now. His research interests include antenna technology and wireless communication technique.

Lei Zhong is a graduate student major in Radio Physics in the University of Electronic Science and Technology of China now. His research interests include wideband antenna technology and wireless communication technique.

Jing-song Hong received the B.Sc. degree in electromagnetics from Lanzhou University, China, in 1991, and the M.Sc. and Ph. D. degrees in electrical engineering from the University of Electronic Science and Technology of China (UESTC), in 2000 and 2005, respectively. He is now a professor with UESTC. From 1991 to 1993, he was a Circuit Designer with the Jingjiang Radar Factory, Chengdu, China. From 1993 to 1997, he was a Testing Engineer with SAE Magnetics (HK) Ltd, Guangdong, China. From 1999 to 2002, he was a Research Assistant with the City University of Hong Kong. His research interest includes the use of numerical techniques in electromagnetics and the use of microwave methods for materials characterization and processing.

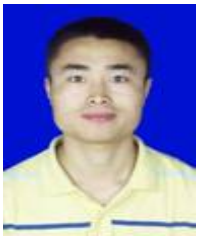

Song-lin Li is a graduate student major in Radio Physics in the University of Electronic Science and Technology of China now. His research interests include antenna technology and wireless charging technique.

Bandwidth Enhancement of Small Square Monopole Antenna with Dual Band-Notched Characterestics Using H-Ring Slot and Conductor Backed Plane for UWB Applications

Mohammad Ojaroudi [1], Nasser Ojaroudi [2], and Seyed Amin Mirhashemi [3]

[1] Young Researchers Club
Ardabil Branch, Islamic Azad University, Ardabil, Iran
m.ojaroudi@iauardabil.ac.ir

[2] Department of Electrical Engineering
Ardabil Branch, Islamic Azad University, Ardabil, Iran
n_ojaroudi@srttu.edu

[3] Department of Electrical Engineering
South Tehran Branch, Islamic Azad University, Tehran, Iran
mirhashemi_amin@yahoo.com

Abstract ─ This article proposes a novel printed monopole antenna for ultra wideband applications with dual band-notch function. The antenna consists of a square radiating patch and a ground plane with H-ring slot and conductor backed plane, which provides a wide usable fractional bandwidth of more than 125% (2.89-13.43 GHz). In order to generate single band-notched characteristic, we use an H-shaped conductor backed plane on the other side of the substrate. By converting this H-shaped conductor backed plane to H-ring form, a dual band-notched function is achieved and also by inserting an H- ring slot in the ground plane, additional resonances are excited and hence much wider impedance bandwidth can be produced, especially at the higher band. The measured results reveal that the presented dual band-notched monopole antenna offers a wide bandwidth with two notched bands, covering all the 5.2/5.8GHz WLAN, 3.5/5.5 GHz WiMAX and 4-GHz C bands. The designed antenna has a small size of 12×18 mm^2.

Index Terms ─ H-ring parasitic structure, H-ring slot, microstrip-fed monopole antenna, and ultra-wideband (UWB) applications.

I. INTRODUCTION

In UWB communication systems, one of key issues is the design of a compact antenna while providing wideband characteristic over the whole operating band. Consequently, a number of microstrip antennas with different geometries have been experimentally characterized. Moreover, other strategies to improve the impedance bandwidth, which do not involve a modification of the geometry of the planar antenna, have been investigated [1-4].

In UWB systems, the frequency range of 3.1 GHz to 10.6 GHz will cause interference to the existing wireless communication systems, such as, the wireless local area network (WLAN) for IEEE 802.11a operating in 5.15 GHz –5.35 GHz and 5.725 GHz – 5.825 GHz bands, WiMAX (3.3 GHz – 3.6 GHz), and C-band (3.7 GHz – 4.2 GHz); thus UWB antenna with a single and dual band-stop performance is required. In order to generate the frequency band-notch function antenna, modified planar monopole antennas have been recently proposed [5-8]. In [5] and [6], different shapes of the slits (i.e., W-shaped and folded trapezoid) are used to obtain the desired band-notched characteristics. Single and multiple [7] half-wavelength U-shaped slits are embedded in the radiation patch to generate the single and

Submitted On: Apr. 28, 2012
Accepted On: Dec. 26, 2012

multiple band-notched functions, respectively. In [8], band-notch function is achieved by using a T-shaped coupled-parasitic element in the ground plane.

In this paper, a new dual band-notch printed monopole antenna with multi resonance performance is presented. In the proposed structure, based on defected ground structure (DGS), by cutting an H-ring slot on the ground plane, additional resonances are excited and the bandwidth is improved to achieve a fractional bandwidth with multi resonance performance of more than 125 %. Also, based on electromagnetic coupling theory (ECT), single band-notched function is provided by inserting an H-shaped conductor backed plane and dual band-notch characteristic is obtained by using an H-ring conductor backed plane. The size of the designed antenna is smaller than the UWB antennas with band-notched function reported recently in [6-7]. Good VSWR and radiation pattern characteristics are obtained in the frequency band of interest. Simulated and measured results are presented to validate the usefulness of the proposed antenna structure for UWB applications.

II. ANTENNA DESIGN

The proposed square monopole antenna fed by a microstrip line is shown in Fig. 1, which is printed on a FR4 substrate of thickness 1.6 mm, and permittivity 4.4. The width of the microstrip feed line is fixed at 2 mm. The basic antenna structure consists of a square radiating patch, a feed line, and a ground plane. The patch is connected to a feed line, as shown in Fig. 1. On the other side of the substrate, a conducting ground plane is placed. The proposed antenna is connected to a 50Ω SMA connector for signal transmission.

Regarding DGS, the creating slots in the ground plane provide an additional current path. Moreover, this structure changes the inductance and capacitance of the input impedance, which in turn leads to change the bandwidth. The DGS applied to a microstrip line causes a resonant character of the structure transmission with a resonant frequency controllable by changing the shape and size of the slot [2]. Therefore, by cutting an H-ring slot at the ground plane and carefully adjusting its parameters, much enhanced impedance bandwidth may be achieved. As illustrated in Fig. 1, the H-shaped ring conductor backed plane is placed under the radiating patch and is also symmetrical with respect to the longitudinal direction. Based on ECT, the conductor backed plane perturbs the resonant response and also acts as a parasitic half-wave resonant structure electrically coupled to the rectangular monopole [3]. At the notched frequency, the current flows are more dominant around the parasitic element, and they are oppositely directed between the parasitic element and the radiation [3]. As a result, the desired high attenuation near the notch frequency can be produced.

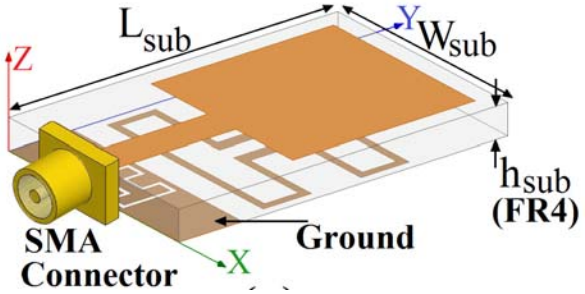

(a)

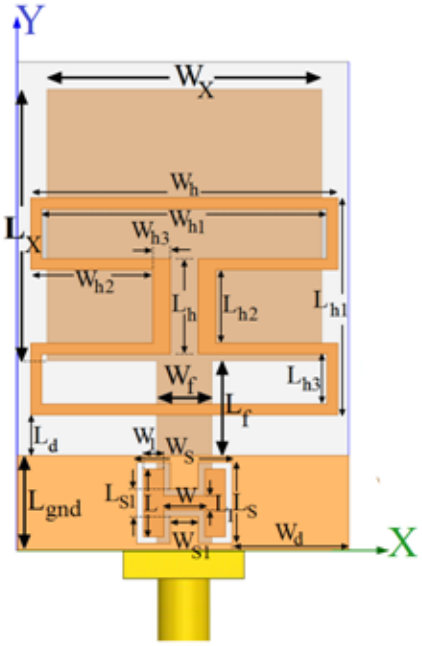

(b)

Fig. 1. Geometry of proposed microstrip-fed monopole antenna, (a) side view, (b) bottom view.

In this work, we start by choosing the dimensions of the designed antenna. These parameters, including the substrate, are $W_{sub} \times L_{sub}$ = 12 *mm* × *18 mm* or about $0.15\lambda \times 0.25\lambda$ at 4.2 GHz (the first resonance frequency). We have a lot of flexibility in choosing the width of the radiating patch. This parameter mostly affects the antenna bandwidth. As W_X decreases, so does the antenna bandwidth, and vice versa. Next step, we have to determine the length of the radiating patch L_X. This parameter is approximately (λ_{lower} / 4), where λ_{lower} is the lower bandwidth frequency wavelength. The wavelength λ_{lower} depends on a number of parameters such as the radiating patch width, as well as the thickness and dielectric constant of the substrate on which the antenna is fabricated [8]. The important step in the design is to choose $L_{resonance}$ (the length of the resonator) and L_{notch} (the length of the filters). $L_{resonance}$ is set to resonate at $0.25\lambda_g$, where $L_{resonance} = 2L_S - L_{S1} + 2W_1 + 0.5W_{S1}$, and λ_g corresponds to a new resonance frequency wavelength at 11.2 GHz. L_{notch} is set to band-stop resonance at $0.5\lambda_g$, where $L_{first\ notch} = L_{h2} + 2L_{h3} + W_{h1} + 2W_{h2}$, $L_{second\ notch} = 0.5L_h + L_{h3} + 0.5W_{h1} + W_{h2}$, and λ_g corresponds to notched band frequencies wavelength (3.9 GHz is the first notched frequency and 5.5 GHz is the second notched frequency). The optimized values of the proposed antenna design parameters are as follow:

W_{sub} = 12 *mm*, L_{sub} = 18 *mm*, h_{sub} = 1.6 *mm*, W_f = 2 *mm*, L_f = 3.5 *mm*, L_x = 10 *mm*, W_x = 10 *mm*, W_s = 3 *mm*, L_s = 3 *mm*, W_{s1} = 0.5 *mm*, L_{s1} = 1 *mm*, W = 1 *mm*, L = 2.5 *mm*, W_1 = 0.75 *mm*, L_1 = 0.5 *mm*, W_d = 4.5 *mm*, L_d, 1.5 *mm*, W_h = 11.5 *mm*, L_h = 3.5 *mm*, W_{h1} = 11 *mm*, L_{h1} = 8 *mm*, W_{h2} = 4.75 *mm*, L_{h2} = 3 *mm*, W_{h3} = 0.5 *mm*, L_{h3} = 2 *mm*, and L_{gnd} = 3.5 *mm*.

III. RESULTS AND DISCUSSIONS

The microstrip-fed monopole antenna were constructed and studied to demonstrate the effect of the proposed dual band-notch function and bandwidth enhancement technique. The numerical and experimental results of the input impedance and radiation characteristics are presented and discussed. The parameters of this proposed antenna are studied by changing one or two parameters at a time and fixing the others. The simulated results are obtained using the Ansoft simulation software high-frequency structure simulator (HFSS™) [9].

Figure 2 shows the structure of the various antennas used for simulation studies. VSWR characteristics for ordinary square patch antennas (Fig. 2(a)), with an H-shaped slot in the ground plane (Fig. 2(b)), and with an H-ring slot in the ground plane (Fig. 2(c)) are compared in Fig 3. As shown in Fig. 3, for the proposed antenna configuration, the ordinary square monopole can provide the fundamental and next higher resonant radiation band at 4.6 GHz and 8.3 GHz, respectively. As illustrated in Fig. 3, the H-shaped slot is playing an important role in the broadband characteristics and in determining the sensitivity of impedance matching of this type of antenna. This is because it can adjust the electromagnetic coupling effects between the patch and the ground plane, and improve its impedance bandwidth without any cost of size or expense [10, 11]. It is found that by inserting the H-shaped ring slot at the ground plane additional resonance (third resonance at 11.2 GHz) is excited and hence much wider impedance bandwidth with multi-resonance characteristics can be produced, especially at the higher band.

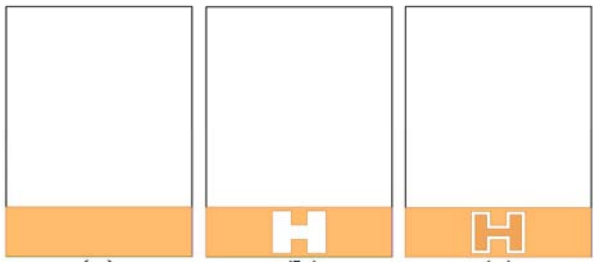

Fig. 2. (a) Ordinary square monopole antenna, (b) antenna with an H-shaped slot in the ground plane, and (c) antenna with an H-shaped ring slot in the ground plane.

To understand the phenomenon behind this new exited resonance performance, the simulated current distributions on the ground plane for the antennas studied in Fig. 2 (b) at 10 GHz and Fig. 2 (c) at 11.2 GHz are presented in Fig. 4 (a) and (b), respectively. It can be observed in Fig. 4 that the current concentrated on the edges of the interior and exterior of the slots. Therefore, the antenna impedance changes at this frequency due to the

resonant properties of these slots inserted in the ground plane [3].

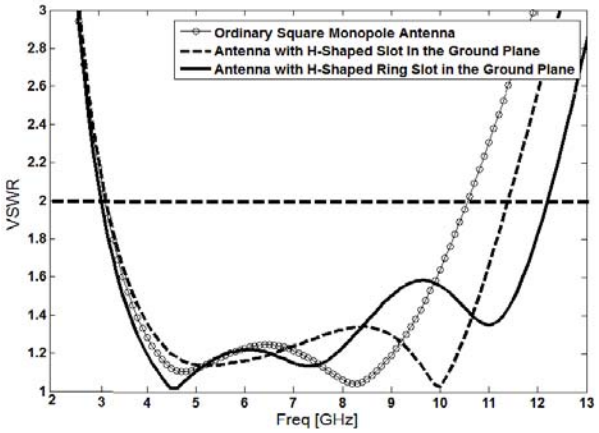

Fig. 3. Simulated VSWR characteristics for the various antenna structures shown in Fig. 2.

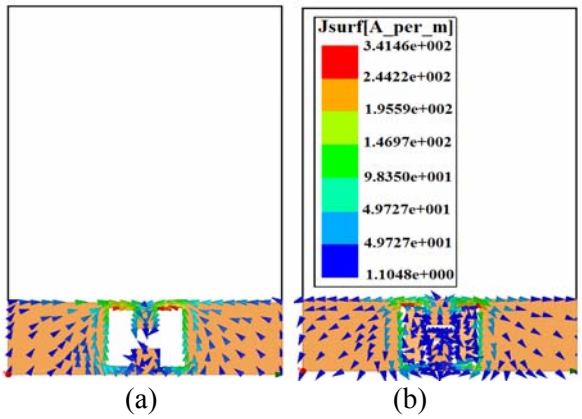

Fig. 4. Simulated surface current distributions in the ground plane for (a) the square monopole antenna with an H-shaped slot at 10 GHz and (b) the square monopole antenna with an H-shaped ring slot at 11.2 GHz.

Figure 5 shows the structure of various basic structures (square antenna with an H-shaped slot ring in the ground plane) used for band-notched function simulation studies. The VSWR characteristics for the basic structure (Fig. 5 (a)), with an H-shaped conductor backed plane (Fig. 5 (b)), and the proposed antenna ((Fig. 5(c)) are compared in Fig 6. As shown in Fig. 6, for the proposed antenna configuration, in order to generate single band-notch characteristics, we use an H-shaped conductor backed plane on the other side of the substrate. By inserting an H-ring conductor backed plane, a dual band-notched function is achieved that covers all the 5.2 GHz / 5.8 GHz WLAN, 3.5 GHz / 5.5 GHz WiMAX and 4 GHz C bands.

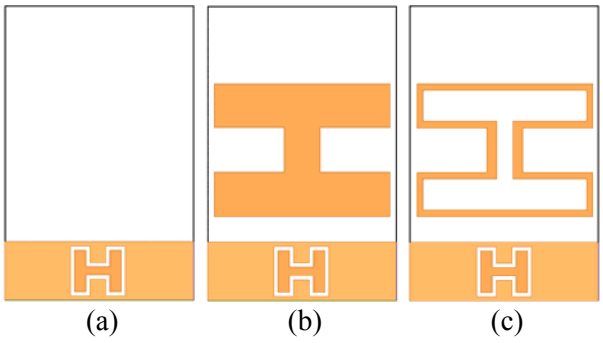

Fig. 5. (a) The basic structure (ordinary square monopole antenna with an H-ring slot in the ground plane), (b) basic structure with an H-shaped conductor backed plane, and (c) basic structure with an H-ring conductor backed plane**.**

To understand the phenomenon behind this dual band-notch performance, the simulated current distribution on the ground plane for the proposed antenna at the notch frequencies of 3.9 GHz and 5.5 GHz is presented in Fig. 7 (a) and (b), respectively. It can be observed from Fig. 7 (a) and (b) that the current is concentrated on the edges of the interior and exterior of the H-shaped ring conductor backed plane at frequencies 3.9 GHz and 5.5 GHz. Therefore, the antenna impedance changes at these frequencies due to the band-notch properties of the proposed structure.

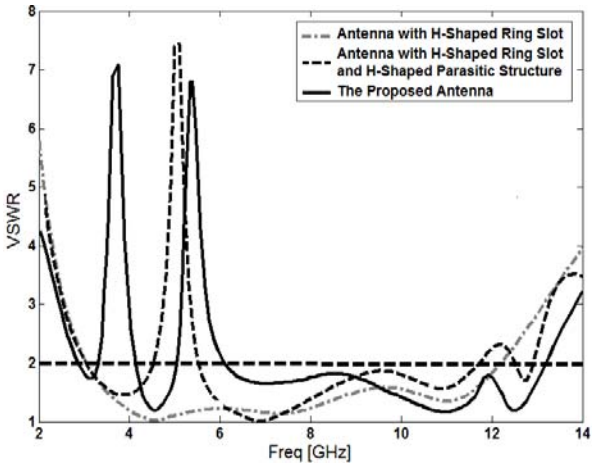

Fig. 6. Simulated VSWR characteristics for the various antenna structures shown in Fig. 5.

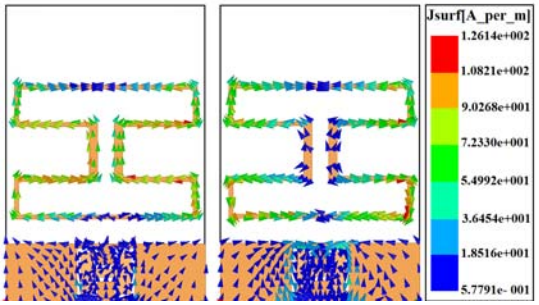

Fig. 7. Simulated surface current distributions on ground plane for the proposed antenna at (a) 3.9 GHz and (b) 5.5 GHz.

Figure 8 shows the conceptual equivalent circuit model for the proposed antenna, which has an RLC resonator and two shunt stubs. When the current path in the H-shaped ring conductor backed plane is equal to a half-wavelength at 3.9 GHz, as shown in Fig. 8 (c), the input impedance at the feeding point is zero (short circuit). Moreover, when the current path in the H-shaped ring conductor backed plane is equal to a half-wavelength at 5.5 GHz, as shown in Fig. 8(d), the input impedance at the feeding point is zero (short circuit).

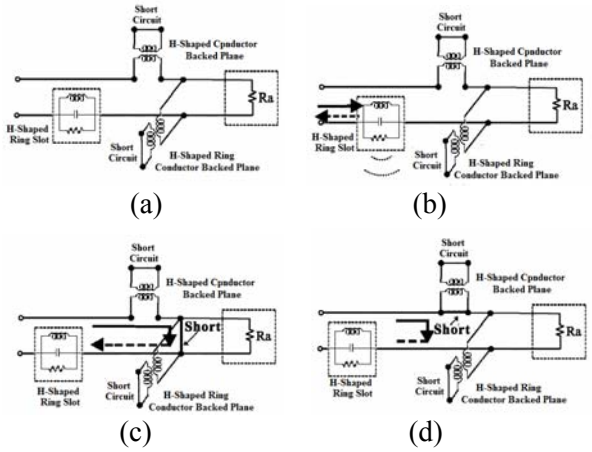

Fig. 8. (a) The conceptual equivalent-circuit model for the proposed antenna, (b) for the new resonance frequency, (c) for the first notched frequency, and (d) for the second notched frequency.

Figure 9 shows the measured and simulated VSWR characteristics of the proposed antenna. The fabricated antenna has the frequency band of 2.89 GHz to over than 13.43 GHz with two rejection bands around 3.45 GHz – 4.23 GHz and 5.07 GHz – 5.89 GHz. As shown in Fig. 9, there exists a discrepancy between the measured data and the simulated results. In a physical network analyzer measurement, the feeding mechanism of the proposed antenna is composed of an SMA connector and a microstrip line (the microstrip feed line is exited by an SMA connector), whereas the simulated results are obtained using the Ansoft simulation software (HFSS^{TM}), where the antenna is exited by a wave port that is renormalized to a 50-Ohm full port impedance. Therefore this discrepancy between the measured data and the simulated results could be due to the effect of the SMA port [6]. In order to verify the accuracy of the VSWR characteristics for the designed antenna, it is recommended that the manufacturing and measurement process need to be performed carefully. In conclusion, since the slot antenna is a short radiator, the SMA connector can modify its impedance matching.

Figure 10 shows the measured radiation patterns including both, the co-polarized and cross-polarized, *E*-plane (*x*-*z* plane) and *H*-plane (*y*-*z* plane), respectively. The main purpose of the radiation patterns is to demonstrate that the antenna actually radiates over a wide frequency band. It can be seen that the radiation patterns in *x*-*z* plane are nearly omnidirectional for the three frequencies.

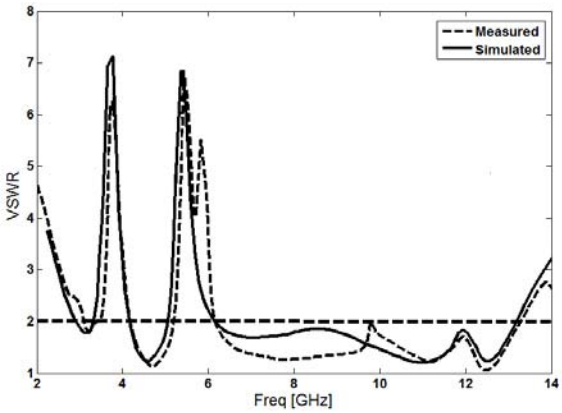

Fig. 9. Measured and simulated VSWR characteristic for the proposed antenna.

Figure 11 shows the effects of the ordinary H-shaped and H-shaped ring conductor backed plane, on the maximum gain in comparison to the same antenna without them. As shown in Fig. 11, the

basic structure (ordinary square monopole antenna with an H-shaped ring slot in the ground plane) has a gain that is low at 3 GHz and increases with frequency [12]. It is found that the gain of the basic structure is decreased with the use of the H-shaped conductor backed plane structures. It can be observed in Fig. 11 that by using the H-ring conductor backed plane, two sharp decrease of maximum gain in the notched frequencies band at 3.9 GHz and 5.5 GHz are shown. For other frequencies outside the notched frequencies' band, the antenna gain with the filter is similar to those without it.

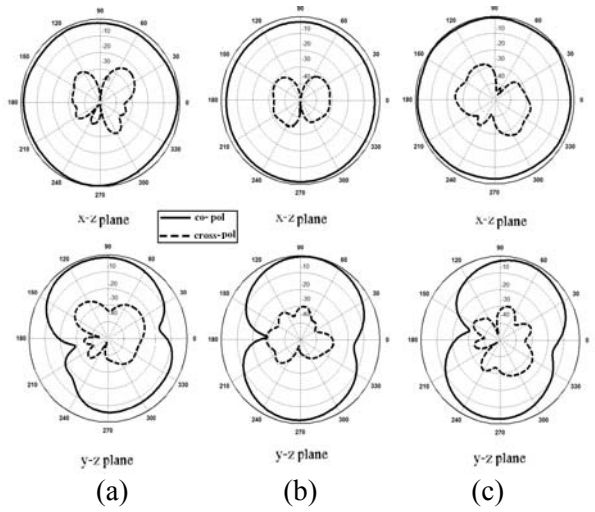

Fig. 10. Measured radiation patterns of the proposed antenna at frequency (a) 4.7 GHz, (b) 7.5 GHz, and (c) 9.8 GHz.

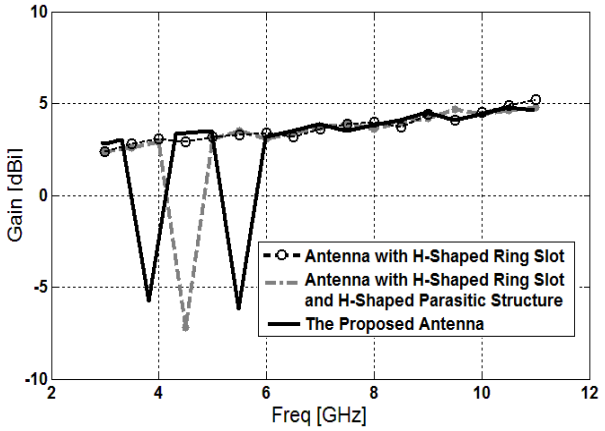

Fig. 11. Maximum gain comparisons for the basic structure (simulated), basic structure with H-shaped parasitic structure (simulated), and the proposed antenna (measured).

IV. CONCLUSIONS

In this paper, a novel compact wideband planar monopole antenna with single and dual band-notched characteristics has been proposed for various UWB applications. The fabricated antenna has the frequency band of 2.89 GHz to over than 13.43 GHz with two rejection bands around 3.45 GHz – 4.23 GHz and 5.07 GHz – 5.89 GHz. By cutting an H-ring slot in the ground plane, additional resonances are excited and hence much wider impedance bandwidth can be produced, especially at the higher band. Furthermore, by inserting an H-ring conductor backed plane on the other side of the substrate, dual band-notch characteristics are generated. The proposed antenna has a simple configuration and is easy to fabricate. Experimental results show that the proposed antenna could be a good candidate for UWB applications.

ACKNOWLEDGMENT

The authors are thankful to Microwave Technology (MWT) company staff for their beneficial and professional help (www.microwave-technology.com).

REFERENCES

[1] N. Ojaroudi, M. Ojaroudi, and S. Amiri, "Enhanced bandwidth of small square monopole antenna by using inverted U-shaped slot and conductor-backed plane," *Appl. Comp. Electro. Soc. (ACES) Journal*, vol. 27, no. 8, pp. 685-690, August 2012.

[2] J. Jung, W. Choi, and J. Choi, "A compact broadband antenna with an L-shaped notch," *IEICE Trans. Commun.*, vol. E89-B, no. 6, pp. 1968-1971, June 2006.

[3] N. Ojaroudi, M. Ojaroudi, and N. Ghadimi, "UWB omnidirectional square monopole antenna for use in circular cylindrical microwave imaging systems," *IEEE Antennas Wireless Propag. Lett.*, vol. 11, pp. 1350-1353, 2012.

[4] R. Azim, M. T. Islam, and N. Misran, "Design of a planar UWB antenna with new band enhancement technique," *Appl. Comp. Electro. Soc. (ACES) Journal*, vol. 26, no. 10, pp. 856-862, Oct. 2011.

[5] D. S. Javan and O. H. Ghouchani, "Cross slot antenna with U-shaped tuning stub for ultra wideband applications," *Appl. Comp. Electro. Soc. (ACES) Journal*, vol. 24, no. 4, pp. 427-432, Aug. 2009.

[6] M. Ojaroudi, "Printed monopole antenna with a novel band-notched folded trapezoid ultra-wideband," *J. of Electro. Waves and Appl.*, vol. 23, pp. 2513-2522, 2009.
[7] J. William and R. Nakkeeran, "A new UWB slot antenna with rejection of WiMax and WLAN bands," *Appl. Comp. Electro. Soc. (ACES) Journal*, vol. 25, no. 9, pp. 787-793, Sep. 2010.
[8] M. Naghshvarian-Jahromi and N. Komjani-Barchloui, "Analysis of the behavior of Sierpinski carpet monopole antenna," *Appl. Comp. Electro. Soc. (ACES) Journal*, vol. 24, no. 1, pp. 32-36, Feb. 2009.
[9] Ansoft High Frequency Structure Simulation (HFSS^{TM}), Ver. 13, *Ansoft Corporation*, 2010.
[10] M. C. Tang, S. Xiao, T. Deng, D. Wang, J. Guan, B. Wang, and G. D. Ge, "Compact UWB antenna with multiple band-notches for WiMAX and WLAN," *IEEE Trans. Antennas and Propag.*, vol. 59, no. 4, pp. 1372-1376, 2011.
[11] A. Ghazi, M. N. Azarmanesh, and M. Ojaroudi, "Muti-resonance square monopole antenna for ultra-wideband applications," *Progress In Electromagnetics Research (PIER C),* vol. 14, pp. 103-113, 2010.
[12] M. Ojaroudi, N. Ojaroudi, and Y. Ebazadeh, "Dual band-notch small square monopole antenna with enhanced bandwidth characteristics for UWB applications," *Appl. Comp. Electro. Soc. (ACES) Journal*, vol. 25, no.5, pp. 420-426, May 2012.

Mohammad Ojaroudi was born on 1984 in Germi, Iran. He received his B.Sc. degree in Electrical Engineering from Ardabil Branch, Islamic Azad University, and M.Sc. degree in Telecommunication Engineering from Urmia University. From 2010, he is working toward the Ph.D. degree at Shahid Beheshti University. From 2007 until now, he is a Teaching Assistant with the Department of Electrical Engineering, Ardabil Branch, Islamic Azad University, Ardabil, Iran. Since March 2008, he has been a Research Fellow (Chief Executive Officer) in the Microwave Technology Company (MWT), Tehran, Iran. His research interests include analysis and design of microstrip antennas, design and modeling of microwave structures, radar systems, and electromagnetic theory. He is author and coauthor of more than 100 journal and international conference papers.

Nasser Ojaroudi was born on 1986 in Germi, Iran. He received his B.Sc. degree in Electrical Engineering from Azad University, Ardabil Branch. From 2011, he is working toward the M.Sc. degree in Telecommunication Engineering at Shahid Rajaee Teacher Training University. Since March 2008, he has been a Research Fellow in the Microwave Technology Company (MWT), Tehran, Iran. His research interests include monopole antenna, slot antennas, microstrip antennas for radar systems, ultra-wideband (UWB) and small antennas for wireless communications, microwave passive devices and circuits, and microwave/millimeter systems.

Seyed Amin Mirhashemi was born on 1983 in Khalkhal, Iran. He received his B.Sc. degree in Electrical Engineering from Ardabil Branch, Islamic Azad University. From 2011, he is working toward the M.Sc. degree in Control Engineering at South Tehran Branch, Islamic Azad University, Tehran, Iran. Since March 2009, he has been a Research Fellow in the Microwave Technology Company (MWT), Tehran, Iran. His research interests include modeling of microstrip structures using neural networks and system identification methods.

A Compact Printed End-Fire Antenna for Radio Frequency Identification (RFID) Handheld Reader

Yuanhua Sun [1], Guangjun Wen [1], Ping Wang [1, 2], Yongjun Huang [1], and Zhibo Du [3]

[1] Centre for RFIC and System Technology, School of Communication and Information Engineering
University of Electronic Science and Technology of China, Chengdu, 611731, China
sunyuanhua17@gmail.com

[2] College of Electronic and Information Engineering
Chongqing Three Gorges University, Chongqing, 404000, China
wangpingcqz@163.com

[3] Chengdu University of Information Technology, Chengdu, 610225, China
du139123456789@163.com

Abstract ─ A new compact end-fire linear polarized printed antenna for a handheld radio frequency identification (RFID) reader is proposed for ultra high frequency (UHF) radio frequency identification (RFID) system in North America. The proposed planar end-fire antenna using two meandered dipole drivers, a folded reflector and a rectangular reflector are presented. The new antenna uses low-cost fabrication. The advantage of the end-fire antenna with meander dipole drivers compared to the conventional quasi-Yagi antenna is a reduction in the length of the driver, which allows closer space for RFID reader. the dimension of the antenna is 80×59 mm^2. The antenna has maximum gain of 3.6 dB and VSWR better than 2 around the US RFID bands (902-928MHz). We describe the antenna structure and present the comparison of simulation results with experimental data. The proposed antenna is fabricated, and measured reflection coefficient, radiation patterns and gain are presented.

Index Terms ─ RFID Reader, end-fire antenna, Radiation pattern, Gain.

I. INTRODUCTION

In recent years, radio frequency identification (RFID) technology has been rapidly developed and applied to many service industries, manufacturing companies, distribution logistics, goods flow systems and moving vehicle identification[1-3]. Many typical RFID tags have been studied[4-7]. For the applications involving item-level management[8][9], a RFID handheld reader plays an important role owing to its advantages of compactness, flexibility and maneuverability. By incorporating with a personal data assistant (PDA), a RFID handheld reader has the ability to provide a total solution for retail or library automation management. The growing demand for small compact wireless devices has increased the need for small antennas that can be integrated while providing acceptable overall performance[10][11]. Most of antennas do not have directional radiation. Some antennas have bidirectional radiation, but the its size is big for handheld reader [12]. In addition, usability of the reader unit in terms of reading directions and orientations of tags has to be taken into account. One of the features affecting the size, weight and ergonomist of handheld RFID reader is the reader antenna size and its positioning when affixed to the handheld reader unit. It is noted that, however, the antenna design in a RFID handheld reader should fulfill several unique requirements[13]. First of all, the reader antenna in a passive RFID system should demonstrate a somewhat lower reflection coefficient level than that in a usual communication system. It is because in such a

Submitted On: July 2, 2012
Accepted On: Nov. 11, 2012

system the backscattered signal from the tag is relatively weak, and prone to be interfered by the strong reflected signal from the reader antenna terminal. Second, in accordance with the emission regulation, the peak gain of a linear-polarized reader antenna must not exceed 6dBi in order to prevent the reader from violating the maximum allowed EIRP, i.e., 4W in North America. Moreover, regarding the public exposure to electromagnetic fields and the associated health issue, it would be beneficial if one could design a RFID handheld reader antenna with high front-to-back ratio so that the absorbed electromagnetic energy by the users can be substantially reduced. We proposed the antenna having good end-fire radiation pattern and can reduced the electromagnetic energy absorbed by users.

In this paper, we describe the design of compact end-fire antenna for the UHF band RFID handheld readers in North America. The antenna is composed of meandered printed dipoles, a folded reflector element and a rectangular reflector element. The proposed antenna has good directional radiation than others RFID antennas[11][12] and size of the proposed antenna is smaller than other handheld RFID antenna[10][12]. The antenna configuration and design methodology will be discussed in detail in Section II. The simulated and experimental results will be illustrated in Section III. This paper is concluded with a brief summary in Section IV.

II. ANTENNA CONFIGURATION

Similar to the quasi-Yagi antenna in[14]. Figure 1 shows the geometry of proposed antenna. The final antenna parameters are optimized using the commercial electromagnetic (EM) solver HFSS 13.0, and are given in the table I. The antenna is designed for UHF RFID applications in North America, i.e., in the frequency range of 902-928MHz. The length of the driven dipole and the reflector elements are optimized for simultaneously achieving excellent input impedance matching and the dipole arms are meandered to reduce the occupied dimension. Unlike a conventional quasi-Yagi antenna, here a reflector element is in close proximity to the driven element, and is also meandered in accordance with the outline of the dipole element. Accordingly, in addition to the surface wave excited in the substrate, in the proposed design the strong near-field coupling between the driven dipole and the reflector elements also helps improve the antenna impedance matching over a wide frequency range. Meander elements affects the resonant frequency of the antenna. The antenna elements are bent into meander shapes, suitable for fitting manufacturing form factors for a handheld RFID reader. The antenna has a high directional gain which results in the operating range around the US RFID bands (902-928MHz). Both top and bottom ground planes, which serve as reflectors in the design, keep the surface wave from propagating towards the backward direction. With such an arrangement, the backward-propagated surface wave can be substantially bounced back and further facilitates the end-fire radiation.

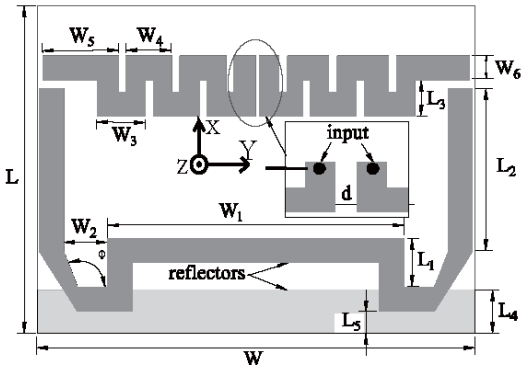

Fig. 1. The proposed antenna.

The finally chosen dimensions of the proposed antenna are illustrated in Table I.

Table I: The dimensions of the antenna (in mm)

L	W	W_1	W_2	W_3	W_4
51	80	54	8.1	9.3	9.3
W_5	L_1	L_2	L_3	L_4	φ
14.4	9	30.8	6.6	8	121°

The proposed anenna is designed based on basic Yagi-Uda antenna principle, consists of two radiating elements (driver and reflector). Both elements were shaped to fit into the available dimension while maintaining their resonant frequencies in the desired band. Key parameters in the design are lengths and shapes of antenna elements and their mutual spacing. The antenna was tuned to achieve 50 ohm (RFID Reader) impedance without using any external matching circuit that will occupy additional space.

For demonstration purpose in the laboratory, the proposed antenna was designed on a 1.6 mm

FR4 substrate with a dielectric constant $\varepsilon = 4.4$ and loss tangent $\tan\delta = 0.02$. The overall dimension of the antenna is 80×59 mm, or equivalently roughly $0.24\lambda_g \times 0.18\lambda_g$.

III.SIMULATION AND MEASUREMENT

To verify the proposed antenna design, a prototype is fabricated as shown in Fig. 2, and the results are presented here. All the measured results are carried out in anechoic chamber using a vector network analyzer (VNA) and other microwave test instruments.

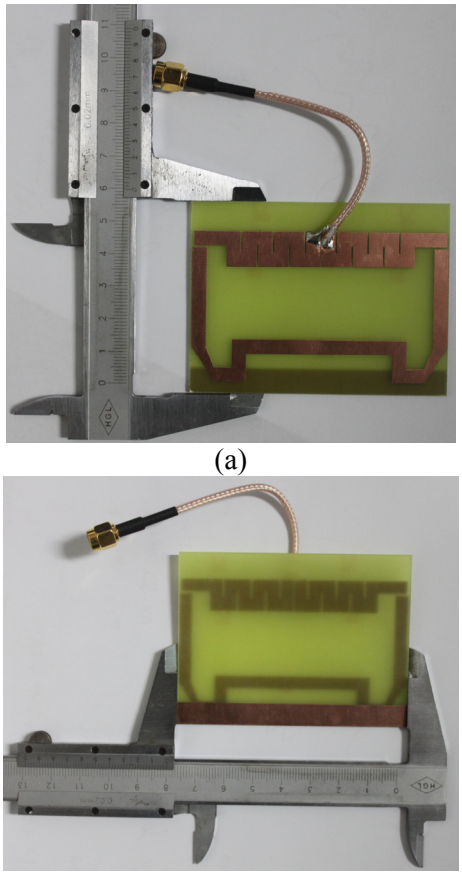

(a)

(b)

Fig. 2. Fabricated prototype of the proposed antenna. (a) top layer; (b) bottom layer.

All simulations were performed by Ansoft high-frequency structure simulation (HFSS) based on the finite-element method (FEM) [7][15]

The antenna simulated and measured magnitude of S_{11} are shown in Fig. 3. The simulation was performed by HFSS 13.0 and the measurement was taken by an Agilent performance network analyzer.

As shown in the Fig. 3, the agreement between the results in fairly good over the frequency band of interest. The simulated and measured center frequencies are given by 915 and 920 MHz, respectively. The slight frequency shift between the results can be mostly attributed to the fabrication tolerance. The measured XY-plane and XZ- plane radiation pattern and 3D radiation at 902, 915 and 928MHz are illustrated in Figs. 4, respectively. The radiation patterns are measured in a $7 \times 3 \times 3$ m^3 anechoic chamber and the measurement is performed by an Agilent network analyzer along with far-field measurement software. In the measurement the connecting cables along the Bakelite support ware carefully shielded by absorbers to reduce the multi-reflection interference. Meanwhile, the simulated -10 dB reflection coefficient bandwidths are from 890 to 940 MHz and the corresponding measurement data are given by 900-940MHz. and the current distribution at 915MHz are shown in Fig. 5. The experimental results demonstrate that the proposed design completely complies with the stringent requirement of impedance matching imposed on a handheld reader antenna, and the operating bandwidth with reflection coefficient better than -10dB covers the whole allocated spectrum for UHF RFID applications in North America.

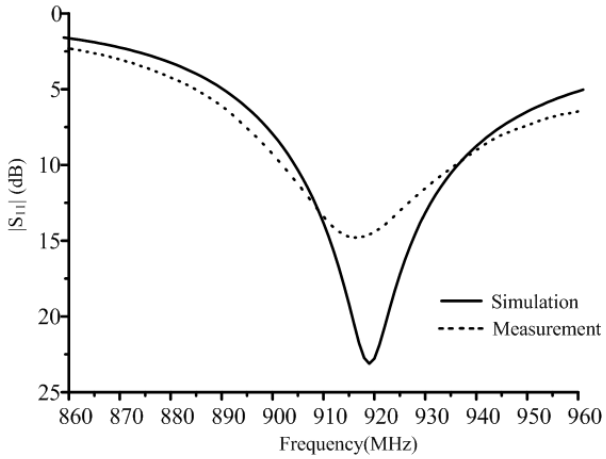

Fig. 3. Simulation and measured $|S_{11}|$.

For ease of practical applications, the studies of an important parameters of the driver meander dipoles and is also performed by simulations. One parameter is changed, while the other parameters are kept as in Table I. Figure 6 shows that the

center frequency is increasing while the length of the meander dipoles varies in a range when is changed from 4.5 to 4.9mm.

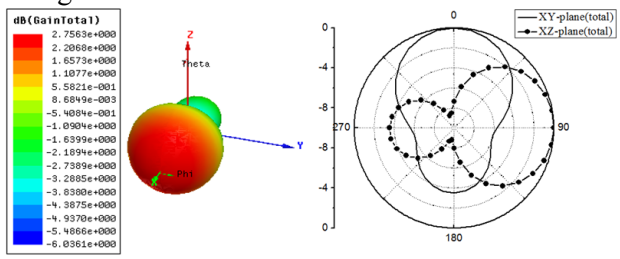

3D radiation Measured radiation

(a)

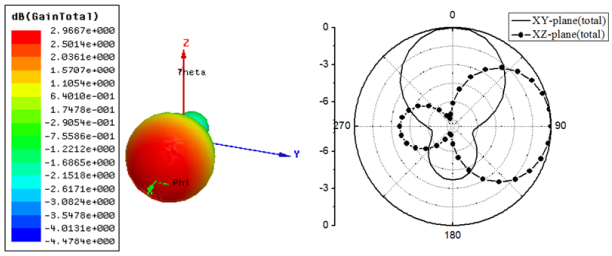

3D radiation Measured radiation

(b)

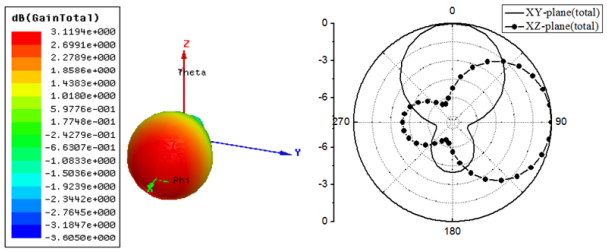

3D radiation Measured radiation

(c)

Fig. 4. 3D radiation and Measured radiation in the XY-plane and XZ-plane. (a) 902 MHz. (b) 915 MHz. (c) 928 MHz.

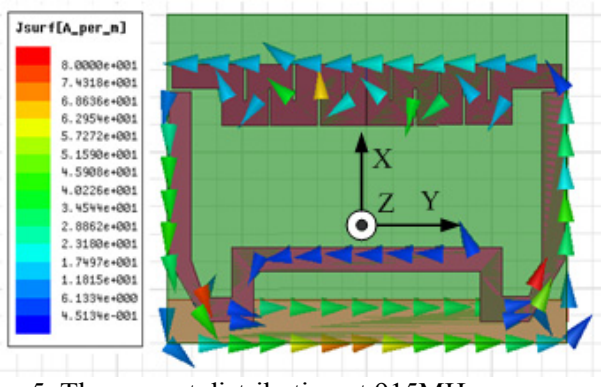

Fig. 5. The current distribution at 915MHz.

The Gain of the antenna was measured using the gain comparison method [16] , where the received power of the antenna under test is compared with known gain of a standard horn antenna. The simulated and measured gain and effectively are shown in Fig. 7, variation between the simulated and measured gain is within 0.5 dB , and this may be due to higher dielectric losses of the substrate, additional loss in the surface roughness of the microstrip patch.

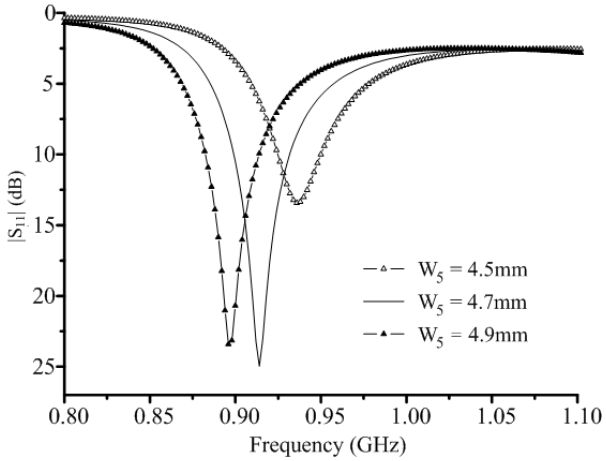

Fig. 6. Effects of varying driver mender length W_5.

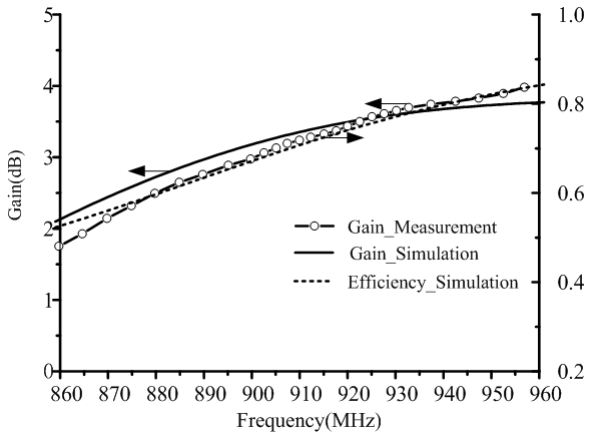

Fig. 7. Simulated gain and Measured gain in the +X direction, and Simulated efficiency of the antenna.

The Referring to the Fig. 3, measured results can be observed over the frequency band of interest. Clearly, Fig. 4 shows the radiation patterns similar to conventional Yagi radiation characteristics. The measured front-to-back ratio is at least 3 dB at 902 MHz and reaches 3.6 dB at

928MHz and remains better than 3 dB over the whole UHF RFID band from 902 to 928MHz. By adding directors elements can increase the front-to-back ratio, but these will increase the dimension of the antenna.

The measured bore sight gain is illustrated in Fig. 7. Referring to Fig. 7, the antenna gain rises steadily from 2.7dBi at 890MHz to 3.8dBi at 940MHz. The efficiency of the proposed antenna rises steadily from 62% to 80%.

IV. CONCLUSIONS

In this paper, we proposed a new printed end-fire antenna for UHF RFID handheld reader applications. The new end-fire antenna is suitable for fabrication on low-cost, low dielectric constant materials such as FR-4. The new antenna is based on the conventional printed quasi-Yagi antenna, where half-wavelength dipole driver element is replaced with two meander dipoles. The input impendence of the folded dipole quasi-Yagi antenna and its resonance frequency can be tuned by properly adjusting the parameters of the mender dipoles giving freedom for optimization. The advantages of the new antenna element are that it is more compact than the conventional design and is suitable for fabrication on low-cost, low dielectric constant materials. The antenna configuration, design, simulated and measured results have been well discussed. The experimental results reveal that the proposed antenna features a compact size of $0.24\lambda_g \times 0.18\lambda_g$, -10 dB reflection coefficient bandwidth of 50MHz and moderate gain around 2.7 to 3.8 dB. The antenna is well designed and may find applications in a variety of circumstances and the antenna is involved in item-level automation management with UHF RFID techniques.

ACKNOWLEDGMENT

This work is supported by Research Fund for the Doctoral Program of Higher Education of China (Grant No 20110185110014).

REFERENCES

[1] A. Toccafondi, C. D. Giovampaola, P. Braconi, A. Cucini, "UHF-HF RFID Integrated Transponder for Moving Vehicle Identification," *Applied Computational Electromagnetics Society (ACES) Journal*, vol. 25, no. 6, pp. 543-551, Jun. 2010.

[2] W. W. Y. Ng, Y.-S. Qiao, L. Lin, H.-L. Ding, P. P. K. Chan, and D. S. Yeung, "Intelligent Book Positioning for Library Using RFID and Book Spine Matching," in *Machine Learning and Cybernetics (ICMLC), International Conference on*, vol. 2, pp. 465-470, 2011.

[3] C. Feng, "Research for Application of RFID in Library," in *Computer and Communication Technologies in Agriculture Engineering (CCTAE), 2010 International Conference On*, vol. 1, pp. 262 -264, 2010.

[4] D. D. Arumugam, D. W. Engels, M. H. Mickle, "The Effect of Curvature on the Performance and Readability of Passive UHF RFID Tags," *Applied Computational Electromagnetics Society (ACES) Journal*, vol. 25, no. 3, pp. 206-217, Mar. 2010.

[5] H. Rajagopalan, Y. Rahmat-Samii, "Platform Tolerant and Conformal RFID Tag Antenna: Design, Construction and Measurements," *Applied Computational Electromagnetics Society (ACES) Journal*, vol. 25, no. 6, pp. 406-497, Jun. 2010.

[6] B. D. Braaten, R. P. Scheeler, M. Reich, R. M. Nelson, C. Bauer-Reich, J. Glower, G. J. Owen, "Compact Metamaterial-Based UHF RFID Antennas: Deformed Omega and Split-Ring Resonator Structures," *Applied Computational Electromagnetics Society (ACES) Journal*, vol. 25, no. 6, pp. 530-542, Jun. 2010.

[7] K. ElMahgoub, T. Elsherbeni, F. Yang, A. Z. Elsherbeni, L. Sydänheimo, L. Ukkonen, "Logo-Antenna Based RFID Tags for Advertising Application," *Applied Computational Electromagnetics Society (ACES) Journal*, vol. 25, no. 3, pp. 174-181, Mar. 2010.

[8] C. Goebel and O. Gu&#x0308 andnther, "The Information Value of Item-Level RFID in Retail Supply Chain Operations," in *System Sciences (HICSS), 2011 44th Hawaii International Conference on*, pp. 1-10, 2011.

[9] G. M. Gaukler, "Item-Level RFID in a Retail Supply Chain With Stock-Out-Based Substitution," *Industrial Informatics, IEEE Transactions on*, vol. 7, no. 2, pp. 362-370, May 2011.

[10] A. A. Babar, L. Ukkonen, A. Z. Elsherbeni, L. Sydanheimo, "A Small Dual Purpose UHF RFID Antenna Design," *Applied Computational Electromagnetics Society (ACES) Journal*, vol. 25, no. 12, pp. 1086-1096, Dec. 2010.

[11] A. Ferchichi, N. Sboui, A. Gharsallah, H. Baudrand, "New Antennas Based on Triangular Patch as a Solution for RFID Application," *Applied Computational Electromagnetics Society (ACES) Journal*, vol. 25, no. 3, pp. 199-205, Mar. 2010.

[12] Y. Lin, Y. Kao, S. Pan, H. Chen, "Bidirectional Radiated Circularly Polarized Annular-Ring Slot Antenna for Portable RFID Reader," *Applied Computational Electromagnetics Society (ACES) Journal*, vol. 25, no. 3, pp. 182-189, Mar. 2010.

[13] L. Ukkonen, L. Sydänheimo, and M. Kivikoski, "Read Range Performance Comparison of Compact Reader Antennas for a Handheld UHF RFID Reader [Supplement, Applications Practice]," *Communications Magazine, IEEE*, vol. 45, no. 4, pp. 24-31, Apr. 2007.

[14] K. M. K. H. Leong, Y. Qian, and T. Itoh, "Surface Wave Enhanced Broadband Planar Antenna for Wireless Applications," *Microwave and Wireless Components Letters, IEEE*, vol. 11, no. 2, pp. 62-64, Feb. 2001.

[15] HFSS: High Frequency Structure Simulator Based on the Finite Element Method. Ansoft.

[16] BALANIS C.A, *Antenna theory: analysis and design*. John Wiley & Sons, Inc., New York, 2nd ed., 1997.

Yuanhua Sun received the B.S. degree in communication engineering from the Liaocheng University in 2007, and M.S. degree in signal and information processing from Chengdu University of Information Technology in 2010. He is working toward the Ph.D degree in UESTC. His research interests include analytical and numerical modeling of metamaterials and antenna theory and design and signal processing.

Guangjun Wen was born in Sichuan, China, in 1964. He received his M. S. and Ph. D. degrees in Chongqing University of China in 1995 and UESTC in 1998, respectively. He is currently a professor and doctor supervisor in UESTC.

His research and industrial experience covers a broad spectrum of electromagnetics, including RF, Microwave, Millimeter wave Integrated Circuits and Systems design for Wireless Communication, Navigation, Identification, Mobile TV applications, RFIC/MMIC/MMMIC device modeling, System on Chip (SoC) and System in Package (SiC) Design, RF/Microwave/Millimeter wave Power source Design, "The Internet of things" devices and system, RFID system and networks, antennas, as well as model of electromagnetic metamaterial and its application in microwave engineering area.

Ping Wang received the B.S. degree in Physics from Western Chongqing University of China in 2005 and the M.S degree in Theoretical Physics from Chongqing University, Chongqing, in 2008. Currently, he is working toward the Ph.D. degree in UESTC. His current research interests include patch antennas, wideband antennas, and arrays.

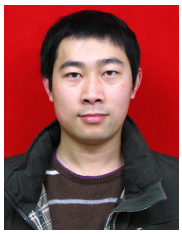

Yongjun Huang received the B.S. degree in Mathematics from Neijiang Normal University of China in 2007, M. S. degree in Communication Engineering from University of Electronic Science and Technology of China (UESTC) in 2010, and is currently working toward a Ph.D. degree in UESTC. His research activities are electromagnetic metamaterial and its application in microwave engineering area, FDTD and CAD analysis for the metamaterial model and characteristics.

Zhibo Du received the B.S. degree in computer science and technology from the Hebei University of Science and Technology in 2007, and M.S. degree in computer application from Chengdu University of Information Technology in 2010. He is working as assistant in Chengdu University of Information Technology. His research interests include application of antenna, and side channel attack on the security chip, for example electromagnetic attack, power attack and so on.

Railway Wheel Detector in the Presence of Eddy Current Brakes

A. Zamani and A. Mirabadi

School of Railway Engineering
Iran University of Science and Technology, Tehran, Iran
alizamani.e@gmail.com and mirabadi@iust.ac.ir

Abstract ─ In this paper, electromagnetic sensor is considered as a train wheel detector, which is one of the most important signalling systems to determine the clearance or occupancy of a track section. The wheel detector is affected by eddy current brakes and this problem has limited its use. In order to improve the wheel detection accuracy and eliminate the eddy current brake effect, the optimal design of sensors is carried out by means of finite element method. Kriging method is utilized to reduce the computational costs. Additionally, genetic algorithm is used as a multi-objective optimization method to find the optimum orientation.

Index Terms - Eddy current brakes, finite element method, genetic algorithm, Kriging, multi-objective optimization, and train wheel detector.

I. INTRODUCTION

Train detection equipment is considered as one of the most important and critical subsystems of the entire railway signaling system, with great importance for passenger and service safety. Axle counter is a particular type of train detection system, which is used widely on many railway lines, because of its beneficial features such as ease of installation, flexibility and low cost, over other train detection systems. Axle counters usually work on the basis of electromagnetic waves. Two coils installed on either side of a rail, acting respectively as transmitter and receiver, perform the role of wheel detector or axle counter sensors as shown in Fig. 1.

The axle counter system may be affected by eddy current brakes. Eddy Current Brake (ECB) is a developing brake system which makes use of Lenz's law to stop the train without mechanical contact. Due to the destroying effect of the ECB on the axle counter, in practice, trains with the eddy current brakes are not allowed to pass through the lines with the axle counter system. However, a wide range of studies aimed to solve such problems, which have been conducted by various researchers around the world. Different researchers, authorities, and companies have designed and developed new hardware and software [1, 2]. However, these designs cannot be implemented on old systems and also removing the old system and installing the new system is very expensive. So, a method for improving the old system is cheaper and more efficient. Experience shows that improving the orientation and position of the coils, is one of the cheapest and most effective methods in enhancing the performance of the system and improving the quality of the signal received in the receiving coil.

In order to find the optimum orientation of the coils, the authors of the present paper have studied the performance of the Response Surface Methodology (RSM) and also Kriging method in their recent publications [3, 4]. In the current paper, Kriging method and the Genetic Algorithm (GA) as a multi-objective optimization method are used to find the optimum orientation of the axle counter sensors and eliminate the ECB effect on it. Given the permanent and transient environmental noises and their effects on the sensors' performance and also the wide range of possible orientations, which can be considered, make it difficult to test all possible conditions with actual sensors. Modeling the system and simulating various local and environmental conditions provide an opportunity to analyse the system performance over a much wider range of orientations to find the optimum sensor coil orientation of the system.

Submitted On: Oct. 9, 2012
Accepted On: Jan. 3, 2013

In this research a finite element method (FEM) has been used to determine the induced voltage in the receiving coil. However, the FEM analysis of the whole continuous search space is time consuming and requires excessive processing effort. So the FEM analysis has been implemented for a limited number of orientations and then metamodeling techniques are utilized to estimate the performance of the system in other points of the spectrum. RSM, Kriging and MARS (Multivariate Adaptive Regression Splines) have been identified as the three most effective approaches in a range of applications, in that they provide the possibility of analysing the whole search space of the system. It is approved that Kriging method has the best performance through the other methods for the train wheel detector system [4]. Using the Kriging method provides two response surfaces, which should be optimized. Finally, a multi-objective optimizer such as genetic algorithm is needed to optimize the two response surfaces.

II. TRAIN WHEEL DETECTOR

Even in the early days of the railway in the 19th century, wheel detection had been an urgent desire for railway engineers, where they were concerned about signalling safety. In the past, mechanical, hydraulic, and finally pneumatic systems were used as a wheel detector. But, due to their limited application and deficient in high speeds, they were replaced in the 1950s by magnetic and contactless inductive devices. Today, the most common wheel detectors in Iran and many other countries are contactless inductive wheel detectors. They are easy to install, flexible, and low cost. Inductive wheel detectors make use of the electromagnetic flux linkage between two coils that are mounted on either side of the rail, to detect the passage of the wheels. Figure 1 shows a wheel detector.

Detailed analysis with the electromagnetic equations for the train wheel detector is performed in [4]. The FEM is used to determine the electromagnetic field around the sensor coils and also the induced voltage in the receiving coil. This provides the opportunity to model the system in a variety of coil orientations. Results of FEM modelling have been shown in Fig. 2. This figure illustrates the distribution of the flux lines in the presence and absence of the wheel. When there is no wheel between receiver and transmitter coils as shown in Fig. 2 (a), the magnetic flux flows along the receiving coil and induces a voltage in it. On the other hand, in the presence of the wheel as presented in Fig. 2 (b), less magnetic flux flows along the receiving coil and hence the lower induced voltage in the receiver.

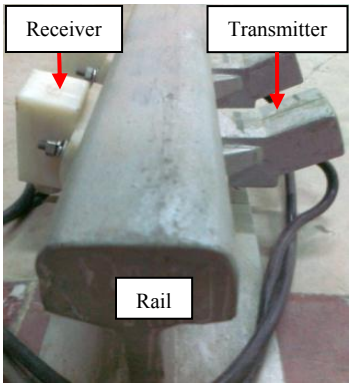

Fig. 1. Train wheel detector.

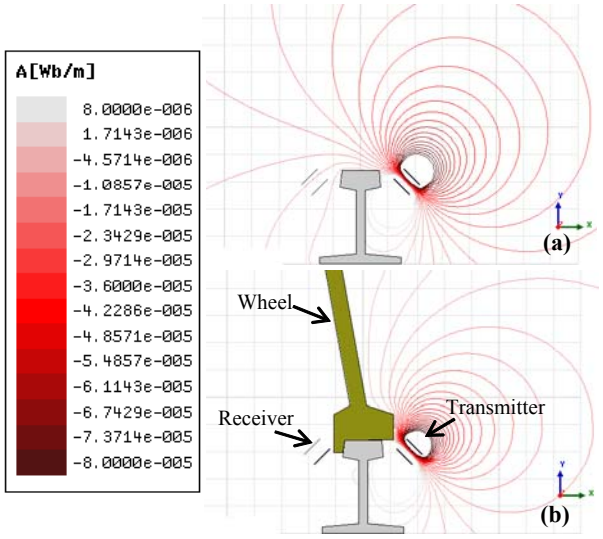

Fig. 2. Distribution of the flux lines with (a) no wheel and (b) wheel present.

In order to detect the passage of a wheel, the induced voltage in the receiving coil is monitored continuously. Furthermore, any changes exceeding predefined thresholds are interpreted as being caused by the presence or absence of a wheel. In other words, the wheel detector detects the wheel when the amplitude of the induced voltage in the receiving coil is less than a threshold level, as shown in Fig. 3.

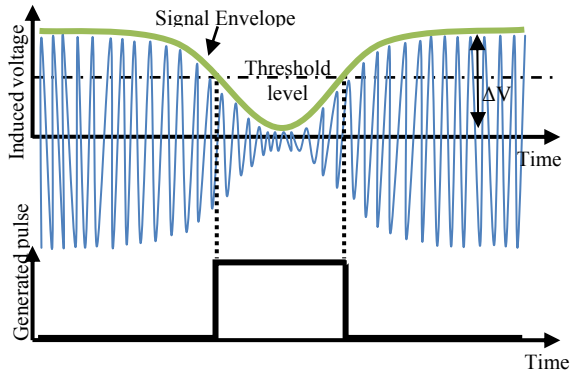

Fig. 3. Induced voltage and detecting principles.

Although axle counters are proven to be more reliable compared to other types of train detectors, it sometimes fails because of electromagnetic interferences and passage of trains with ECBs. The effect of electromagnetic noise on the output signal can be reduced or eliminated by generating a large difference in the voltage amplitudes, in the presence and absence of a wheel (ΔV). In the case which there is no ECB, the authors of the present paper have suggested (-45°, 45°) orientation for the wheel detectors [4]. In this paper, the authors are trying to find an appropriate orientation for the wheel detector coils to solve the problem of wheel detector in the presence of eddy current brake.

III. EDDY CURRENT BRAKE

The eddy current brake consists of a magnetic yoke with electrical coils positioned along the rail, which are being magnetized alternating as south and north magnetic poles as shown in Fig. 4. This magnet does not touch the rail, but is held at a definite small distance from the rail (approximately 7 mm). It does not move along the rail, it exerts only a vertical pull on the rail [5, 6].

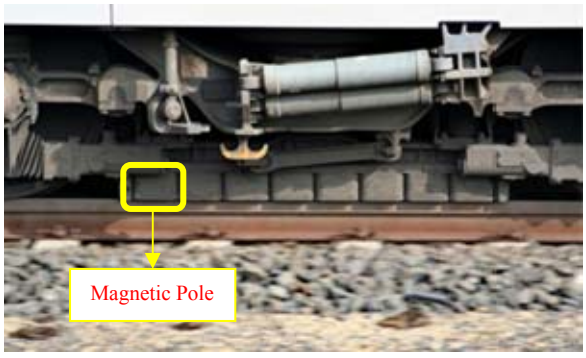

Fig. 4. Eddy current brake with 8 poles.

An ECB can affect the wheel detector in two possible ways: first, the ECB can affect the wheel detector as the wheel does. In other words, when the brakes are placed between the coils of the wheel detector, less magnetic flux arrives to the receiving coil and hence, lower voltage will be induced in the receiver and the ECB may be detected as a wheel. The second way is the transient current, which passes through the ECB. In this way, if the brake is near the wheel detector, it may induce a disturbing voltage in the coils of the wheel detector. However, the processor unit of an axle counter system detects only changes that have more than 5 second lengths; so, transient voltages cannot affect the whole axle counter system. Therefore, in this paper only the first effect of the ECB (physical presence) is analysed.

To analyse the effect of the ECB on the wheel detector, it is modelled by the FEM as shown in Fig. 5. This figure shows the FEM model of an ECB with six poles in the presence of the wheel detector.

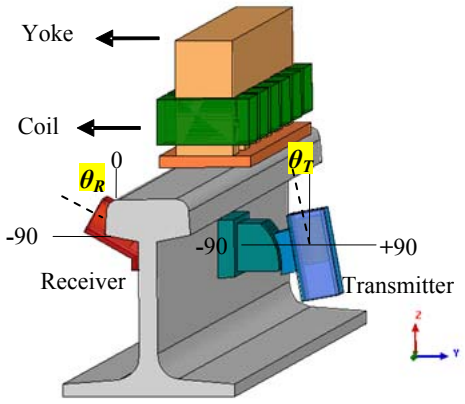

Fig. 5. FEM model of eddy current brake and wheel detector.

The distribution of the flux lines produced by the transmitter of the wheel detector, in the presence of the ECB is displayed in Fig. 6. In this figure the wheel detector coils are located in (θ_R, θ_T) = (45°, -45°), in which θ_R and θ_T are the receiver and transmitter angels, respectively. As can be seen from Fig. 6, the presence of the ECB between the coils causes reduction in the flux lines near the receiver. This reduction subsequently causes falling in the induced voltage in the receiver. This figure should be compared with Fig. 2, which displays the distribution of flux in the

presence and absence of the wheel. It can be comprehended that the effect of the ECB is very similar to that of the wheel.

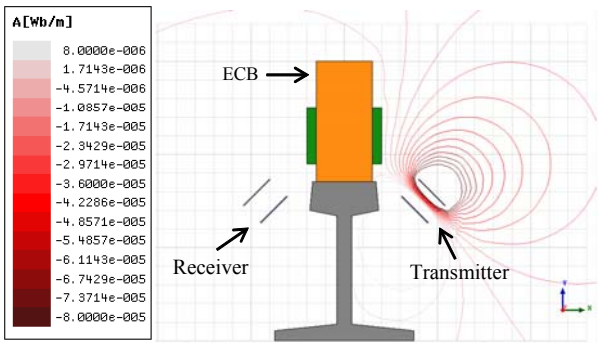

Fig. 6. Distribution of the flux lines in the presence of the eddy current brake.

The results of the FEM modeling show that the induced voltage in the presence of the ECB is about 230 mV, which is lower than the threshold level (470 mV), and consequently, the brake is recognized as a wheel. This status is indicated in Fig. 7.

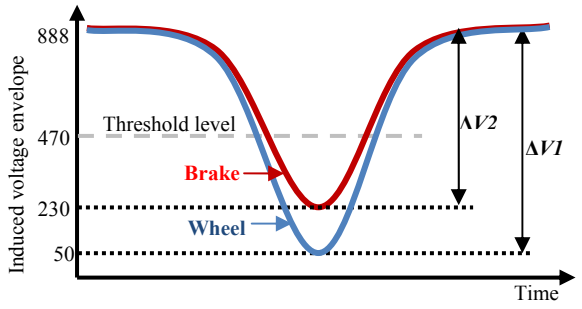

Fig. 7. Induced voltage envelopes by passing the wheel and the eddy current brake when coils are positioned in (θ_R, θ_T) = (-45°, 45°).

To solve this problem, the coils should be located in the optimized orientation in which the induced voltage envelope by passing the wheel is lower than the threshold level. Simultaneously, this voltage should be more than the threshold level by the passage of the brake. For this purpose the induced voltage for three situations: 1) without wheel and brake, 2) with wheel and with brake, and 3) in all orientations should be calculated. It can be easily comprehended that the voltage calculation for the all possible ranges of θ_R and θ_T (-90 to +90 degrees) is impossible. Therefore, a metamodeling technique like Kriging, which can almost accurately estimate the full-range voltages, is needed.

Using the Kriging method, two response surfaces (i.e., objectives) will be created. The first objective is for the voltage difference between the wheel absence and presence, which is indicated by ΔV_1 in Fig. 7, which should be maximized. The second objective is for the voltage difference between the brake absence and presence, which is illustrated by ΔV_2 in Fig. 7, and should be minimized. To find the optimum orientation in which both of the mentioned requirements are fulfilled, a multi-objective optimization method should be used. Both, Kriging method and multi-objective optimization method are explained in the following section.

IV. OPTIMIZATION

The aim of optimizing the wheel detector design, as an electromagnetic system, is to determine the most appropriate orientation of the coils, to achieve the following three goals:

1- Maximum sensitivity in detecting the train wheels,

2- maximum protection against the electro-magnetic noises,

3- avoid detecting the ECB as a wheel.

The first and second goals mean that ΔV_1 should be maximized, and the third goal means that ΔV_2 should be minimized. In other words, the aim of the optimization is to find the set of optimum θ_R and θ_T values, which provide the maximum ΔV_1 and at the same time the minimum ΔV_2. Thus, the system can be recognized as a "two inputs – two outputs" system, in which θ_R and θ_T are the inputs and ΔV_1 and ΔV_2 are the outputs. However, finding functions for ΔV_1 (θ_R, θ_T) and ΔV_2 (θ_R, θ_T) is not possible, but using statistical approximate models, such as Kriging model are recommended in some engineering cases [7, 8]. Although these approaches are not as accurate as direct optimization methods, they can be categorized as fast methods. A short explanation on the Kriging method is represented as follows.

A. Kriging method

Kriging, also called spatial modeling, is a regression method that is becoming more popular in optimization algorithms due to its advantages in

modeling nonlinear surfaces [9]. The Kriging model is defined as follows,

$$y(x) = f(x) + Z(x) \quad (1)$$

where $f(x)$ is the known approximation function, which is usually taken as a constant β and $Z(x)$ is the realization of a stochastic process with mean zero, variance σ^2, and covariance C.

The covariance matrix $C = [c_{ij}]$ can be defined as,

$$c_{ij} = \sigma^2 \mathbf{R}[R(x_i, x_j)], \qquad i, j = 1,2,...,n \quad (2)$$

where $\mathbf{R}$ is the correlation matrix and R is the user specified correlation functions. A popular choice for the correlation function is

$$R(x_i, x_j) = \prod_{k=1}^{m} \exp(-\alpha_k \mid x_i - x_j \mid^2), \quad (3)$$

where m is the number of design variables and α_k represents the unknown correlation function parameter vector. Small values of α_k smoothen the Kriging prediction, while for large values of α_k the Kriging model has accurate predictions around the sampled points over which it is built, and false predictions elsewhere.

Estimation of the response $y(x)$ at untried values of x is given by $\hat{y}(x)$

$$\hat{y} = \hat{\beta} + r^T(x)\mathbf{R}^{-1}(y - f\hat{\beta}), \quad (4)$$

where f is an $n \times 1$ vector of ones, when $f(x)$ is taken as constant, then $r^T(x)$ is the correlation between x and n sample points is expressed by,

$$r^T(x) = [R(x, x_1), R(x, x_2), ..., R(x, x_n)]^T \quad (5)$$

and $\hat{\beta}$ is an estimation of β, which is

$$\hat{\beta} = (f^T \mathbf{R}^{-1} f)^{-1} (f^T \mathbf{R}^{-1} y). \quad (6)$$

The above estimation is the minimum variance linear unbiased estimation, which is an optimal estimation in the statistical sense [10].

The estimated variance, $\hat{\sigma}^2$, is obtained from,

$$\hat{\sigma}^2 = \frac{1}{n}\left[(y - f\hat{\beta})^T \mathbf{R}^{-1} (y - f\hat{\beta})\right]. \quad (7)$$

The maximum likelihood estimator of α is then obtained by maximizing

$$\Phi(\alpha) = -\frac{1}{2}\left(n \ln(\hat{\sigma}^2) + \ln(|\mathbf{R}|)\right). \quad (8)$$

Both $\hat{\sigma}^2$ and $|\mathbf{R}|$ are functions of α and the solution of this nonlinear problem gives us the value of α and allows us to evaluate the function with the best linear unbiased estimation of β.

Using the explained method for ΔV_1 and ΔV_2 with 64 experimental points generated the two response surfaces are shown in Fig. 8.

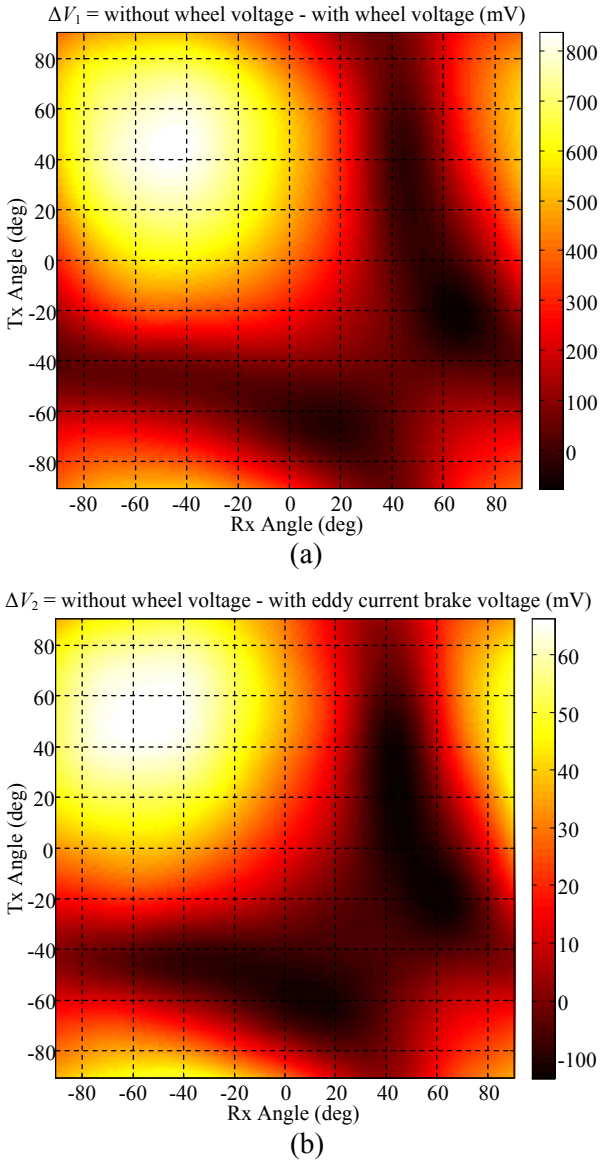

Fig. 8. (a) ΔV_1 and (b) ΔV_2 both, versus angles of receiver and transmitter coils.

B. Multi-objective optimization

Finding an optimum point for systems by more than one objective is not as easy as for one-objective systems, especially when improvement in one objective requires degradation in the other objectives. In this paper there are two variables (θ_R and θ_T), and two objectives (ΔV_1 and ΔV_2). So a system with two inputs and two outputs should be considered.

Assume a system with two variables (i.e., inputs) x_1 and x_2 in the parameter space Ω, and two objectives (i.e., outputs) F_1 and F_2 in the objective function space Λ,

$$\Omega = \left\{ x \in R^2 \right\} \tag{9}$$

$$\Lambda = \left\{ y \in R^2 : y = F(x), x \in \Omega \right\}. \tag{10}$$

The performance vector $F(x)$ maps the parameter space into the two dimension objective function space, shown in Fig. 9.

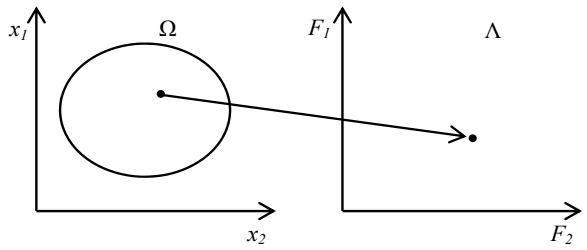

Fig. 9. Mapping from parameter space into objective function space.

The purpose is finding a non-inferior solution, which simultaneously minimizes F_1 and F_2 [11]. For this purpose, the objectives F_1 and F_2 must be traded off. A two dimensional representation is shown in Fig. 10, where the set of non-inferior solutions lie on the curve between A and B.

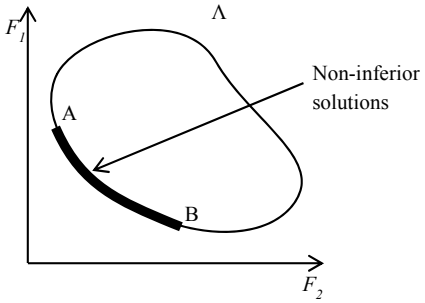

Fig. 10. Set of non-inferior solutions.

It can be clearly seen from Fig. 10 that an improvement in one objective, F_1, requires degradation in the other objective, F_2. So any points on the curve between A and B are non-inferior solution points. Since any point in Ω that is an inferior point that represents a point in which improvement can be attained in all the objectives, it is clear that such a point is of no value. Multi-objective optimization is, therefore, concerned with the generation and selection of non-inferior solution points [12].

There are several algorithms to find the non-inferior points in a multi-objective optimization problem. The most popular, easiest to implement, and most efficient one is the Non-dominated Sorting Genetic Algorithm II (NSGA-II) [13]. This algorithm sorts the current population according to the amount of solutions that dominate each other individual. A solution x_i is said to dominate the other solution y_i, if both of the following conditions are true,

1. $f_j(x_i) \leq f_j(y_i)$ for all functions j,
2. $f_j(x_i) < f_j(y_i)$ for at least one function j.

At any generation, an offspring population Q is first created from the parent population P with the usual crossover and mutation operators from GA. Thereafter, the number of solutions y_i that dominate the current solution x_i is counted. This is done for all individuals from both the parent population P and the offspring population Q. Some solutions will be found to be zero when other solutions dominate them. They are non-dominated, and thus are part of the Pareto front of the current populations. The solutions that have only one other solution dominate them, would have been part of the Pareto front if the members forming the true Pareto front would not have been present. Those who have two solutions dominating them would have formed the Pareto front if those solutions would have not been present, etc. Thus, the level of domination is indicative of the quality of that solution.

Next, the crowding distances are computed. These are the average distances between one solution and its surrounding solutions in the function-value space. Then, a new population R, which contains individuals from the previous two populations P and Q, sorted by their level of dominance, will be created. That is, first insert all Pareto members in R, and then insert those that have only one dominating solution, etc. Keep inserting individuals until R is the same size as P and Q. After that, a subset P_{i+1} from R by a binary tournament selection is created. This selection takes two random individuals from R, a_R and b_R, and lets them compete using their domination level and crowding distances as competitive factors. The “winning" individual is the one that satisfies the following: 1) rank (a) < rank (b) or 2) [rank (a) = rank (b) and the crowding distance (a)

> the crowding distance (b)]. Finally, a new offspring population Q_{i+1} is created, which is equal in size to the original P, Q, and R, using crossover and mutation from GA, using members from the subset P_{i+1} as parents. After the initialization step, the rest of the steps are then repeated.

In this paper the purpose is to find θ_R and θ_T values, which provide the maximum ΔV_1 (or the minimum "$-\Delta V_1$") and at the same time the minimum ΔV_2. NSGA-II runs with a population size of 50 and for 50 generations. The variables are used as real numbers and a recombination operator with crossover probability of p_c = 0.9, distribution index of η_c = 10, a polynomial mutation operator with mutation probability of p_m = 0.5, and finally, a distribution index of η_m = 15 are used. The result is shown in Fig. 11. The optimum response is calculated as (θ_R, θ_T) = (-7°, 5°), in which ΔV_1 and ΔV_2 are, respectively, 485 and 227 mV.

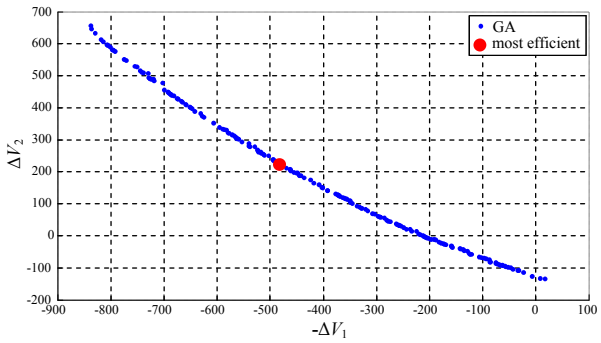

Fig. 11. Non-inferior solutions produced by GA.

V. RESULTS AND ANALYSIS

By locating the sensors in the optimum orientation, (θ_R, θ_T) = (-7°, 5°), the induced voltage envelopes by passing the wheel and the ECB will change as shown in Fig. 12. The new calculated orientation and the former are compared in Table 1. Difference between ΔV_1 and ΔV_2 is calculated to reveal the amount of success in the reduction of the brake effect on the wheel detector. In fact, a great ΔV_1 and a small ΔV_2 is the goal; so, the greater "$\Delta V_1 - \Delta V_2$" means the better solution.

It can be seen from this table that both of, ΔV_1 and ΔV_2 are reduced in the new orientation, but reduction in ΔV_2 is more considerable and thus "ΔV_1- ΔV_2" is improved. It means that in this orientation, the brake will not substantially affect the induced voltage and will not be detected as a wheel. Although in the new orientation ΔV_1 is lessened from 838 mV in (−45°, 45°) to 485 mV, the system sensitivity of the wheel is adequate. This is because the processing unit is able to sense voltages in the range of hundreds of millivolts and the output pulse will thus be generated by the passage of the wheel. In addition, the ECB will not be recognized as a wheel, because the induced voltage in the receiver is less than the threshold level. However, the threshold level should be adjusted again. As it is shown in Fig. 12, the threshold level is adjusted to the center of ΔV_1, which is 383 mV. Therefore, the processing unit will generate a pulse by the passage of a wheel, but the ECB will not affect the processing unit.

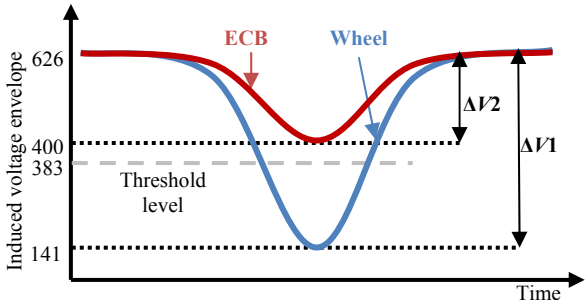

Fig. 12. Induced voltage envelopes by passing the wheel and the eddy current brake when coils are positioned in (θ_R, θ_T) = (-7°, 5°).

Table 1: Comparison of different orientations.

Orientation / Voltage (mV)	(-45°, 45°)	(-7°, 5°)
$\Delta V1$	838	485
$\Delta V2$	658	227
$\Delta V1 - \Delta V2$	180	258

VI. CONCLUSION

The aim of this paper was to eliminate the effect of eddy current brake on the train wheel detector without degradation of its performance against electromagnetic noises and its sensitivity to train wheels. Due to the fact that sensor orientation has a great effect on the amplitude of the induced voltage at the receiving coil, the authors focused on it. Kriging method was used for mathematical modeling of the induced voltage,

which changes over coils' angles. Then, genetic algorithm was used for finding the optimum orientation from two objectives that had been obtained by Kriging method.

The analysis results, showed that coil orientations of -7^{o}, $+5^{o}$, with the modeled constraints and conditions, present the optimum solution. However, these measurements are the results of simulation and may change in the real world. In this research the following assumptions were made: the effect of the rail vehicle body shell is neglected, and the train wheel and eddy current brake are considered to be stationary. More realistic conditions, like the influence of the vehicle body and also the wheel and eddy current brake motions, will be considered for future studies in this area.

REFERENCES

[1] T. Haecker and R. Klemm, "Development and testing of an axle counter which is insensitive to the impacts of high-speed traction vehicles Final report," *Stuttgart*, TV8822A2, 1993.

[2] J. Frauscher, "From track switch to inductive wheel sensor using a variety of technologies," *Signal + Draht*, vol. 1+2, no. 98, pp. 67-71, 2006.

[3] A. Zamani and A. Mirabadi, "Analysis of sensor orientation in railway axle counters using response surface methodology," *5th SASTech*, Mashhad, pp. 1-7, 2011.

[4] A. Zamani, A. Mirabadi, and F. Schmid, "Applying metamodeling techniques in the design and optimization of train wheel detector," *Sensor Review*, vol. 32, no. 4, pp. 327-336, 2012.

[5] I. Tsukerman, M. Mirzayee, M. Mirsalim, and H. Gholizad, "Motional eddy currents analysis in moving solid iron using magnetic equivalent circuits' method," *IEEE Proc. of Wireless Comm. and Appl. Comp. Electro. Soc. IEEE/ACES International Conference*, pp. 533-536, 2005.

[6] S. Kitanov and A. Podolskii, "Analysis of eddy-current and magnetic rail brakes for high-speed trains," *The Open Transportation Journal*, vol. 2, pp. 19-28, 2008.

[7] J. P. Kleijnen, "Kriging metamodeling in simulation: A review," *European Journal of Operation Research*, vol. 192, no. 3, pp. 707-716, 2009.

[8] S. Koziel and J. W. Bandler, "Accurate modeling of microwave devices using space mapping and Kriging," *Int. Review of Progress in Appl. Comp. Electro.*, Tampere, Finland, pp. 902-907, April 26-29, 2010.

[9] J. Kleijnen, "Design and analysis of computational experiments: overview," *Experimental Methods for the Analysis of Optimization Algorithms*, Thomas Bartz-Beielstein et al., Eds. Berlin: Springer, pp. 51-72, 2010.

[10] G. Lei, K. R. Shao, Y. Guo, J. Zhu, and J. D. Lavers, "Sequential optimization method for the design of electromagnetic device," *IEEE Trans. on Magnetic*, vol. 44, pp. 3217-3220, 2008.

[11] L. A. Zadeh, "Optimality and non-scalar-valued performance criteria," *IEEE Trans. on Automation Control*, vol. 8, no. 1, pp. 59-60, 1963.

[12] K. Deb, *Multi-Objective Optimization using Evolutionary Algorithms*. Chichester, England: John Wiley & Sons, Ltd, 2001.

[13] K. Deb, S. Agrawal, A. Pratap, and T. Meyarivan, "A fast and elitist multi-objective genetic algorithm: NSGA-II," *IEEE Trans. on Evol. Comp.*, vol. 6, pp. 182-197, 2002.

Ali Zamani received the B.Sc. Degree in Electrical Engineering from the University of Isfahan in 2008 and the M.Sc. Degree in Electric-Railway Engineering from Iran University of Science and Technology in 2011. During his M.Sc. Program, he worked on the design and optimization of railway axle counters. His research interests include applied electromagnetic and railway signaling.

Ahamd Mirabadi received his Ph.D. Degree in Control Engineering from the University of Sheffield in 2000 and the M.Sc. Degree in Mechatronics and optical Engineering from Loughborough University in 1994. He is an Associate Professor with the School of Railway Engineering, Iran University of Science and Technology. He is an author of numerous scientific papers in the field of railway control and signaling. His research interests include railway signaling and operation simulation, railway maintenance and condition monitoring, and safety critical systems.

2013 INSTITUTIONAL MEMBERS

DTIC-OCP LIBRARY
8725 John J. Kingman Rd, Ste 0944
Fort Belvoir, VA 22060-6218

AUSTRALIAN DEFENCE LIBRARY
Northcott Drive
Canberra, A.C.T. 2600 Australia

BEIJING BOOK CO, INC
701 E Linden Avenue
Linden, NJ 07036-2495

DARTMOUTH COLLEGE
6025 Baker/Berry Library
Hanover, NH 03755-3560

DSTO EDINBURGH
AU/33851-AP, PO Box 830470
Birmingham, AL 35283

SIMEON J. EARL – BAE SYSTEMS
W432A, Warton Aerodome
Preston, Lancs., UK PR4 1AX

ENGINEERING INFORMATION, INC
PO Box 543
Amsterdam, Netherlands 1000 Am

ETSE TELECOMUNICACION
Biblioteca, Campus Lagoas
Vigo, 36200 Spain

GA INSTITUTE OF TECHNOLOGY
EBS-Lib Mail code 0900
74 Cherry Street
Atlanta, GA 30332

TIMOTHY HOLZHEIMER
Raytheon
PO Box 1044
Rockwall, TX 75087

HRL LABS, RESEARCH LIBRARY
3011 Malibu Canyon
Malibu, CA 90265

IEE INSPEC
Michael Faraday House
6 Hills Way
Stevenage, Herts UK SG1 2AY

INSTITUTE FOR SCIENTIFIC INFO.
Publication Processing Dept.
3501 Market St.
Philadelphia, PA 19104-3302

LIBRARY – DRDC OTTAWA
3701 Carling Avenue
Ottawa, Ontario, Canada K1A OZ4

LIBRARY of CONGRESS
Reg. Of Copyrights
Attn: 407 Deposits
Washington DC, 20559

LINDA HALL LIBRARY
5109 Cherry Street
Kansas City, MO 64110-2498

MISSOURI S&T
400 W 14th Street
Rolla, MO 56409

MIT LINCOLN LABORATORY
Periodicals Library
244 Wood Street
Lexington, MA 02420

NATIONAL CHI NAN UNIVERSITY
Lily Journal & Book Co, Ltd
20920 Glenbrook Drive
Walnut, CA 91789-3809

JOHN NORGARD
UCCS
20340 Pine Shadow Drive
Colorado Springs, CO 80908

OSAMA MOHAMMED
Florida International University
10555 W Flagler Street
Miami, FL 33174

NAVAL POSTGRADUATE SCHOOL
Attn:J. Rozdal/411 Dyer Rd./ Rm 111
Monterey, CA 93943-5101

NDL KAGAKU
C/0 KWE-ACCESS
PO Box 300613 (JFK A/P)
Jamaica, NY 11430-0613

OVIEDO LIBRARY
PO BOX 830679
Birmingham, AL 35283

DAVID PAULSEN
E3Compliance
1523 North Joe Wilson Road
Cedr Hill, TX 75104-1437

PENN STATE UNIVERSITY
126 Paterno Library
University Park, PA 16802-1808

DAVID J. PINION
1122 E Pike Street #1217
SEATTLE, WA 98122

KATHERINE SIAKAVARA
Gymnasiou 8
Thessaloniki, Greece 55236

SWETS INFORMATION SERVICES
160 Ninth Avenue, Suite A
Runnemede, NJ 08078

YUTAKA TANGE
Maizuru Natl College of Technology
234 Shiroya
Maizuru, Kyoto, Japan 625-8511

TIB & UNIV. BIB. HANNOVER
DE/5100/G1/0001
Welfengarten 1B
Hannover, Germany 30167

UEKAE
PO Box 830470
Birmingham, AL 35283

UNIV OF CENTRAL FLORIDA
4000 Central Florida Boulevard
Orlando, FL 32816-8005

UNIVERSITY OF COLORADO
1720 Pleasant Street, 184 UCB
Boulder, CO 80309-0184

UNIVERSITY OF KANSAS – WATSON
1425 Jayhawk Blvd 210S
Lawrence, KS 66045-7594

UNIVERSITY OF MISSISSIPPI
JD Williams Library
University, MS 38677-1848

UNIVERSITY LIBRARY/HKUST
Clear Water Bay Road
Kowloon, Honk Kong

CHUAN CHENG WANG
8F, No. 31, Lane 546
MingCheng 2nd Road, Zuoying Dist
Kaoshiung City, Taiwan 813

THOMAS WEILAND
TU Darmstadt
Schlossgartenstrasse 8
Darmstadt, Hessen, Germany 64289

STEVEN WEISS
US Army Research Lab
2800 Powder Mill Road
Adelphi, MD 20783

YOSHIHIDE YAMADA
NATIONAL DEFENSE ACADEMY
1-10-20 Hashirimizu
Yokosuka, Kanagawa,
Japan 239-8686

APPLIED COMPUTATIONAL ELECTROMAGNETICS SOCIETY JOURNAL
http://aces.ee.olemiss.edu

INFORMATION FOR AUTHORS

PUBLICATION CRITERIA

Each paper is required to manifest some relation to applied computational electromagnetics. **Papers may address general issues in applied computational electromagnetics, or they may focus on specific applications, techniques, codes, or computational issues.** While the following list is not exhaustive, each paper will generally relate to at least one of these areas:

1. **Code validation.** This is done using internal checks or experimental, analytical or other computational data. Measured data of potential utility to code validation efforts will also be considered for publication.

2. **Code performance analysis.** This usually involves identification of numerical accuracy or other limitations, solution convergence, numerical and physical modeling error, and parameter tradeoffs. However, it is also permissible to address issues such as ease-of-use, set-up time, run time, special outputs, or other special features.

3. **Computational studies of basic physics.** This involves using a code, algorithm, or computational technique to simulate reality in such a way that better, or new physical insight or understanding, is achieved.

4. **New computational techniques** or new applications for existing computational techniques or codes.

5. **"Tricks of the trade"** in selecting and applying codes and techniques.

6. **New codes, algorithms, code enhancement, and code fixes.** This category is self-explanatory, but includes significant changes to existing codes, such as applicability extensions, algorithm optimization, problem correction, limitation removal, or other performance improvement. **Note: Code (or algorithm) capability descriptions are not acceptable, unless they contain sufficient technical material to justify consideration.**

7. **Code input/output issues.** This normally involves innovations in input (such as input geometry standardization, automatic mesh generation, or computer-aided design) or in output (whether it be tabular, graphical, statistical, Fourier-transformed, or otherwise signal-processed). Material dealing with input/output database management, output interpretation, or other input/output issues will also be considered for publication.

8. **Computer hardware issues.** This is the category for analysis of hardware capabilities and limitations of various types of electromagnetics computational requirements. Vector and parallel computational techniques and implementation are of particular interest.

Applications of interest include, but are not limited to, antennas (and their electromagnetic environments), networks, static fields, radar cross section, inverse scattering, shielding, radiation hazards, biological effects, biomedical applications, electromagnetic pulse (EMP), electromagnetic interference (EMI), electromagnetic compatibility (EMC), power transmission, charge transport, dielectric, magnetic and nonlinear materials, microwave components, MEMS, RFID, and MMIC technologies, remote sensing and geometrical and physical optics, radar and communications systems, sensors, fiber optics, plasmas, particle accelerators, generators and motors, electromagnetic wave propagation, non-destructive evaluation, eddy currents, and inverse scattering.

Techniques of interest include but not limited to frequency-domain and time-domain techniques, integral equation and differential equation techniques, diffraction theories, physical and geometrical optics, method of moments, finite differences and finite element techniques, transmission line method, modal expansions, perturbation methods, and hybrid methods.

Where possible and appropriate, authors are required to provide statements of quantitative accuracy for measured and/or computed data. This issue is discussed in "Accuracy & Publication: Requiring, quantitative accuracy statements to accompany data," by E. K. Miller, *ACES Newsletter*, Vol. 9, No. 3, pp. 23-29, 1994, ISBN 1056-9170.

SUBMITTAL PROCEDURE

All submissions should be uploaded to ACES server through ACES web site (http://aces.ee.olemiss.edu) by using the upload button, journal section. Only pdf files are accepted for submission. The file size should not be larger than 5MB, otherwise permission from the Editor-in-Chief should be obtained first. Automated acknowledgment of the electronic submission, after the upload process is successfully completed, will be sent to the corresponding author only. It is the responsibility of the corresponding author to keep the remaining authors, if applicable, informed. Email submission is not accepted and will not be processed.

EDITORIAL REVIEW

In order to ensure an appropriate level of quality control, papers are peer reviewed. They are reviewed both for technical correctness and for adherence to the listed guidelines regarding information content and format.

PAPER FORMAT

Only camera-ready electronic files are accepted for publication. The term **"camera-ready" means that the material is neat, legible, reproducible, and in accordance with the final version format listed below.**

The following requirements are in effect for the final version of an ACES Journal paper:

1. The paper title should not be placed on a separate page.

The title, author(s), abstract, and (space permitting) beginning of the paper itself should all be on the first page. The title, author(s), and author affiliations should be centered (center-justified) on the first page. The title should be of font size 16 and bolded, the author names should be of font size 12 and bolded, and the author affiliation should be of font size 12 (regular font, neither italic nor bolded).

2. An abstract is required. The abstract should be a brief summary of the work described in the paper. It should state the computer codes, computational techniques, and applications discussed in the paper (as applicable) and should otherwise be usable by technical abstracting and indexing services. The word "Abstract" has to be placed at the left margin of the paper, and should be bolded and italic. It also should be followed by a hyphen (—) with the main text of the abstract starting on the same line.

3. All section titles have to be centered and all the title letters should be written in caps. The section titles need to be numbered using roman numbering (I. II. ….)

4. Either British English or American English spellings may be used, provided that each word is spelled consistently throughout the paper.

5. Internal consistency of references format should be maintained. As a guideline for authors, we recommend that references be given using numerical numbering in the body of the paper (with numerical listing of all references at the end of the paper). The first letter of the authors' first name should be listed followed by a period, which in turn, followed by the authors' complete last name. Use a coma (,) to separate between the authors' names. Titles of papers or articles should be in quotation marks (" "), followed by the title of journal, which should be in italic font. The journal volume (vol.), issue number (no.), page numbering (pp.), month and year of publication should come after the journal title in the sequence listed here.

6. Internal consistency shall also be maintained for other elements of style, such as equation numbering. Equation numbers should be placed in parentheses at the right column margin. All symbols in any equation have to be defined before the equation appears or right immediately following the equation.

7. The use of SI units is strongly encouraged. English units may be used as secondary units (in parentheses).

8. Figures and tables should be formatted appropriately (centered within the column, side-by-side, etc.) on the page such that the presented data appears close to and after it is being referenced in the text. When including figures and tables, all care should be taken so that they will appear appropriately when printed in black and white. For better visibility of paper on computer screen, it is good to make color figures with different line styles for figures with multiple curves. Colors should also be tested to insure their ability to be distinguished after black and white printing. Avoid the use of large symbols with curves in a figure. It is always better to use different line styles such as solid, dotted, dashed, etc.

9. A figure caption should be located directly beneath the corresponding figure, and should be fully justified.

10. The intent and meaning of all text must be clear. For authors who are not masters of the English language, the ACES Editorial Staff will provide assistance with grammar (subject to clarity of intent and meaning). However, this may delay the scheduled publication date.

11. Unused space should be minimized. Sections and subsections should not normally begin on a new page.

ACES reserves the right to edit any uploaded material, however, this is not generally done. It is the author(s) responsibility to provide acceptable camera-ready files in pdf and MSWord formats. Incompatible or incomplete files will not be processed for publication, and authors will be requested to re-upload a revised acceptable version.

COPYRIGHTS AND RELEASES

Each primary author must execute the online copyright form and obtain a release from his/her organization vesting the copyright with ACES. Both the author(s) and affiliated organization(s) are allowed to use the copyrighted material freely for their own private purposes.

Permission is granted to quote short passages and reproduce figures and tables from and ACES Journal issue provided the source is cited. Copies of ACES Journal articles may be made in accordance with usage permitted by Sections 107 or 108 of the U.S. Copyright Law. This consent does not extend to other kinds of copying, such as for general distribution, for advertising or promotional purposes, for creating new collective works, or for resale. The reproduction of multiple copies and the use of articles or extracts for commercial purposes require the consent of the author and specific permission from ACES. Institutional members are allowed to copy any ACES Journal issue for their internal distribution only.

PUBLICATION CHARGES

All authors are allowed for 8 printed pages per paper without charge. Mandatory page charges of $75 a page apply to all pages in excess of 8 printed pages. Authors are entitled to one, free of charge, copy of the printed journal issue in which their paper was published. Additional reprints are available for $ 50. Requests for additional re-prints should be submitted to the managing editor or ACES Secretary.

Corresponding author is required to complete the online form for the over page charge payment right after the initial acceptance of the paper is conveyed to the corresponding author by email.

ACES Journal is abstracted in INSPEC, in Engineering Index, DTIC, Science Citation Index Expanded, the Research Alert, and to Current Contents/Engineering, Computing & Technology.